March 2016

Integrated Solar Technologies with Outdoor Pedestrian Bridge Superstructure Decking

Richard K. Racz Mr.
University of Massachusetts Amherst

Richard Racz

Recommended Citation

Racz, Richard K. Mr. and Racz, Richard, "Integrated Solar Technologies with Outdoor Pedestrian Bridge Superstructure Decking" (2016). *Masters Theses*. 332.
https://scholarworks.umass.edu/masters_theses_2/332

Integrated Solar Technologies with Outdoor Pedestrian Bridge Superstructure Decking

A Thesis Presented

by

Richard Kevin Racz

Submitted to the Graduate School of the University of Massachusetts, Amherst in partial
fulfillment of the requirements for the degree of

MASTER OS SCIENCE IN CIVIL ENGINEERING

February 2016

Civil and Environmental Engineering

Integrated Solar Technologies with Outdoor Pedestrian Bridge Superstructure Decking

A Thesis Presented

By

RICHARD KEVIN RACZ

Approved as to style and content by:

Sanjay Arwade, Chair

Sergio Brena, Member

Michael Knodler Jr., Member

Richard N. Palmer, Department Head

Civil and Environmental Engineering Department

DEDICATION

I’d like to thank my great friends and class mates, as well as my family. Without all of your support and confidence in me this project would never have be possible. Thank you to all.

ACKNOWLEDGEMENTS

I would like to thank the professionals who provided their assistance in this project. Their efforts made much of the design and concepts possible, and the project could not have been completed without their help. Thank you to the University of Massachusetts, Amherst for providing me the financial means to complete this project and support my efforts along the way. I greatly appreciate the guidance and support that the following individuals provided:

- Dr. Sanjay Raja Arwade, Ph.D. - The University of Massachusetts, Amherst, Civil Engineering Department
- Dr. Behrouz Shafei, Ph.D., P.E. – Iowa State University, Civil Engineering Department
- Dr. Michael Knodler Jr. – Ph.D. – The University of Massachusetts, Amherst, Civil Engineering Department
- Dr. Sergio F. Brena, Ph.D. – The University of Massachusetts, Amherst, Civil Engineering Department

ABSTRACT

INTEGRATED SOLAR TECHNOLOGIES WITH OUTDOOR PEDESTRIAN BRIDGE SUPERSTRUCTURE DECKING

FEBRUARY 2016

RICHARD KEVIN RACZ, B.S., UNIVERSITY OF MASSACHUSETTS AMHERST

M.S.C.E., UNIVERSITY OF MASSACHUSETTS AMHERST

Directed by: Sanjay R. Arwade

Solar technology has been a major topic in sustainable design for many years. In the last five years, however, the solar technology industry has seen a rapid growth in installations and technological advances in cell design. Combined with a rapidly declining overall system cost, the idea of introducing solar technology into a wider range of applications is becoming a focus for engineers and scientists around the world. So many variables which alter solar energy production, such as the sun and surrounding environment, determine whether a solar design is beneficial. This thesis presents a bridge deck surface integrated with solar cells tested under all AASHTO LRFD pedestrian bridge loadings. A detailed solar analysis of the University of Massachusetts's campus is presented to determine if solar integration is even plausible for the Northeastern United States with the energy limitations created by the deck integration, as well as an economic evaluation of the deck design. The purpose of this thesis was to determine if a walking surface could be integrated with solar technology and be a plausible alternative to conventional walking surfaces, while providing a source of sustainable power.

TABLE OF CONTENTS

Page

CHAPTER

LIST OF TABLES

Page

LIST OF FIGURES

Page

LIST OF SYMBOLS

α = Sun elevation angle

θ = Zenith angle

I = Solar irradiance

I_g = Global solar irradiance on the earth’s surface

I_0 = Solar irradiance where zenith is equal to zero perpendicular to incident irradiance

I_θ = Solar irradiance where zenith is greater than zero

AM = Air Mass

δ = Declination angle

φ = latitude of given location on earth

β = module tilt angle measured from the horizontal

PV = Photovoltaic

POA = Plane of Array (measurements perpendicular to solar panel)

P-N junction = Positive-Negative junction (the charged layers of a PV monocrystalline cell)

GHI = Global Horizontal Irradiance

COF = Coefficient of Friction

CHAPTER 1

INTRODUCTION

Solar energy costs are drawing closer to traditional power costs in many markets. With high demand from both residential and commercial consumers, new and innovative solar applications have become a major topic in research facilities across the globe. With the cost per solar generated kilowatt-hour falling lower every year and cost of conventional power increasing, the time to expand beyond traditional solar applications is now. Any proposed design must be efficient and reliable in power generation while ultimately providing clear financial benefits over its lifetime. The greatest cost analyses of solar projects take into account many variables, but ultimately reduce to a simple figure of cost per kilowatt-hour in comparison with conventional power systems. In the past year alone the average cost of electricity in Massachusetts increased by 23.5% reaching 20.8 cents per kilowatt-hour as expressed in Figure 1-1.

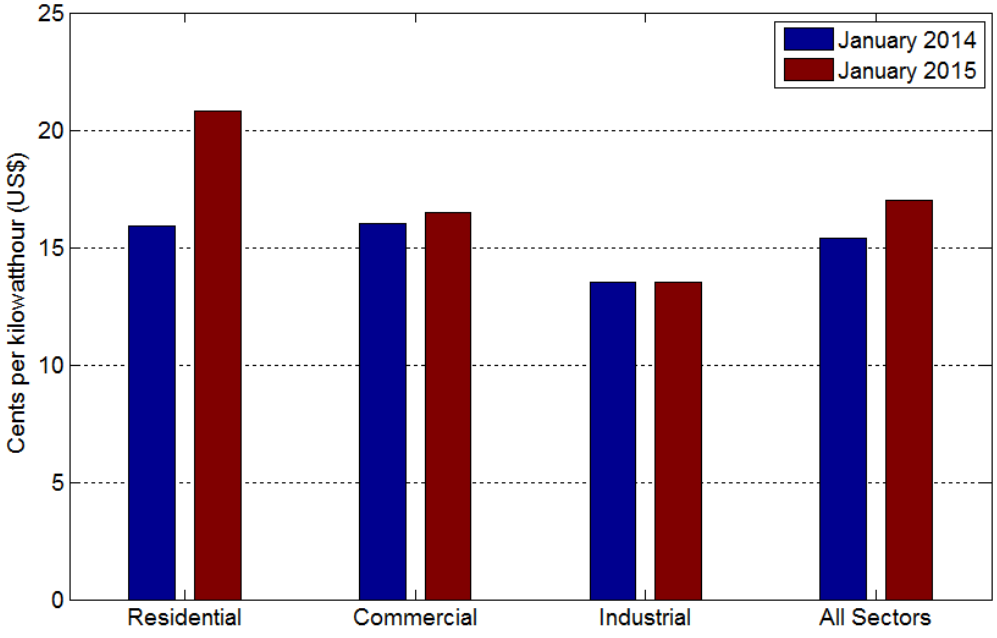

Figure 1-1: Retail Price of Electricity, Massachusetts (Energy Information Administration 2015)

The objective of this thesis is to engineer a suitable pedestrian bridge deck surface that is both safe and able to generate a beneficial amount of power from incident irradiance. The

University of Massachusetts has recently adopted a new campus master plan that looks fifty years into the future. The plan matches academic vision with facilities to strengthen a sense of community and enhance the campus's beauty. The plan calls for a pedestrian bridge to be erected across the campus pond located in the heart of the campus. This thesis will explore the challenges incorporated in the integration of a solar walking surface with the proposed campus pedestrian bridge as a case study. The pedestrian bridge deck will be designed for specified limit states to achieve the objective of durability, and serviceability with regard to issues of economic feasibility, and aesthetics.

The geometry of the bridge decking will be fitted with an array of solar modules which will be exposed to typical pedestrian bridge loadings. The mechanics of the decking will be analyzed to determine if a feasible deck surface, under AASHTO and MassDOT loadings, can be created where the underlying solar cells remain undamaged.

1.1 Netherlands Solar Innovation:

Wouldn't it be nice if our roads act like solar panels? And if we could drive our vehicles with the solar power generated by this? In 2009 these simple, yet innovative questions kick started the beginning of the solar based bike path prototype called SolaRoad. The Province of Noord-Holland, road construction company Ooms Civiel and technical service provider Imtech accepted the invitation and now form, together with TNO, the core consortium that is developing SolaRoad (SolaRoad 2009). Figures 1-2 and 1-3 show the completed prototype and pilot.

Figure 1-2: SolaRoad Pilot (SolaRoad 2014)

Dutch imagination and innovation has helped push the boundaries of solar capabilities for future research. This thesis looks to explore and expand upon the abilities of its own solar integrated walking surface, in hopes to engineer an improved design.

Figure 1-3: SolaRoad Pilot 2 (SolaRoad 2014)

1.2 Site Location:

The proposed site for the pedestrian bridge is located at the University of Massachusetts' campus pond in Amherst, Massachusetts with approximate latitude and longitude coordinates of 42° 23' 22.7" N, 72° 31' 35.3" W.

Figure 1-4: Proposed Site Location (Google Maps 2015)

The pedestrian bridge is to cross the University campus pond and connect the west and east shores of the pond as seen in Figure 1-4. The bridge will begin at roughly mid-span of the pond, following the 50 year campus master plan. The bridge location follows the idea of an original campus layout which the University incorporated into their campus plan. "Ellis Way" is a pedestrian walking path which forms an arc starting from the pedestrian crosswalk at Knowlton dormitory, and proceeds to arc around the Lincoln Campus Center, crossing the campus pond as seen in Figure 1-5, finishing with an intersection at East Pleasant Street by the southwest façade of Morrill Science Center. Ellis way arc's main purpose is to connect the University's East and West campuses as it was intended to do back when originally designed. The arc in Figure 1-5 will be one of the most populated walkways on campus. With the implementation of a bridge the conflicting campus pond will no longer "split" the campus into two, but rather open and interconnect it creating a closer and thriving campus community. The Bridge will span roughly 250ft across the pond, with a 15ft clear width.

Figure 1-5: Master Plan "Ellis Way" Pedestrian Arc (UMass Amherst Campus Planning Division 2012)

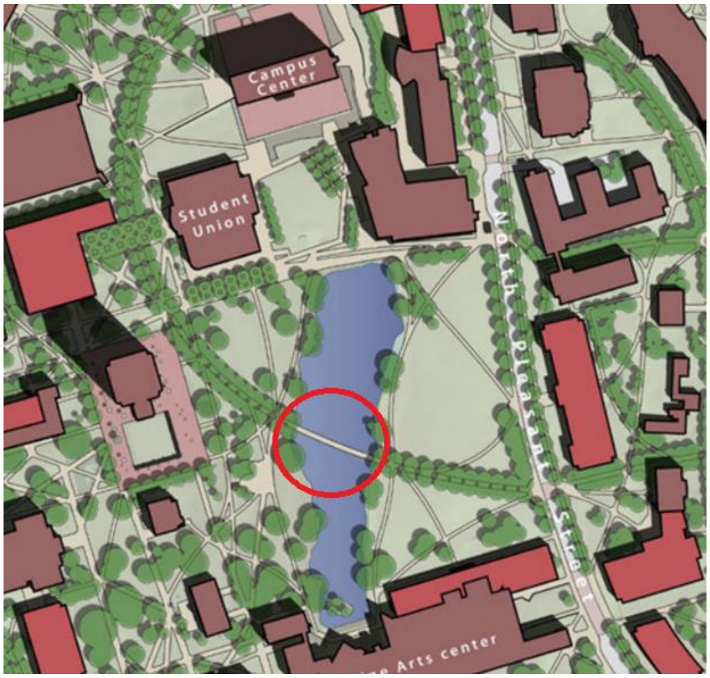

Figure 1-6: Master Plan Bridge Location (UMass Amherst Campus Planning Division 2012)

Figures 1-7 and 1-8were taken from all three pond shores of the proposed project site on 7/12/15 at the University of Massachusetts, Amherst and show current site conditions for the proposed bridge location.

Figure 1-7: North Pond Shore Looking South (left) West Pond Shore Looking East (right) (Racz 2015)

Figure 1-8: View from East Pond Shore Looking West (Racz 2015)

CHAPTER 2

ASSESSING THE PARAMETERS OF NORTH-EAST SOLAR POTENTIAL

Solar Radiation is an unlimited source of power for earth's inhabitants; it is clean and is readily accessible to every person on earth. Like alternative sources of power, solar energy has its challenges of being harnessed and converted to power. However, it is unlike any other energy source. It does not need to be drilled for beneath the earth's surface, nor does it need a complex chemical breakdown of its molecular structure to become efficient. In order to receive the most from the sun's radiation, one must look to the sky and understand the challenges solar radiation faces every second of every day to reach the earth's surface. The sun's radiation travels a great distance, and along the way encounters obstacles that distort its intensity.

The more this process is understood the more accurate solar power estimates will be for the University's solar bridge decking. With accurate energy predictions, negative influences which question the feasibility of a project such as this can be proven false or in many cases drastically over exaggerated. The more in depth and understood solar data is explained, the better chance solar concepts have at becoming realities. Investigating the steps needed to improve the impact of PV technologies in Massachusetts can help make an accurate prediction of the deck's power generating capabilities. In this chapter solar radiation's path from the sun to the proposed bridge decking will be explained, along with all factors which influence a solar modules ability to produce power. The systems reliability will be evaluated and a cost analysis will be conducted.

2.1 Solar Radiation Spectrum:

Solar radiation is the radiant energy which is emitted by the sun and travels through extraterrestrial space in all directions outward from the star of origin. The sun's radiation travels to earth in the form of electromagnetic waves on a wide spectrum of wavelengths. About one half of the radiation received by the earth is in the visible short-wave part of the light spectrum, while the other half is in the near-infrared part with minor amounts in the ultraviolet, as depicted in Figure 2-1. The received radiation is measured in W/m^{2}nm just outside earth's atmosphere where air mass (AM) is zero. Radiant energy from the sun has a wavelength range of 300 to

4000 nm, which includes UV frequencies of 300 to 380 nm, visible light frequencies of 380 to 780 nm, and near infrared energy frequencies of 780 to 4000 nm.

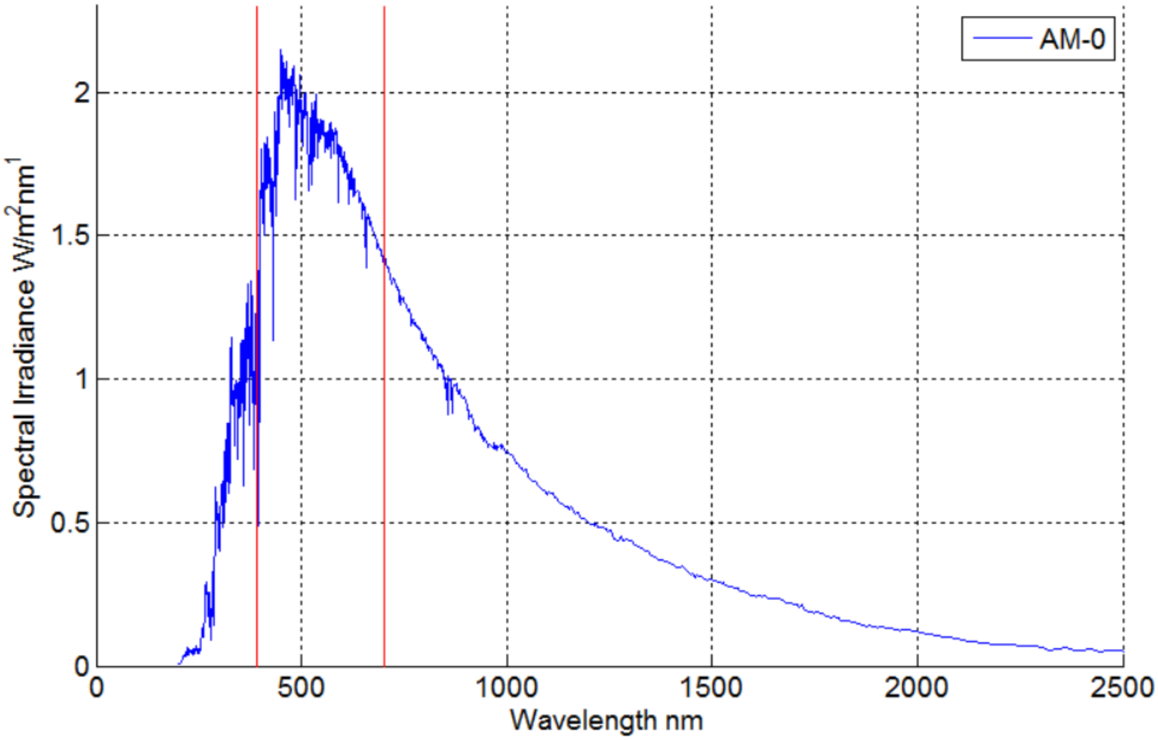

Figure 2-1: 2000 ASTM Standard Extraterrestrial Spectrum Reference E-490-00 (ASTM 2012)

Solar energy companies use solar spectrum data to better understand the amount of solar irradiance that can physically be delivered to the earth. The most significant measures that companies track are the intensity and energy delivered to the earth. The intensity of solar radiation is literally the amount of radiation hitting a surface which sums the energy contributed across the entire solar spectrum expressed in W/m^2 and is known as irradiance ($I_{incident}$). When given a dimensional surface the total irradiance can be calculated for the given surface area and is expressed in watts and is known as power. Throughout most of this report, however the energy per unit area is expressed in kWh/m^2 and is strictly used for solar based infrastructure design. This is a measure of irradiance on a $1m^2$ surface over a period of time.

2.2 Solar Panel Surface Orientation:

Although it may appear as though solar irradiance is distributed evenly over whole areas from a person's perspective, it is not the case in solar modules. After solar irradiance reaches earth's atmosphere, depending on the surface location, atmosphere will have an effect on the total irradiance that reaches the ground. Once past the earth's atmosphere the orientation of the surface absorbing the remaining solar irradiance must be analyzed. The orientation of a surface in solar calculations is known as the surface zenith angle (θ) ranging from 0 to 90 degrees. The zenith angle is the angle between the incident solar irradiance that will strike the surface and the normal of the surface. If the surface area in question is not perpendicular to the incident irradiance, where the zenith angle would be equal to zero, then the area will have to be larger to capture the same amount of irradiance. This concept is expressed as a single parameter (L) shown in Figure 2-2. Or in terms of fixed surface dimensions, such as solar panels, the total percentage of solar irradiance captured will be less than 100 percent, with direct respect to the zenith, as shown in Equation 1.

$$I_{\theta} = I_{0}\cos(\theta) \tag{1}$$

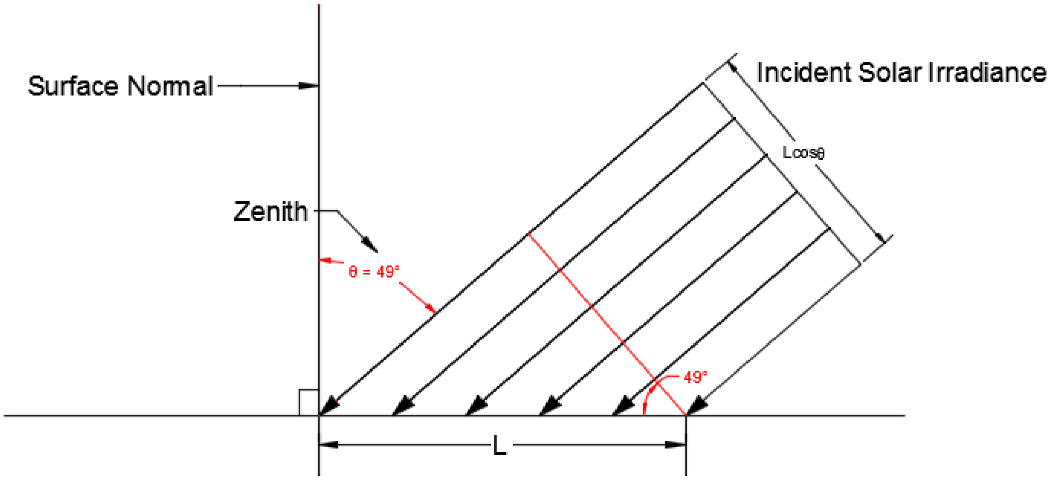

Figure 2-2: Effects of Zenith Angle on Irradiance

2.3 Atmospheric Air Mass:

Air mass is the coefficient that defines the direct path length of incident solar irradiance from just outside earth's atmosphere to ground surface relative to the zenith angle of the final surface area. The coefficient associated with AM helps characterize and refine the solar spectrum shown in Figure 2-1. Figure 2-1 expresses an air mass of zero (AM-0) which is the measure of intensity of solar radiation just outside earth's atmosphere. Figure 2-4 introduces two more very common intensity measurements that are used in solar analyses around the world. AM-1 and AM-1.5 are air masses which produce irradiance intensities of conditions inside of the earth's atmosphere seen with AM-0 in Figure 2-3. The number associated with the air mass is the length of the path through the atmosphere if the sun was in the apex of the day.

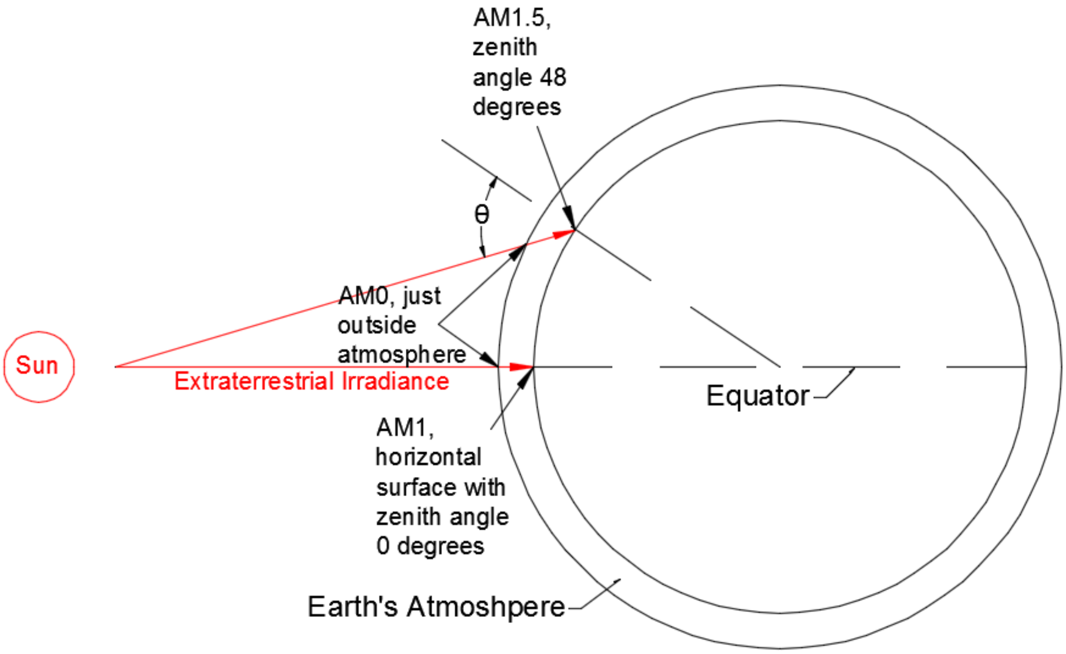

Figure 2-3: Relative Air Mass Locations (Green Rhino Energy 2013)

Earth’s Atmosphere does not simply lower the intensity by some fraction, but rather changes the entire solar spectrum distribution. Figure 2-4 shows that many, if not all, of the high energy wavelengths are much lower for AM-1 and AM-1.5G & D compared to AM-0. This is because most high energy wavelengths are blocked by the earth’s ozone layer. Although harmful to life on earth, the high energy reflected wavelengths are in reality a major loss to measured potential solar power on the surface below.

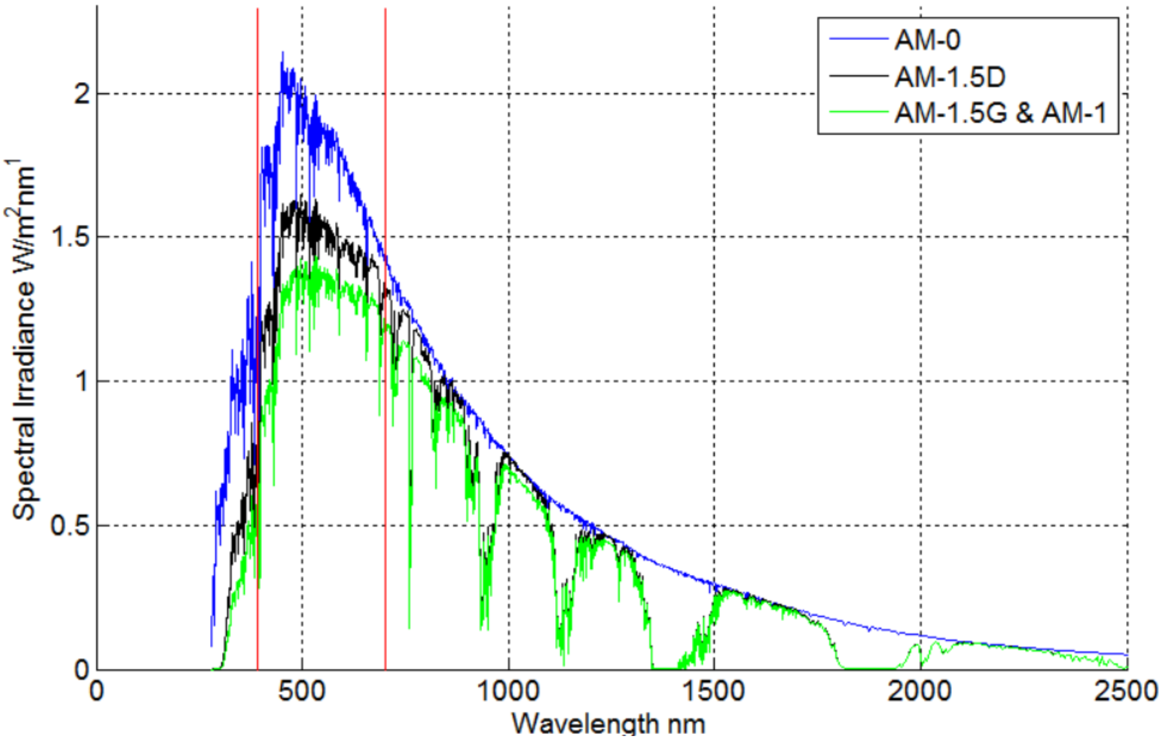

Figure 2-4: ASTM Standard Atmospheric Spectrums (ASTM 2012)

The remaining low energy wavelengths have interval drops in intensity for AM-1.5D, AM-1.5G, and AM-1 in the infrared spectrum of Figure 2-4. These lows occur because of a filter effect of tiny particles suspended in the air known as the attenuation effect or turbidity. There is a small percent difference in irradiance in the infrared portion of the light spectrum. The percent difference approaches zero as the wavelength of the incident light increases. This occurs because the wavelength of the light is greater and becomes unaffected by the scattering of the atmospheric particles. Irradiance intensity of an air mass can be determined at any time of day as expressed using Equation 2 and the zenith angle (θ), however, ASTM refers to air masses at apex only. Their intensities are from actual measurements, which are subsequently declared standard and follow as such in Table 2-1.

$$AM = \frac{1}{\cos(\theta)} \tag{2}$$

Table 2-1: Standard Air Mass Conditions and Intensities (Green Rhino Energy 2013)

NAME	AUTHORITY	DATA CONDITIONS	SOLAR INTENSITY (W/M^2)
AM-0	ASTM E490	just outside earth's atmosphere	1353
AM-1	CEI 85	sun directly overhead, (zenith=0), at sea level with horizontal surface	1000
AM-1.5G	ASTM G173-03	angled surface of 37 degrees, (zenith=48), facing due south, albedo 0.3, turbidity 0.29, @ 20 degrees Celsius	963.8 normalized to 1000
AM-1.5D	ASTM G173-03	same as AM-1.5G	768.3

AM-1.5G is the global radiation air mass. The conditions of AM-1.5G are the conditions used to represent the average of the entire lower 48 states of the United States. AM-1.5D is direct radiation air mass and reflects the conditions of a solar module perpendicular to the incident irradiance of the lower 48 states. It was concluded that 23% of the global horizontal irradiance for AM-1.5G is due to diffuse irradiance while 77% is due to direct irradiance at a total of 768.3 W/m^2 in Table 2-1. While at noon on a clear day, about 26% of the extraterrestrial radiation from the sun is scattered and absorbed as it passes through the atmosphere.

2.4 Atmosphere Effects on Solar Irradiance:

As mentioned before, as incident irradiance travels through the atmosphere, losses in intensity occur as expressed in the dips of AM-1.5G, AM-1, and AM-1.5D. The longer the irradiance travels through atmosphere, the more its intensity drops. These losses have been contributed to the effects of turbidity. But what exactly happens to the irradiance in atmosphere? A number of factors create minor reductions in irradiance and contribute to an overall noteworthy loss in intensity. Irradiance gets reflected, absorbed, and scattered by the atmosphere and light is split into direct and diffuse light through attenuation. It’s no surprise that the effects that cause reduction in intensity from earth's atmosphere are actually the same concepts that reduce intensity due to protective solar glass.

2.5 Solar Radiation on Earth's Surface:

Earth's axial tilt is the angle between the equatorial plane and orbital plane and changes over the year as the earth travels around the sun. Because of this tilt the earth constantly has a varying angular position to the sun over time. The angle is known as the declination angle of the earth and is the angular position of the sun at solar noon with respect to the plane of the equator. The angle varies from -23.45° to 23.45°over the course of one year and is expressed as (δ). The exact declination angle at any given day can be solved using Equation 3, where (n) denotes the number of days of a given year, where day 1 is January 1.

$$\delta = 23.45°\sin\left(\frac{360}{365} * (284 + n)\right) \tag{3}$$

Incident irradiance strikes the earth simultaneously all across the earth's surface. For locations other than the equator, the latitude (φ) is used in Equation 4 along with day (n), to determine the sun elevation angle (α) to account for changes in incident irradiance and accurately measure the incident irradiance of an entire day. Once elevation angle of the sun is known, Equation 5 is used to determine the zenith displayed in Figure 2-5. All angles tie together to obtain an intensity of irradiance on any given location on earth as seen in Figure 2-6.

$$\alpha = 90° - \varphi + \delta \tag{4}$$

$$\delta = 90° - \alpha \tag{5}$$

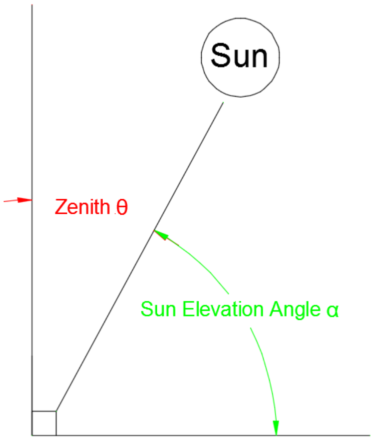

Figure 2-5: Sun and Zenith Angles with Respect to the Earth

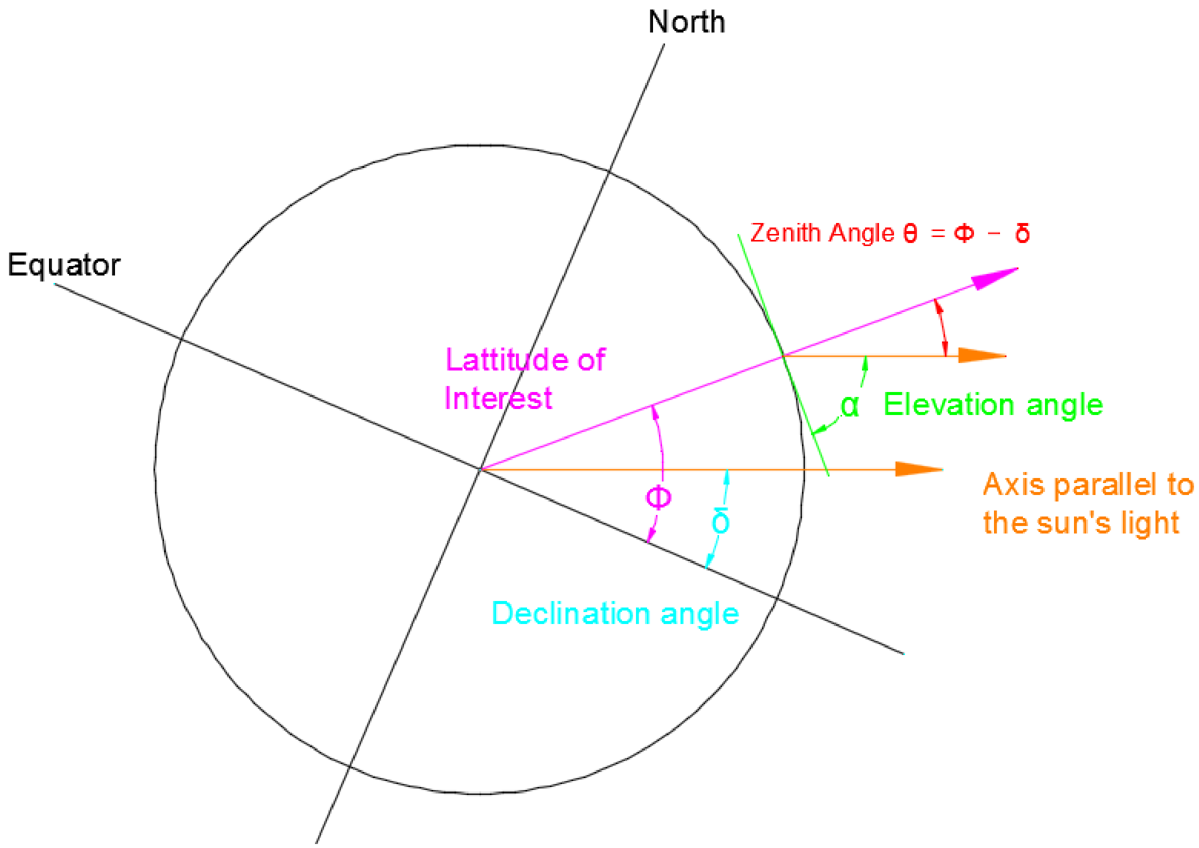

Figure 2-6: Solar Angles with Respect to the Sun (Green Rhino Energy 2013)

Figure 2-6 shows the tilt of the earth compared to the sun, given by the declination angle δ. Depending on the season δ can range from -23.45° to 23.45° as mentioned above. Figure 2-6 shows a maximum declination angle occurring at the summer solstice where Amherst, Massachusetts is nearest the sun and is the latitude of interest φ at 42° relative to the equator. The zenith angle θ can be seen geometrically as the angle between the incident irradiance and the latitudinal location angle.

2.6 Effects of Module Tilt on Solar Radiation:

Although the intensity of solar radiation is half the equation in producing higher amounts of energy, the angle between the solar module and the sun is just as significant in the design of a highly efficient system. By integrating solar technology into a walking surface, the design must be parallel to the plane of the earth's surface. When a solar module and incident radiation are perpendicular to one another the power density of both the surface of the module and the incident radiation are one in the same. Therefore, the power density will always be greatest when the module is perpendicular to the sun. But, because the angle between the sun's elevation angles α is continuously changing with time, the power density on a fixed solar module will always be less than 100%.

The solar walkway will be fixed parallel to the plane of earth and therefore will not receive the maximum amount of irradiance. Losses will occur due to the fixed flat plate design. A case study by Christiana Honsberg and Stuart Bowden has been used to determine exact percent loss of total irradiance due to a module tilt (β) equal to zero. Sample global horizontal irradiance (GHI) in the Northeast region of the United States was generated in laboratory settings throughout an entire year without cloud. The cloudless year allows for an exact representation of incident irradiance upon the Northeast so that exact percent loss can be calculated.

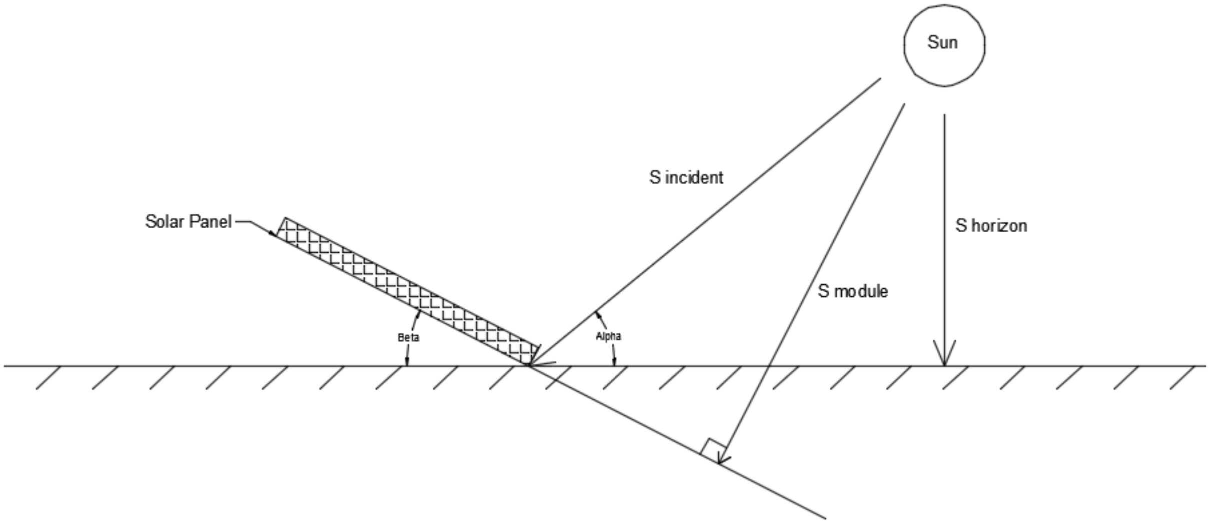

Figure 2-7: Incident irradiance on tilted surface geometry (Honsberg & Bowden 2014)

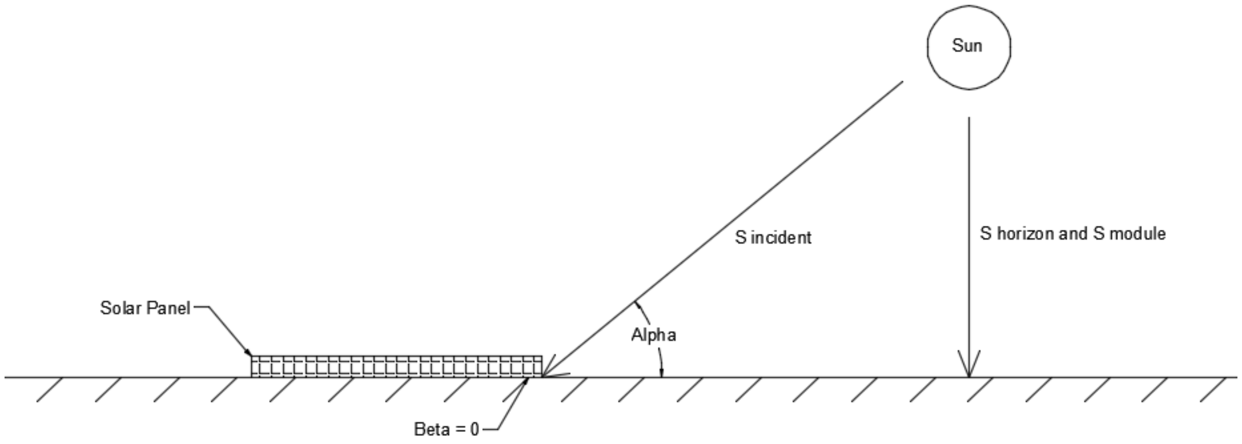

Figure 2-8: Incident irradiance on a flat surface geometry (Honsberg & Bowden 2014)

Figures 2-7 and 2-8 show how to calculate module irradiance by splitting incident irradiance into three unique light paths. Figure 2-7 along with Equations 6-8 shows how to calculate the irradiance incident on a tilted module surface (I_{module}), along with solar irradiance measured on a horizontal surface perpendicular to the sun's rays at all times ($I_{horizontal}$) given measured values of solar irradiance perpendicular to the sun ($I_{incident}$). The equations relating I_{module}, $I_{horizontal}$, and $I_{incident}$ are given below.

$$\mathrm{I}_{\mathrm{horizontal}} = I_{\mathrm{incident}} * \sin(\alpha) \tag{6}$$

$$I_{\mathrm{module}} = I_{\mathrm{incident}} * \sin(\alpha + \beta) \tag{7}$$

$$\mathrm{I}_{\mathrm{module}} = \frac{\mathrm{I}_{\mathrm{horizontal}} * \sin(\alpha + \beta)}{\sin(\alpha)} \tag{8}$$

The above equations were used to ultimately determine I_{module}, for an entire year, for both a flat angle module $I_{module0}$, to represent the solar bridge deck, and a module with a tilt β of 37° $I_{module37}$, to represent maximum efficiency of a stationary system in Amherst Massachusetts, latitude of 42°. The solar elevation angle α can be determined from equation 4 for any given day of the entire year. Figure 2-8 shows the geometry of a flat solar module. As the value of β approaches zero the $I_{horizontal}$ and I_{module} converge with one another. When β is equal to zero in Equation 7 it becomes identical to Equation 6. The following data used by Honsberg & Bowden from Equations 3-8 is shown in Figure 2-9.

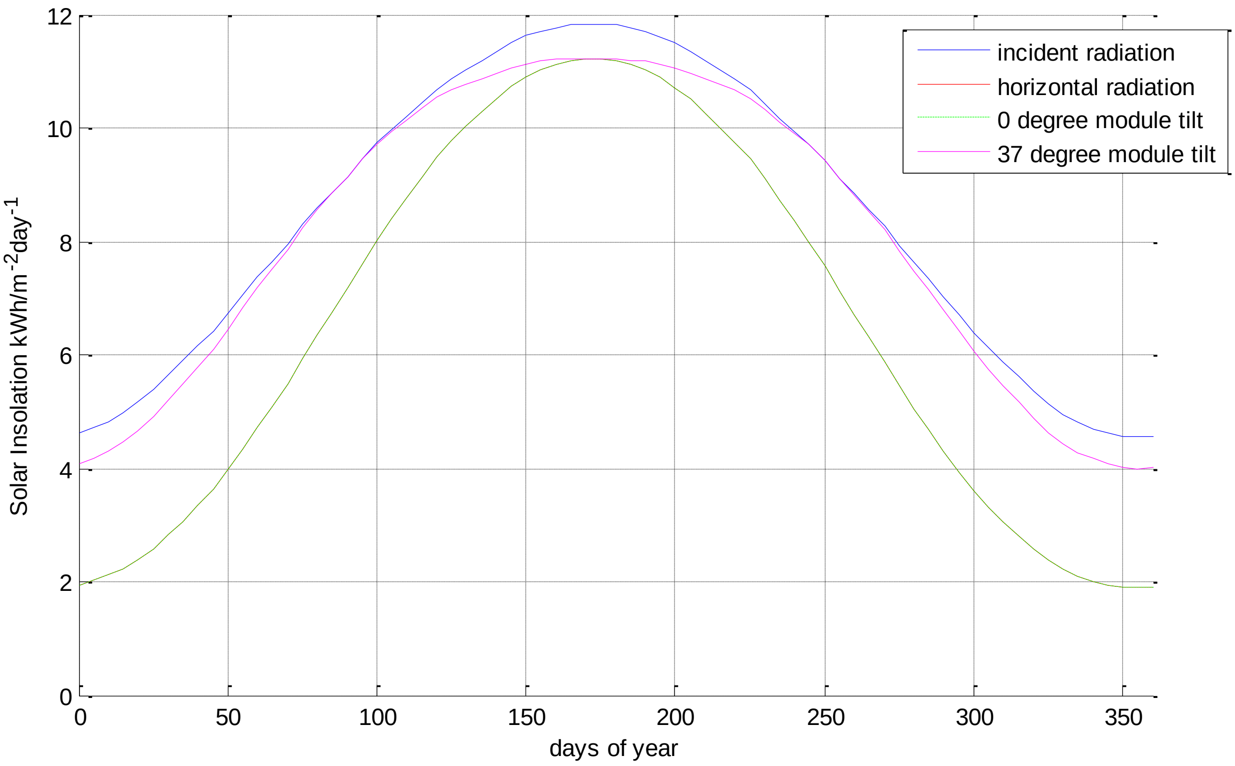

Figure 2-9: Solar irradiance received by varying module angles (Honsberg & Bowden 2014)

Figure 2-9 shows the effects of module tilt on the solar irradiance received throughout the year in kWh/m^{2}day without cloud. The $I_{incident}$ is the solar radiation perpendicular to the sun's rays and is what would be received by a module that perfectly tracks the sun and hence is the largest sum of solar radiation. $I_{horizontal}$ is the solar radiation striking the ground and is what would be received for a module lying flat on the ground as depicted in Fig. 9. Both the $I_{module0}$ and $I_{horizontal}$ are identical to one another throughout the year and confirm this notion. The values are regarded as maximum possible values at latitude 42° with AM-1.5G as they do not include the effects of cloud cover and are compiled in Table 2-2.

Table 2-2: Sum of Radiation

$I_{incident}$	614.28
$I_{horizontal}$	473.07
$I_{module0}$	473.07
$I_{module\ 37}$	591.52
loss due to module angle 0	22.9%
loss due to module angle 37	3.7%

From Table 2-2 a total loss in system efficiency would be 23% due to a module tilt angle of zero degrees in Amherst, Massachusetts latitude 42° with AM-1.5G. For the proposed fixed angle module, the maximum power over the course of a year is obtained when the tilt angle β is equal to the latitude φ of the proposed location and thus the proposed walkway will generate less than the maximum power over its lifetime due to its tilt angle.

2.7 National Solar Radiation Data Base:

The National Solar Radiation Data Base, NSRDB, has provided extraterrestrial solar irradiance intensities since 1961 and has updated its data collection systems over its course. From 1961 to 1990 the NSRDB collected solar radiation and meteorological data from 237 sites across the U.S. From 1990 to 2010 the number of sites rose to 1454 location, including U.S. territories. The last update in 2012 is comprised of data collection in 30 minute increments where all other previous data had been collected hourly.

The data examined in the solar analysis of this report is of this past year, January 1, 2014 through December 31, 2014. The NSRDB provides three types of incoming solar irradiance readings; Direct Normal Irradiance (DNI), diffuse horizontal Irradiance (DHI), and global horizontal irradiance (GHI). GHI was used for all calculations in determining PV electricity yield. The data provides monthly and annual average daily total solar irradiance. The irradiance values represent the resource available to horizontal flat plate collectors. Figure 2-10 shows a standard pyranometer used frequently for solar energy studies and climatology. These devices are commonly found at many meteorological stations, such as Barnes Regional Airport, where the solar data for this study has been obtained. The Barnes pyranometer is mounted parallel with the horizon and therefore collects data with the conditions of a flat plate solar module.

Figure 2-10: Standard Pyranometer (Hukseflux 2015)

Barne's pyranometer measures irradiance from the ground and therefore measures the exact irradiance absorbed by the ground or solar cell lying parallel with the ground. Unlike a clear sky model, described below, the pyranometer experiences cloud coverage and the losses associated with them. Barnes Regional Airport has both a pyranometer and clear sky model that collect data for the NSRDB. During the solar analysis of this thesis, it needs to be clear which collection of data belongs to which method. Pyranometer data will display a pattern of random periodic spikes in irradiance over time.

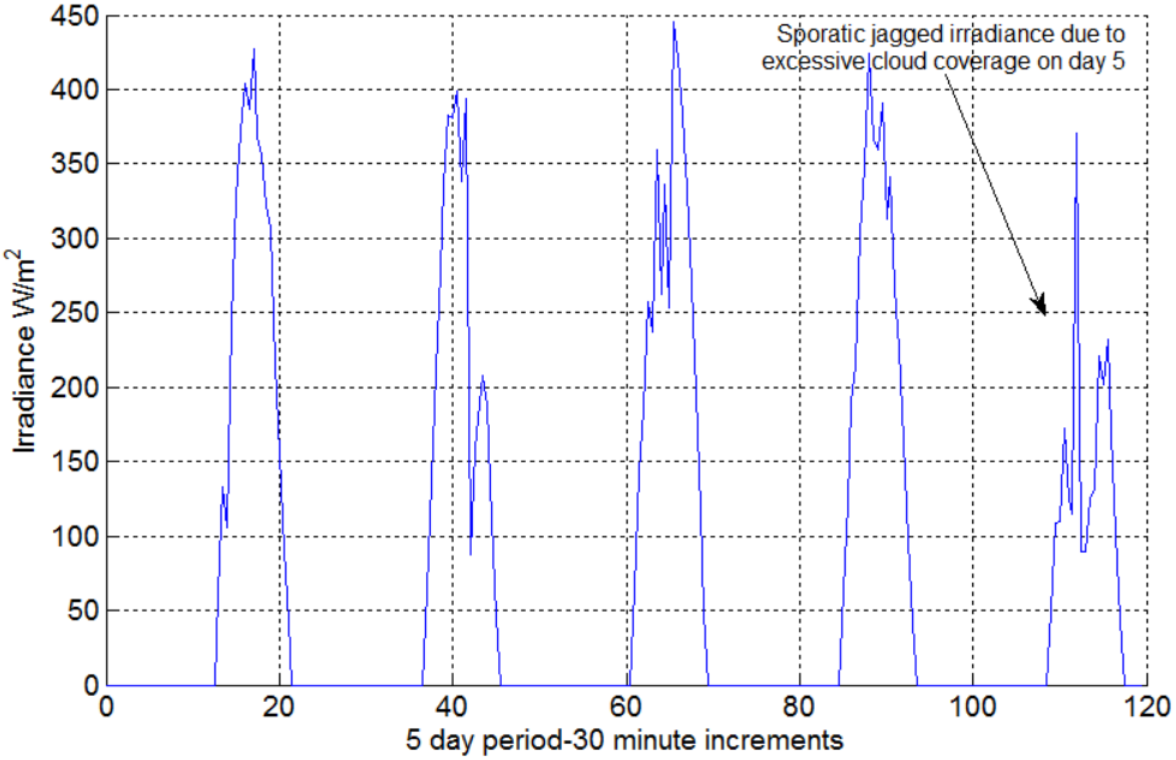

Figure 2-11: 5 Day Pyranometer data (Barnes Airport)

The jagged spikes in Figure 2-11 indicate periods of time where there was a blockage in the absorption of solar irradiance due to cloud coverage. Days of heavy cloud cover observed from time increments 110 to 118, create a very large loss in irradiance. In most time intervals only 50 percent of the peak irradiance was absorbed due to absorption and reflection effects of cloud coverage. The data used for this thesis has been confirmed to be obtained by use of a pyranometer at the Barnes Regional Airport and therefore losses due to annual cloud coverage for the photovoltaic electricity yield will not be factored into electrical yield equations.

2.7.1 Global Irradiance:

Global Horizontal Irradiance is the most important parameter for the calculation of photovoltaic electricity yield. In short, GHI is calculated by encompassing both direct normal irradiance (DNI) and diffuse horizontal irradiance (DHI). DNI is the irradiance component that reaches a horizontal surface of earth without any atmospheric losses due to scattering or absorption. DIF however is the radiation component that reaches a horizontal surface of earth as a result of being scattered by air molecules, aerosol particles, cloud particles or other particles. In a scenario where there is no atmosphere present there would be no diffuse horizontal radiation.

Ground reflected irradiance is the last type of categorized radiation which can be measured for study. However, because ground reflected radiation is usually insignificant compared to direct and diffuse, for all practical purposes global irradiance is said to be the sum of direct and diffuse radiation only and therefore ground reflected irradiance is assumed to be zero for all calculations. The mathematical equation 9 describes the relationship of DHI and DNI to obtain GHI.

$$\mathrm{GHI} = \mathrm{DHI} + \mathrm{DNI}\cos(\theta) \tag{9}$$

The following equation is used to calculate Global Horizontal Irradiance, where θ is the solar zenith angle. The zenith angle is the angle between the direction of interest of the sun and the zenith directly overhead.

2.7.2 Atmospheric Effects on Global Irradiance:

Even on a clear day, not all extraterrestrial irradiance reaches the ground. Generally at noon on a clear day, about 26% of the extraterrestrial radiation from the sun is scattered and absorbed as it passes through the atmosphere. Radiation which does travel through the atmosphere splits into diffuse and direct irradiance before striking the earth. In the morning and the evening, the reduction from the atmosphere increases due to the longer path through the atmosphere as seen in Figure 2-12. The geometry of the extraterrestrial irradiance path at noon and 5A.M. has two different air mass path lengths through the earth’s atmosphere. As the earth rotates, and the day becomes night, the extraterrestrial irradiance has to travel through more of the earth’s atmosphere to reach the surface. This longer path increases the percentage of diffuse and direct light absorbed by the earth’s surface.

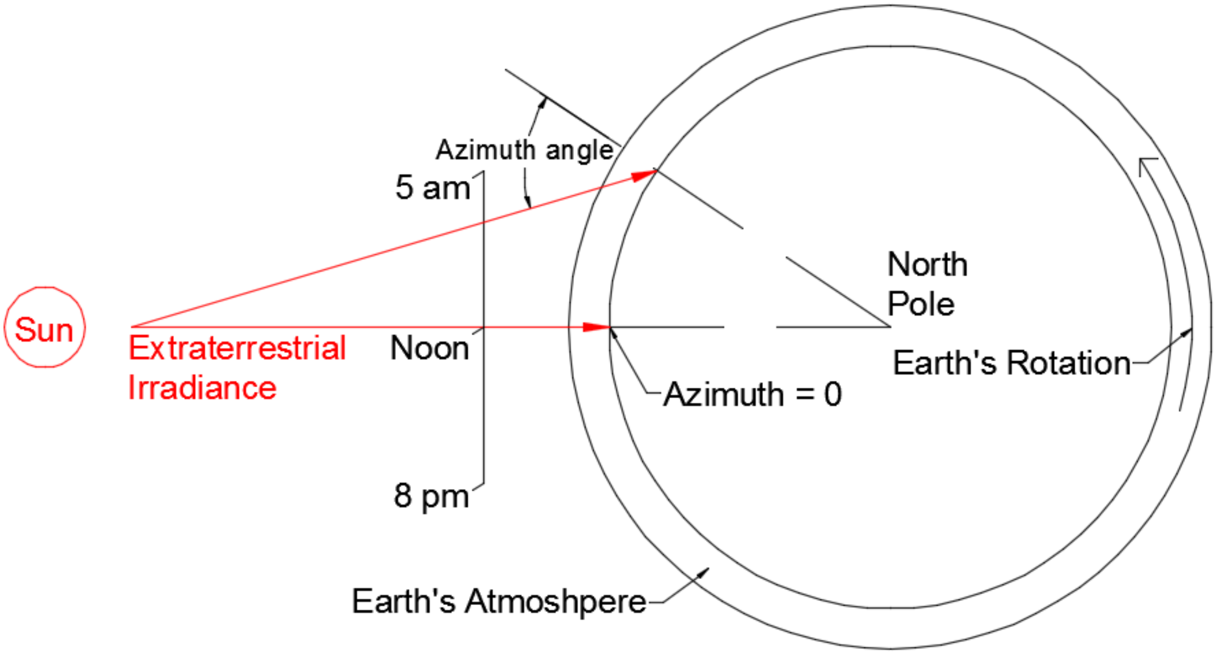

Figure 2-12 Effects of Global Positioning on Extraterrestrial Irradiance

Below in Figure 2-14 is a relation between the beam fractions of the NSRBD irradiance from January 1, 2014 to January 5, 2014. As expected, clear skies cause less diffusion of solar radiation, but when cloud cover is present, diffuse irradiance can be in excess of 50%. Cloud coverage creates losses in solar power generation by changing irradiance from direct to diffuse. In cases of solar modules, which have small surface areas to concentrate radiation, high percentages of direct irradiance are important to generate electricity. A full year analysis breakdown of irradiance collected at Barnes Airport is expressed in Figure 2-13. Amherst Massachusetts maintains a rather high percentage of direct light throughout the year. Although cloud coverage is consistent in the northeastern region of the United Sates, the overall effects of atmosphere and weather are reasonable for PV compatibility.

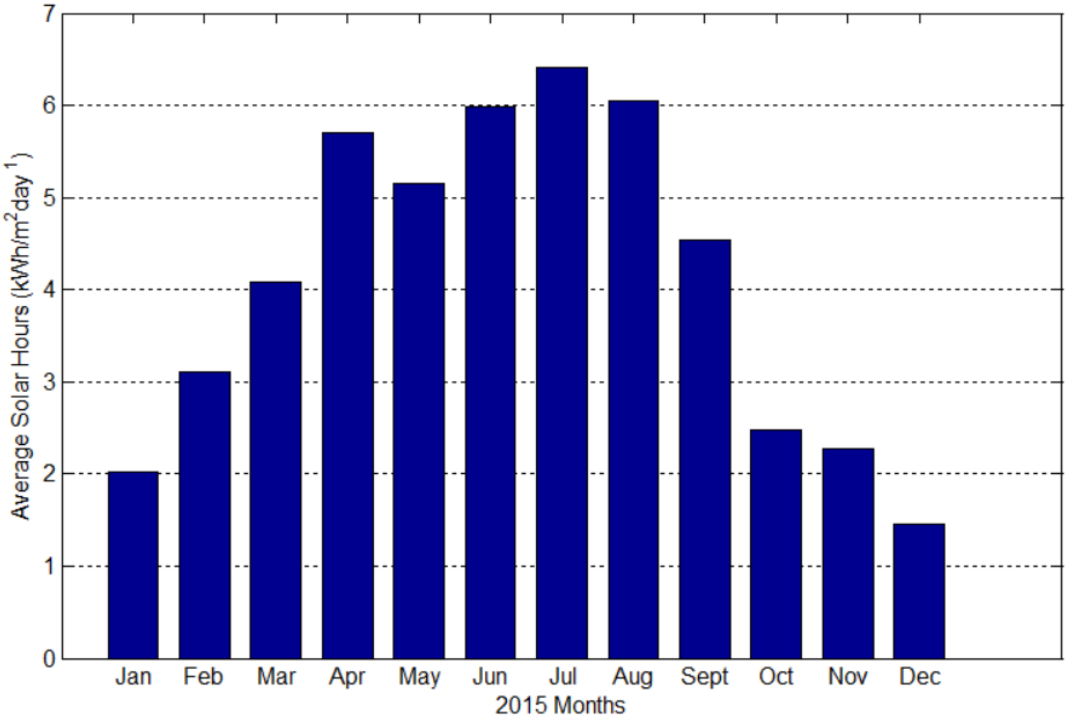

Figure 2-13: 2015 Average Monthly Solar Hours at Barnes Regional Airport (NSRDB 2014)

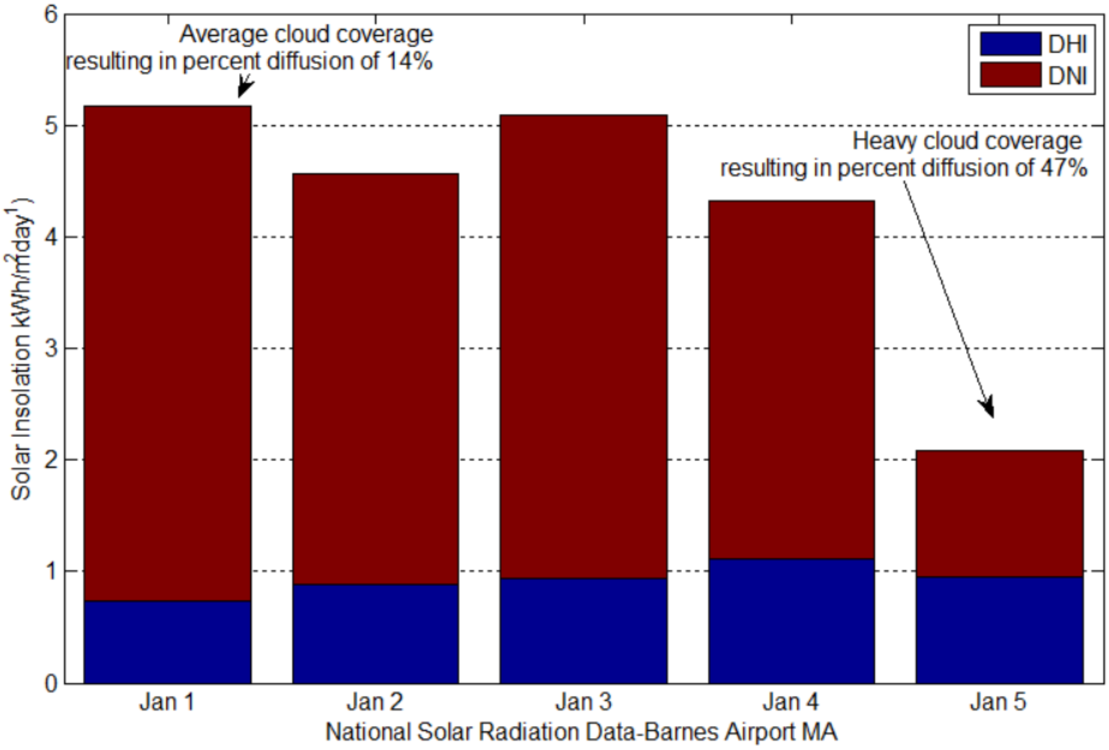

Figure 2-14: % Diffuse Irradiance due to cloud Coverage (NSRDB 2014)

2.8 Losses in Solar Irradiance due to Deck Integration:

Chapter 2 has made it abundantly clear that solar technology is in a constant struggle with ever changing global and atmospheric conditions. In short, solar walkways, and all current solar technologies, must find a way to reduce elemental and infrastructural aspects which decrease ability to absorb and convert irradiance into power. The idea of incorporating solar technology into walking surfaces only increases the likelihood of lower solar cell efficiency due to an increase in irradiant blocking elements.

With the introduction of elements such as increased tempered glass, advanced soiling, and complex cable and inverter designs, calculations along with accurate assumptions must be used to account for the added losses they include. Section 2.8 breaks down each power decreasing element of the solar deck design and obtains accurate losses for each to ensure the most accurate power yield of the proposed system.

2.8.1 Tempered Glass Thickness:

Incident light frequencies are the main parameters for a materials solar efficiency capability. While transmittance, absorption, and albedo are all parameters which explain why different glasses have different levels of efficiency, Incident light frequencies are used in lab to determine glasses and cells efficiency over a range of light frequencies mimicking the natural environment. Rarely does just a single frequency of light strike an object. While it does happen, it is more usual that visible light of many frequencies or even all frequencies is incident towards the surface of an object. When this occurs, objects have a tendency to selectively absorb, reflect or transmit light at certain frequencies.

Tempered glass is no different when it comes to interaction with light. Just like the effects the thickness of earth’s atmosphere has on incident irradiance, so too does the thickness of tempered glass protecting solar cells. Although necessary for a solar walking surface, tempered glass type and thickness reduce the amount of incident irradiance a solar cell receives. Technoglass tempered glass has a transmittance of 91% meaning that 91% of solar irradiance passes through the glass. This is a standard percentage for solar glass; however this percentage is justified for Technoglass with a thickness of 6mm. Because of the fear of fracture, the glass studied in this report is 12mm thick and is assumed to reduce the over power output by 10%.

2.8.2 Soiling:

As expressed in detail in earlier chapters, the radiation received by the cells of a photovoltaic module is only a fraction of what radiation is arriving to the module surface. Although laboratory testing boast high efficiencies outcomes for the latest commercial modules, real world factors are unfortunately not factored into the final efficiency of a PV system. One of the main causes of energy loss in a PV system is a combination of accumulated dirt, dust, pollution, snow, and seasonal pollen. The other contributors to losses include reflection and absorption of the PV cover glass. Soiling is defined as the percent loss of PV power due to the collection of a variety of airborne contaminates, both natural and manmade, which settle on PV systems, (Cano 2011) inevitably reducing radiation received by PV cells and ultimately reducing system efficiency.

Soiling is a much larger problem in desert conditions with the high presence of loose sand. Soiling in these extreme solar installation environments are being more closely studied, however soiling energy loss field data is scarce in the literature world. Since type of particle accumulation depends on the climate and the position and inclination of the PV module, the scarcity of data on energy losses is currently a problem. These problems can only be determined through site specific data analysis. Soiling losses for high traffic, high pollution areas with infrequent rain can cause anywhere from a 1-25% drop in efficiency (Cano 2011). Much of the studies conducted for soiling have occurred in the state of California in desert and polluted climates.

For northern locations, such as Amherst Massachusetts, snow can reduce the amount of energy produced by a PV module through a function based on the amount of snow received along with how long the snow remains in contact with the module. As temperatures drop, snow remains for a longer period of time. PV systems historically have prevented soiling due to snow with the tilt angles of the modules. Small PV array tilt angles, however, prevent snow from sliding off; such is the case of the solar bridge deck.

Soiling can be measured as either the rate at which contaminants accumulate on the module surface or the resulting decrease in production. Ultimately, determining the decrease in system performance due to soiling loss is the desired goal. Assuming all other factors remain constant, comparing actual electrical production values between a control subject and a soiled array is one way to determine soiling losses for a given site.

To simulate soiling losses over time the rate at which soiling accumulates must be determined. Although soiling rates can be calculated in a variety of ways, a soiling rate that represents the daily percent decrease in production is most valuable for the purposes of PV power analysis. Once a soiling rate for the site has been established, it can be used with rainfall data to estimate past, present and future soiling losses. This is because rainfall is the number one natural contributor to reducing soiling effects (Cano 2011).

2.8.3 Soiling Case Study:

In 2011 a study was conducted on the effects of soiling on PV power output at Arizona State University. In the study, daily insolation losses of soiled modules were determined at different module tilt angles. The losses were calculated using clean module power generation as a baseline. The experiment wanted to show a simply, yet effective, way of measuring losses due to soiling in comparison to perfect laboratory conditions, free of airborne debris.

Tilt angles from 0 to 40 degrees were used to show the effects of module tilt on the severity of soiling. The data calculated for a module angle of 0 degrees is used for further calculations in finding PV power generation for the proposed solar bridge deck as it is the closest angle to the proposed design. From January to March daily insolation was measured and recorded in Table 2-3 in Arizona.

Table 2-3: January to March 2011 insolation values and losses for clean and unclean solar modules (Cano 2011)

	0°	23°	33°
Clean	393.17	549.09	578.69
Soiled	385.24	543.33	573.11
Insolation Loss (%)	2.02%	1.05%	0.96%

Cano found that average losses due to soiling ranged from 2.02% to 0.69%, with a module of 0 degree tilt angle recording the highest losses of 2.02%. Of the horizontal solar modules, energy losses varied from 0.1 to 4.5% over the course of the experiment time, and all fluctuations were directly influenced by periods of rain showers shown in Figure 2-15. From

Cano's experiment it is clear that increasing module tilt decreases the percent losses due to soiling.

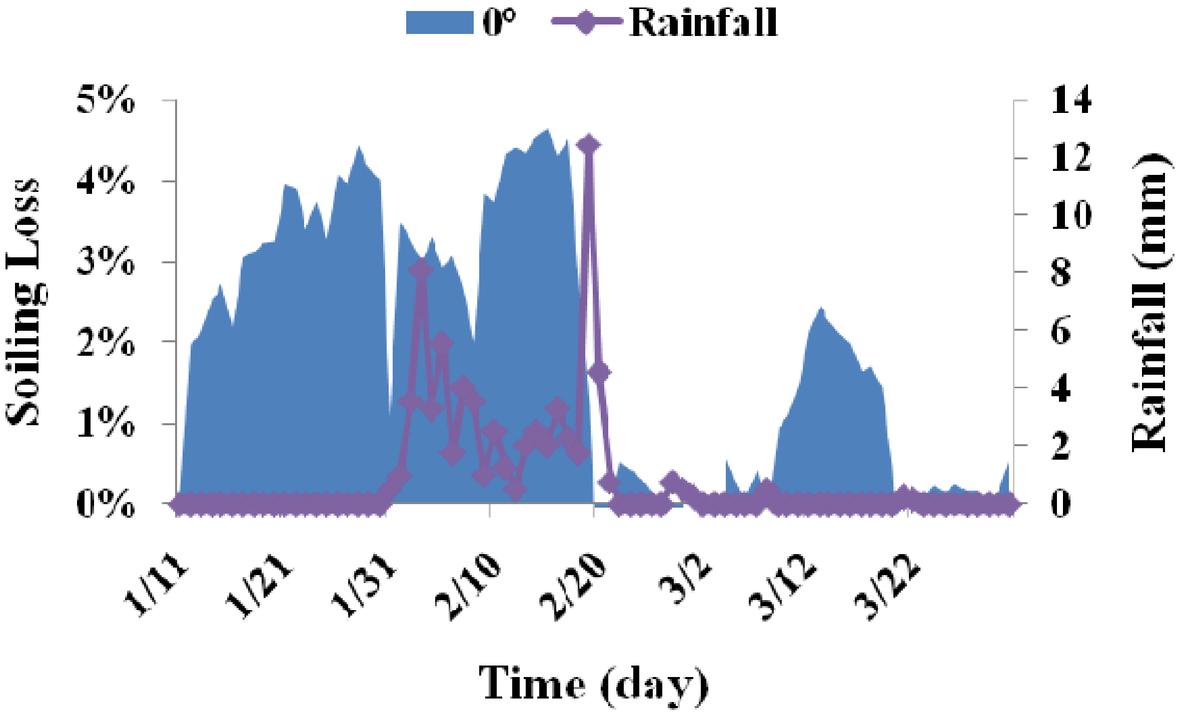

Figure 2-15: Average daily insolation losses for 0 degree tilt angle and total rainfall (Cano 2011)

It is important that soiling effects be monitored with either equipment or by visual inspection to ensure the proper power generation of a PV system. The experiment was conducted in Arizona and thus a much different climate then that of Amherst Massachusetts. Therefore certain assumptions are made in this thesis in order to properly estimate the potential power generation capabilities of the solar bridge deck. It is understood that the soiling effect is present at every module angle; however larger angles are shown to be much more effective at reducing soiling based on Cano's study. The loss in efficiency of 2.02% along with an added 8% in losses will be assumed for all data analysis of the solar output of the bridge deck. This assumption of an additional 8% accounts for the potential effects that seasonal changes may have on the soiling effect in Massachusetts as well as the excessive debris accumulation from pedestrian foot traffic. The Arizona climate has a far greater amount of dust content then Massachusetts, however Massachusetts must deal with drastic seasonal changes such as snow and leave cover, and therefore a far greater soiling loss of 10% is assumed.

2.8.4 Inverter vs. Micro-Inverter Configuration:

Solar inverters are electrical components of a solar system which convert direct current (DC) output into a national utility frequency of alternating current (AC). Prior to 2008 central inverters made up 100% of the solar market and they were lacking in efficiency. Complex cabling and one central inverter for a system meant that shading and minor panel damage caused massive losses in energy collecting capabilities of the solar system. Since 2008 and the introduction of micro-inverters, manufacturers and solar innovators have noticed critical advantages in these new micro-inverters. While cost remains an issue, the photovoltaic system adoption has exploded in recent years and the choice of using a central inverter vs. micro-inverter is becoming clear.

2.8.5 Inverter vs. Micro-Inverter Case Study:

Appalachian State University has conducted a study directly comparing the power produced by two identical solar systems in Boone North Carolina. Two systems were assembled of four Sharp NE-170 panels, one using a central inverter while the other used micro-inverters. Each system performed and was analyzed under ideal, no shade, conditions, and in partial shaded conditions. Power differences for the unshaded configuration for incident irradiance between 950 and 1050 W/m^2 are shown in Table 2-4 and shaded configuration in Table 2-5.

Table 2-4: Unshaded Power Differences (Lee, Raichle 2013)

POA (W/m^2)	**Micro Power (Watts)**	**Central Power (Watts)**	**Power Diff. (Watts)**	**Power Diff. (%)**
950	598	495	103	21%
960	607	504	104	21%
970	617	510	107	21%
980	618	510	108	21%
990	625	516	109	21%
1000	630	519	111	21%
1010	638	525	113	21%
1020	644	531	114	21%
1030	651	536	115	21%
1040	652	536	116	22%
1050	657	536	121	23%
average	**633**	**521**	**111**	**21%**

Table 2-5: Shaded Power Differences (Lee, Raichle 2013)

POA (W/m^2)	Micro Power (Watts)	Central Power (Watts)	Power Diff. (Watts)	Power Diff. (%)
950	602	478	124	26%
960	604	479	125	26%
970	609	482	127	26%
980	618	488	130	27%
990	618	487	131	27%
1000	626	493	133	27%
1010	633	497	136	27%
1020	641	503	138	27%
1030	649	505	143	28%
1040	651	506	145	28%
1050	661	515	146	28%
average	**631**	**495**	**135**	**27%**

Results from Table 2-4 show that the micro-inverters consistently outperformed the central inverter in power output by 20% across incident irradiance levels between 950 – 1200 W/m^2. Tabulated power differences for the shaded configuration for incident irradiance between 950 – 1200 W/m^2 are expressed in Table 2-5. Again, the micro-inverters outperformed the central inverter by a significant percentage. An average 27% increase in power output for irradiance values between 950 – 1200 W/m^2 was found. Researchers noted that the watts generated by the micro-inverters for both configurations were nearly identical, confirming that the micro-inverters were virtually unaffected by shading.

The study conducted at Appalachian State University found that one particular micro-inverter (Enphase D380) outperformed one particular central inverter (SunnyBoy 700U) in Boone North Carolina using 4 Sharp NE-170 solar panels. They were clear in stating that different micro-inverters and central inverters can produce varying results; however this one study represents a taste of performance comparisons between the two technologies and are consistent with previous studies surrounding the topic. With both cases it was clear that the micro-inverters outperformed the central inverter by a quantity $\geq$ 21% (Lee, Raichle 2013).

From the Appalachian State University study, it is concluded that micro-inverters will be used for in the design of the solar walkway. Common micro-inverters contribute to a typical loss in system efficiency of 5-15%. Today however, the top 25 most efficient solar panel micro-inverters on the market range from just 1.5-2% in efficiency loss. Therefore a conservative loss in efficiency due to micro-inverters will be 10% for the entirety of this thesis based on affordability. If costs were not factored into this thesis then an assumed 2% in system losses would be used. The 10% loss is assumed in all power generation calculations found in section 2.9.

2.9 Estimated Power Generation:

The idea of a solar walking surface was first brainstormed by answering a simple question. "What if every pedestrian walkway in the heart of the UMass campus was actually a flat laying solar panel"? The Heart of the UMass campus contains nearly 95,000 m^2 of walking surface and is defined as the portion of campus confined between Commonwealth Avenue, Massachusetts Avenue, and North Pleasant Street. With 21% efficient solar modules an average of 47,757 kWh/day would be produced. The next question was "What kind of impact does this create in the field of power conservation"? The University of Massachusetts, Amherst consumed on average 381,945.6 kWh/day in 2014 (UMass 2014). Nearly 13% of the entire campuses energy needs would be met due to solar walkways.

2.9.1 UMass Campus Average Global Horizontal Irradiance:

The solar cells used in the deck are monocrystalline silicon solar cells and are from a SunPower X21-345 module. Global horizontal irradiance expressed in (kWh/m^2 day) was calculated and summed into an average GHI per month of each of the twelve months of the 2014 season. GHI data was obtained from the National Solar Radiation Database at Westfield Barnes Regional Airport, Massachusetts. The data used is the most accurate data available to the public, and geographically is the closest data set to the proposed solar bridge at the University of Massachusetts, Amherst. Figure 2-16 shows average GHI for each month of the 2015 year starting from January and ending in December.

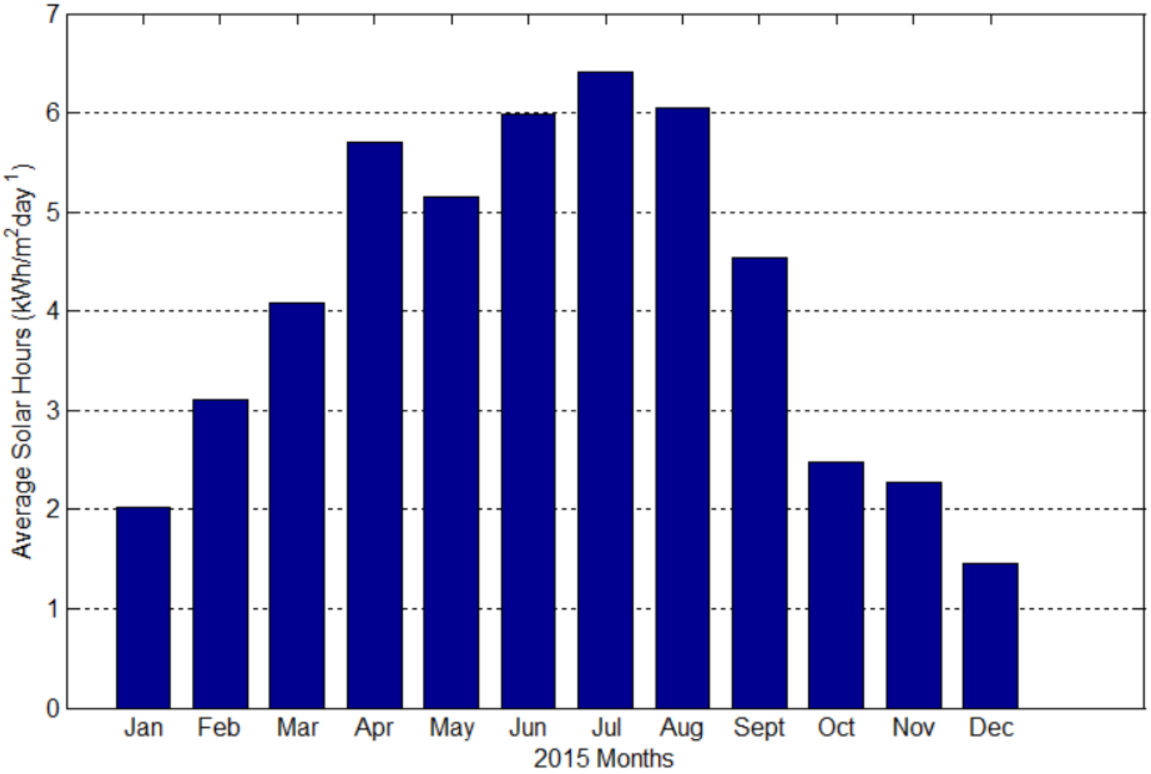

Figure 2-16: 2015 Average Monthly Solar Hours at Barnes Regional Airport (NSRDB 2014)

In standard testing conditions Figure 2-16 would appear as a perfect bell curve where winter months on either ends would produce lower average GHI while the middle summer months would produce progressively higher average GHI due to conditions explained in chapter 2. Figure 2-16 only shows a simplified interpretation of this. This is due to the technique used for data collection explained in full in chapter 2. Figure 2-16 shows ground GHI conditions under all weather conditions throughout the year with AM1.5, module tilt of 0°, and varying temperature conditions. Average GHI for the entire 2015 year in Westfield Massachusetts was calculated to be 4.1 (kWh/m^2 day) with a peak monthly average GHI of 6.4 (kWh/m^2 day) in July and low GHI of 1.4 (kWh/m^2 day) in December.

2.9.2 Panel Efficiency and Losses:

The SunPower X21-345 boasts a module power efficiency of 21%. With an average GHI of 4.1 (kWh/m^2 day), the SunPower X21-345 can harness 21% of the average GHI equaling 868 (Wh/m^2 day). 868 (Wh/m^2 day) is the expected best case scenario of power conversion for this module as its efficiency was determined in STC. As explained in chapter 2, this 868 (Wh/m^2

day) is if the SunPower X12-345 were to simply be placed on the ground with a module tilt of 0°.

Losses due to cables and inverters are 12%, glass roughness 10%, glass thickness 10%, and soiling 10%. These cumulative losses to energy generation result in a total potential power yield of 503 (Wh/m^2 day).

2.9.3 Bridge Deck Dimensioning:

The University of Massachusetts master plan shows a bridge spanning across the center of the current campus pond. The span is 250 (ft.) long or 76.2 (m). This is the main span of the bridge and the span length will house the solar walkway modules. The bridge deck is 15 (ft.) or 4.57 (m) wide producing a deck surface area of 348 (m^2). With this deck surface area and a total potential power generation of 503 (Wh/m^2 day) the proposed solar walking surface has a total power generation of 175.3 (kWh/day).

2.9.4 Lifetime Output Guarantee:

Overtime solar modules decay and lose efficiency. Solar companies, such as SunPower, have created warranties for their products in order to protect the consumer. Warranties cover conditions of the product and provide security for the amount of power generated by the modules. The SunPower X21-345 module has the best combined power and product warranty on the market and this coverage last 25 years, 15 more than traditional warranties. SunPower guaranties 95% power generation on average for the first 5 years of operation with a mere 0.375% decline per year to 25 years as compared to traditional warranties in Figure 2-17.

Figure 2-17: Module Warranty Comparison (SunPower Warranty Review 2013)

It is clear from Figure 2-17 that SunPower has a much higher guaranteed output of power over 25 years. With the company's guarantee of this power generation, calculations were completed in Appendix (F) which takes into account the SunPower warranty declination of 0.375% per year after 5 years at 95% operation. Under warranty parameters, the solar walking modules will produce 161.5 (kWh/day) on average over the course of 25 years. This number includes cell decay and also introduces the benefits of zero maintenance and replacement costs for faulty equipment. Tables 2-6 and 2-7 sum the total reductions in power yield due to walking integration challenges and total estimated power generation of the solar bridge deck‘s service life.

Table 2-6: Direct Losses due to Decking Integration

Losses	(%)
due to cables/inverter	12
due to glass roughness	10
due to glass thickness	10
due to angle of panel	0
due to soiling	10

Table 2-7: Lifetime Decking Power Generation and Capabilities

UMass average GHI (kWh/m^2*day)	4.11
Solar cell efficiency (%)	21
Solar cell yield (Wh/m^2*day)	867.88
Solar cell yield with losses (Wh/m^2*day)	503.37
Bridge deck area (m^2)	348.23
Bridge deck power generation (kWh/day)	175.29
Life time deck power generation (kWh/day)	161.5
Average daily energy consumption of street lamp (kWh/day)	3.5
MA household average daily Energy Consumption (kWh/day)	19
Lamps powered	50.08
Houses powered	8.5

On Average a standard pedestrian lamp uses a daily average of 3.5 (kWh/day). It is estimated that 50 pedestrian walkway lamps could be powered as long as the solar decking is operational. The bridge deck is 250ft long and does not require nearly 50 lamps or 8.5 houses. Therefore the solar decking produces more power than it needs to light itself, a small example of its sustainable capabilities. Amsterdam's SolaRoad is 100m long and roughly half the width of the bridge deck in this thesis. Its total square footage is about 52% of the solar bridge deck analyzed. SolaRoad states that its pilot has produced enough power to power roughly 3.5 homes, while the UMass solar bridge is estimated to power 7.5 homes. The square footage comparison suggests that the bridge deck should produce enough energy to power roughly 7 homes and that the predicted power yield is slightly high. The additional energy generation is due to the differences in solar irradiance of the two locations. Amherst, Massachusetts has higher annual GHI than Amsterdam and results in the additional power output of the deck system. Therefore SolaRoad's pilot has supported the accuracy of the solar analysis of the UMass solar bridge deck.

2.10 Solar Economics:

The world of solar technology is a small one compared to its counter parts such as oil, natural gas, coal, and nuclear power. Solar power has always been at the bottom of the power generating industry as its prices were sky high compared to the amount of power produced. Although environmentally green, producing zero carbon emissions or waste product, requiring little to no maintenance, and running on a limitless energy source, solar has gotten a bad reputation as being uneconomical. Since the early 2000's, high manufacturing costs of panels, along with extremely cheap fossil fuel utility costs, solar remained a commodity for the rich looking to go green. It was not however, a source of power that could be used to power a nation effectively.

This Chapter shows the factors which influence solar costs today. With prices in the power utility sector increasing steadily over the past decade and a greater interest in solar manufacturing and research, a new economical evaluation of solar is presented. This Chapter took six different solar panels of varying prices and efficiencies and determined total cost design, return of investment, and breakeven point.

2.10.1 Influence of Cost / Watt:

Each of the 6 panels varies in cost and efficiency. The solar panel efficiency rating measures what percentage of sunlight hitting a panel gets turned into electricity. High efficiency doesn't mean better, it just means you use less space for the solar array. Efficiency isn't usually a big concern unless there is an unusually small space for the solar panels. Typical solar panel efficiency rating is around 14-18%. Sun Power is the leading solar manufacturer in the world of highly efficient solar panels available commercially. Their X21-345 model of 21% efficiency is currently the most efficient in the world for commercial use. The 6 panels range in efficiency of 21%-14% as seen in Table 2-8. The prices per panel however ranges drastically from just over $1000 to $200.

Table 2-8: Solar Panel Types

Solar panel types	Company Name	Product name	Efficiency (%)
Monocrystalline	Sun Power	X21-345	21
Monocrystalline	Solarworld	Sunmodule plus mono silver 285w	17
Polycrystalline	Solarworld	Sunmodule pro-series 255w poly	15.1
Monocrystalline	Panasonic	240w mono black	19
Polycrystalline	Q Cells	280w poly	17.1
Polycrystalline	Suntech	275w Poly XL	14.2

It is clear from Figure 2-18 that the higher a panel’s efficiency of converting sunlight to energy the higher the cost to make it. This trend is due to the quality of the panels. Each of the 6 panel types are silicon based, but half of the panels contain a key difference that drives manufacturing costs up as well as panel efficiency. Sun Power, Solar World, and Panasonic all have panels which use monocrystalline cells while the other three use polycrystalline cells. Monocrystalline cells require a more refined and complex manufacturing process to create. They also have a higher temperature coefficient, meaning that they can maintain high efficiency under high temperatures, where polycrystalline cells begin to lose efficiency as temperatures increase. Lastly monocrystalline cells produce more power per area, hence resulting in higher efficiency. What Figure 2-18 shows however is that although monocrystalline efficiency are much higher and more power is produced, the costs associated with those cell improvements are not worth the percent increase in cost.

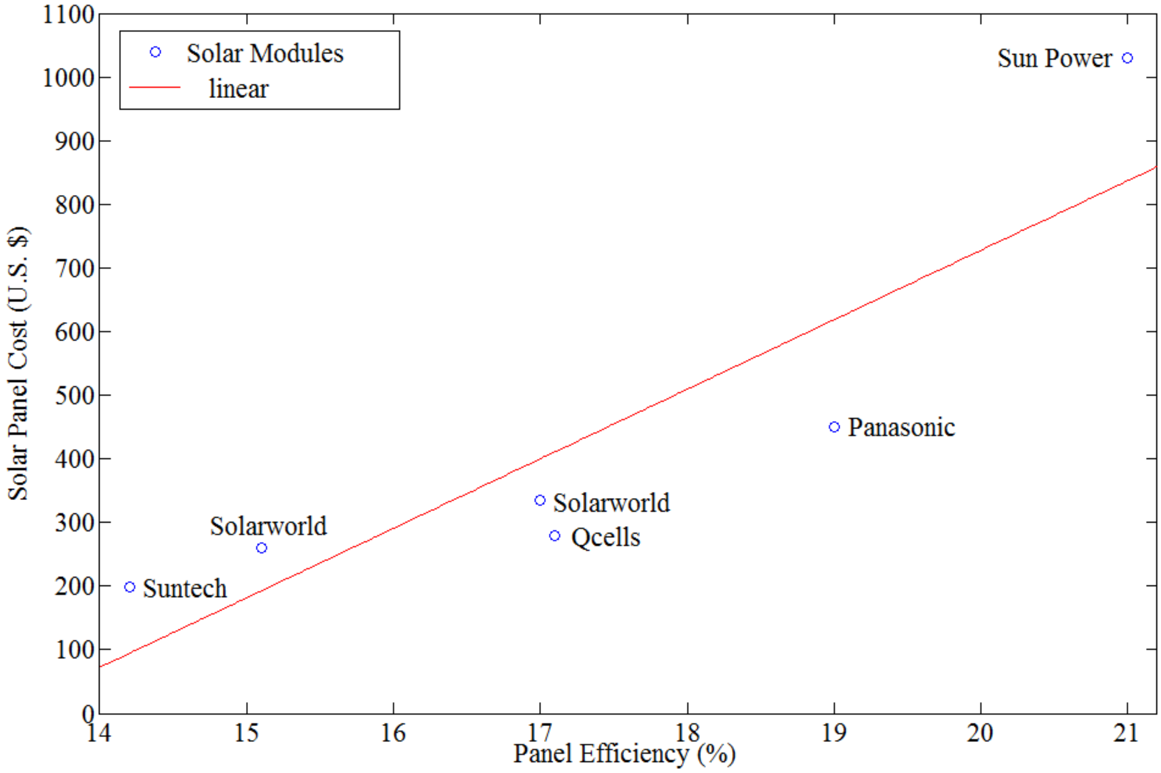

Figure 2-18: Panel Efficiency vs. Cost

From 19% efficiency to 21% efficiency there is a 128% increase in cost. While an efficiency jump from 15.1% efficiency to 19% has an increase in cost of 73%. Therefore higher cell efficiency does not mean an economically superior cell.

Panel cost vs. panel efficiency however, is not the only factor which influences solar economics. Panel sizes and peak watt output of both standard test conditions (STC) and PV USA test conditions (PTC) heavily determine a panel’s economic feasibility. Therefore solar companies have concluded that all these factors boil down into a simple unit known as cost per watt. Cost per watt compares the capital cost of various forms of solar technologies, and it refers to the number of dollars needed to buy a solar device capable of generating one watt of electricity. From Table 2-9 it is clear that the panels with higher efficiencies and greater panel area generate more peak watts. This notion is simple, however cell quality is the other major influence in a panels cost per watt. While STC shows a panel’s peak watt generation in perfect laboratory conditions, PTC shows what a panel can actually produce in a true environment.

Table 2-9: STC & PTC Analysis

Panels Size (m^2)	Efficiency (%)	Cost per panel (U.S. $)	Peak Watts (STC)	Peak Watts (PTC)	Peak Watts Maintained
2.12	21	$1,030.50	345	320.2	92.81%
1.67	17	$335.00	285	257.6	90.39%
1.67	15.1	$260.00	255	223.2	87.53%
1.26	19	$450.00	240	223.5	93.13%
1.67	17.1	$280.00	280	251.8	89.93%
1.93	14.2	$199.00	275	249.3	90.65%

Table 2-9 shows that the cheaper panels produce a greater amount less then stated in STC conditions. Their ability to perform in a true environment is hindered more so then the more expensive quality cells due to temperature changes, and other natural factors, however the percent fluctuation in maintained peak wattage (5.5%) is still far insignificant compared to the percent increase in cost per panel of 73%. The price per watt of all 6 examined panels is presented in Table 2-10 from most expensive to least expensive.

Table 2-10: Solar Equipment Cost per Watt

Company Name	product name	Cost per Watt
Sun Power	X21-345	$2.99
Panasonic	240w mono black	$1.88
Solarworld	Sunmodule plus mono silver 285w	$1.18
Solarworld	Sunmodule pro-series 255w poly	$1.02
Q Cells	280w poly	$1.00
Suntech	275w Poly XL	$0.72

The costs per watt shown in Table 2-10 do not include inverters, racks, wiring, marketing, or installation. The costs are simply that of the solar panels sold in industrial quantities.

2.10.2 Cost of Design:

Careful analyses of 6 different solar panels were analyzed in Section 2.10. While all different in size, efficiency, cost, and peak watt generation, the cost per watt was used to compare the capital costs. Final capital costs per watt are presented in Table 2-11.

Table 2-11: Capital Cost per Watt

Company Name	Product Name	Cost per Watt
Sun Power	X21-345	$4.96
Panasonic	240w mono black	$3.11
Solarworld	Sunmodule plus mono silver 285w	$1.95
Solarworld	Sunmodule pro-series 255w poly	$1.69
Q Cells	280w poly	$1.66
Suntech	275w Poly XL	$1.20

The Costs in Table 2-11 include theoretical installation costs and overhead profit. Traditionally installation and overhead add another 66% in additional costs in the solar market today. The total capital costs of both the solar equipment costs and total installed costs for the 250ft campus bridge deck are presented in Table 2-12 below.

Table 2-12: Theoretical Bridge Decking Cost

Company Name	Solar Equipment Cost	Installed Deck System Cost
Sun Power	$169,002.00	$280,543.32
Panasonic	$124,200.00	$206,172.00
Solarworld	$69,680.00	$115,668.80
Q-Cells	$58,240.00	$96,678.40
Solarworld	$54,080.00	$89,772.80
Suntech	$35,820.00	$59,461.20

Although Sun Power's X21-345 model is the most efficient model on the market today, its manufacturing costs are far to sever for the extra quality and power it provides. Although it can be argued with more efficient and reliable cell design, that lifetime maintenance and repair costs would be far less. It is believed for this thesis that the severely high cost of the Sun Power modules will never allow the offset in maintenance costs to create a substantial dent in the cost per watt. The previous statement is not supported as fact, however, and a more in depth economic lifetime analysis would have to be presented for the scenario. That analysis was not conducted and is not presented in this thesis; however engineering judgment was used and took into account the probability of cell damage and more frequent maintenance over the solar slabs lifetime depending on the cells used. Therefore a median cell type was chosen for the design.

The Solar world Sunmodule plus mono silver 285W will be was chosen to be the best module to be integrated into the decking system. Although it does not have the lowest capital cost, its slightly higher cost utilizes monocrystalline silicon solar cells which are much more resilient then cheaper polycrystalline cells. The module is one of Solarworld's best models and with a high temperature coefficient ensuring the system will perform at specified efficiencies more so over there lifetime.

2.10.3 Return of Investment:

The Solarworld Sunmodule plus mono silver 285W was chosen as the optimum solar tech for the decking system. However, for economic relevance, the six panels will continue to be compared for return of investment (ROI) calculations and breakeven calculations. Table 2-13 shows compared module ROI values.

Table 2-13: Return of Investment

Company Name	Installed Total System Cost (U.S. $)	System avg. yearly power output (kWh/yr.)	Avg. Annual Savings (U.S. $)	Lifetime Savings (U.S. $)	ROI (%)	With Tax Credit ROI (%)
Sun Power	$280,543.32	58948	$12,261.18	$306,529.60	9.26%	63.89%
Solarworld	$206,172.00	52195	$10,856.56	$271,414.00	31.64%	97.47%
Solarworld	$115,668.80	46815	$9,737.52	$243,438.00	110.46%	215.69%
Panasonic	$96,678.40	47092	$9,795.14	$244,878.40	153.29%	279.94%
Q Cells	$89,772.80	41610	$8,654.88	$216,372.00	141.02%	261.53%
Suntech	$59,461.20	39106	$8,134.05	$203,351.20	241.99%	412.98%

Although total system cost is important in economics, the highest cost does not always mean the most expensive. ROI is a performance measure used to evaluate the efficiency of a solar investment or to compare the efficiency of a number of different solar investments. ROI measures the amount of return on an investment relative to the investments cost. Because ROI is measured as a percentage, it is easily used to compare with returns from other energy industries, both sustainable and unsustainable alike.

From Table 2-13 it is observed that Panasonic's solar modules have an initial capital cost higher than that of Q Cells. At first glance one would think to purchase Q Cells as it costs less money upfront. However ROI shows that over the investment's lifetime Q Cells actually return less overall profit. While Panasonic costs 7.7% more than Q cells initially, Panasonic produces 12.3% more ret urn.

The Solarworld Sunmodule plus mono silver 285W has a ROI of 110.46% concluding that even with a decrease in solar performance due to decking integration, the system is still economically self-sufficient. More so, the state of Massachusetts has a tax credit to all solar projects in the state. This credit reduces the initial total capital cost of any system by 33% until 2016. Table 2-13 shows this included credit and resulting ROI. With significant reductions in capital costs, the ROI of the Solarworld Sunmodule plus mono silver 285W is increased to 215.69%.

2.10.4 Breakeven Point:

The final economic evaluation needed for the design is its breakeven point. This is the time in which the system will pay back the amount equal to that of what it cost to create it. After this point the system will produce profit. Table 2-14 shows the breakeven dates in years of the six system types.

Table 2-14 Module Break Even Point

Company Name	Installed Total System Cost	Avg. Power Generation (kWh/Day)	Revenue	Break Even Date (Years)	Break Even Date With Tax Credit (Years)
Sun Power	$280,543.32	162	$33.59	22.88	15.25
Panasonic	$206,172.00	143	$29.74	18.99	12.66
Solarworld	$115,668.80	128	$26.68	11.88	7.92
Q Cells	$96,678.40	129	$26.84	9.87	6.58
Solarworld	$89,772.80	114	$23.71	10.37	6.92
Suntech	$59,461.20	107	$22.29	7.31	4.87

Without Massachusetts state tax credit, the Solarworld Sunmodule plus mono silver 285W has a breakeven time of roughly 12 years. This is nearly half of the systems design operating lifespan. With the tax credit included the breakeven time is roughly 8 years, or 1/3 of the systems operating lifespan. Although the number of years may seem long for a simple "money back" investment, these numbers in terms of solar systems are a good thing. A solar system is designed today with a 20 – 25 year service or power guarantee warranty. This means the manufacturers are confident that their product will last at least that given time while still producing power. Therefore 12 years at worst, is nowhere near a systems potential for failure and a breakeven point of 12 years is well worth the investment with little to no risk involved.

CHAPTER 3

PROPOSED STRUCTURAL GEOMETRY AND AASHTO LRFD PARAMETERS

Using the University of Massachusetts master plan, a bridge is called to be erected across the campus pond. The “Ellis Way Arc” will extend through the main heart of the campus, including the campus pond. The future bridge site will be used as a case study for the implementation of solar technology into walkway surfaces by using the bridge decking as its surface. A theoretical sketch of the University of Massachusetts’s “Ellis way bridge” is presented in Figures 3-1 through 3-4 in order to create boundary conditions for analysis of the bridge deck.

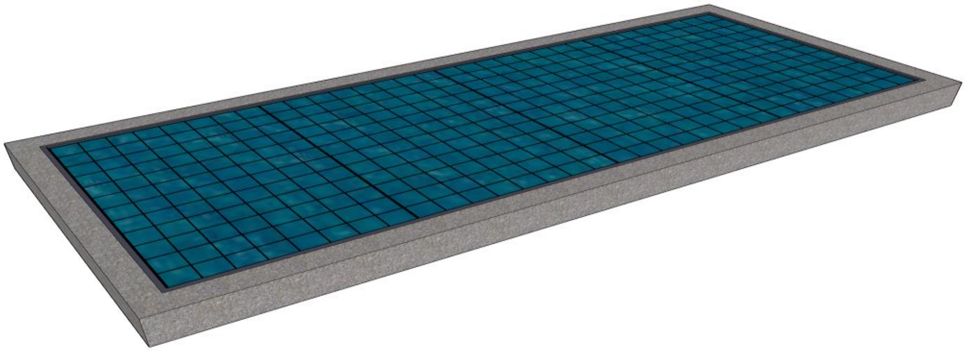

Figure 3-1: Solar Slab Concept Art

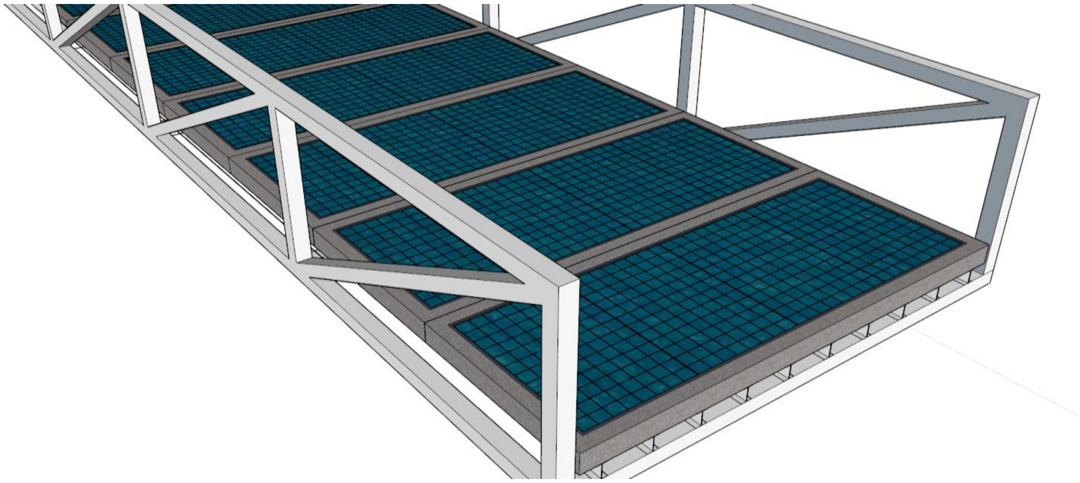

Figure 3-2: Solar Decking Concept Art

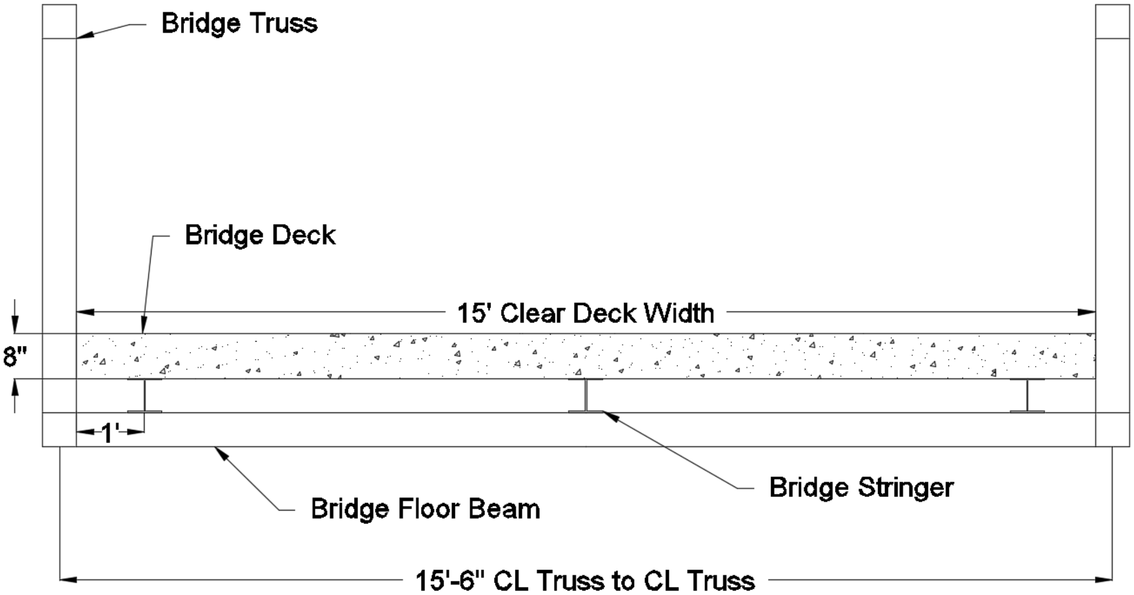

Figure 3-3: AutoCAD Front View

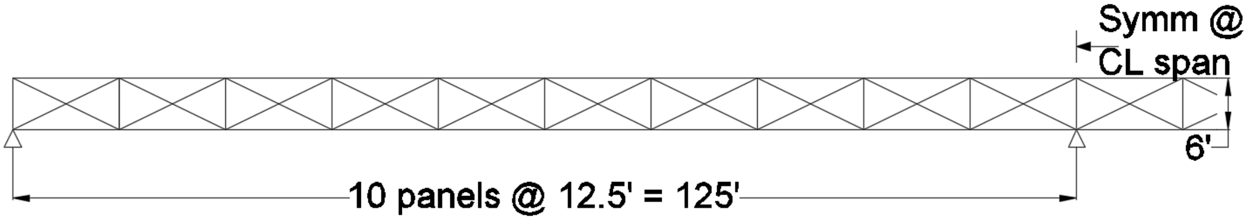

Figure 3-4: Side View of Proposed Bridge

The bridge superstructure spans 250ft across the campus pond, is supported at a mid-span of 125ft, and is simply supported at both ends. The truss design for the main support system is completely theoretical and is only presented for a visual representation of the superstructure for the reader. The load bearing main supports will not necessarily be composed of a truss system and is up to the discretion of the University of Massachusetts. The proposed solar bridge decking will be supported with a series of calculated I-beam stringers running longitudinally along the bridge seen in Figure 3-2.

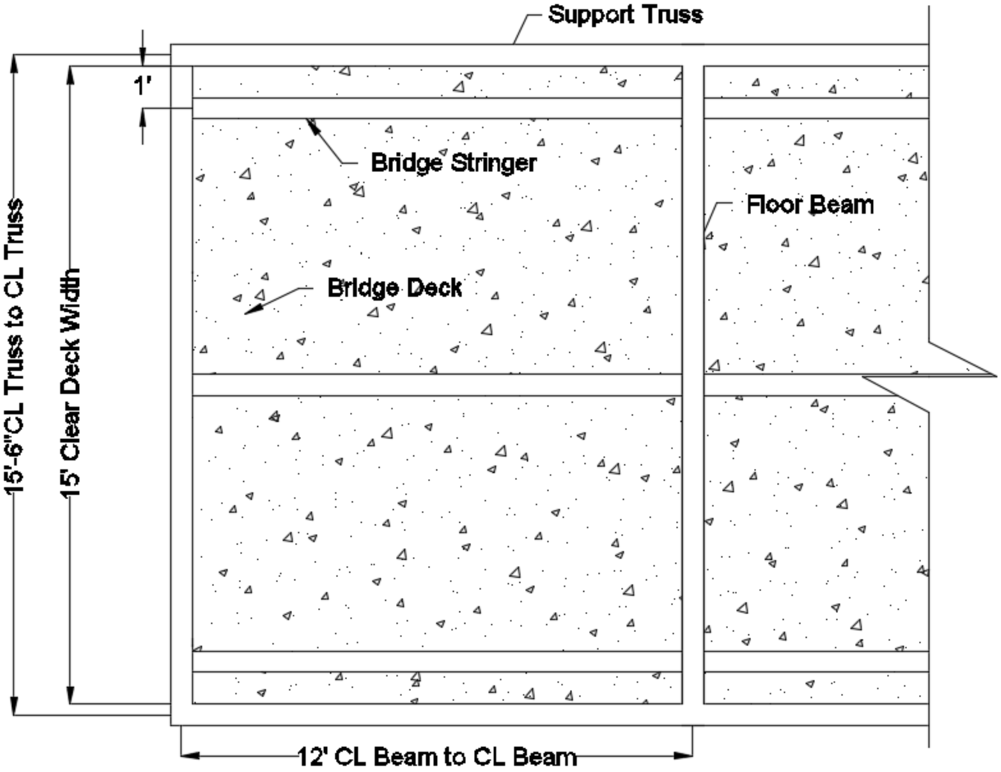

Figure 3-5 Bottom View of Bridge Superstructure

Running perpendicular to the stringers are structural hollow metal floor beams seen in Figure 3-5. As recommended by AASHTO LRFD the clear deck width is 15ft from interior truss edge to interior truss edge. Floor beams run every 12.5ft creating 10 panels, or bays, as displayed in Figures 3-4 and 3-5.

The decking is comprised of rectangular concrete slabs which house the solar modules seen in detail in Figure 3-6. The Slab is a 177in x73.4in x8in and houses four X21-345 series solar panels comprised of 96 solar cells each. The full slab contains 384 solar cells. The slab is comprised of various materials layered on top of one another along with all solar module electronics seen in Figure 3-7.

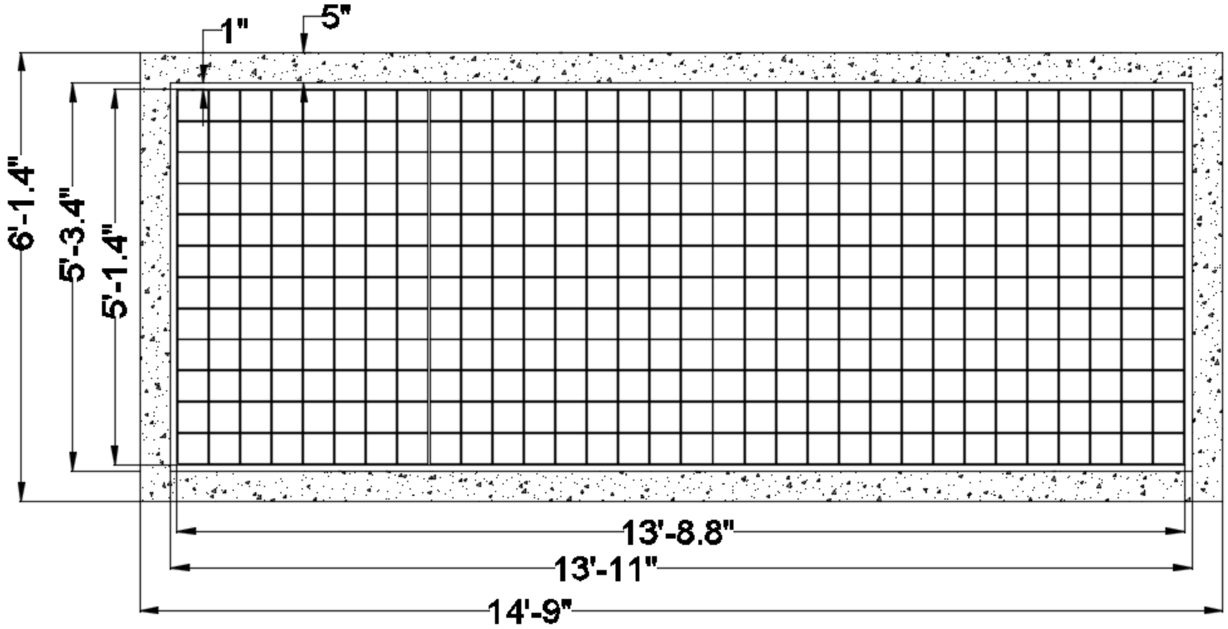

Figure 3-6: Solar Decking Slab

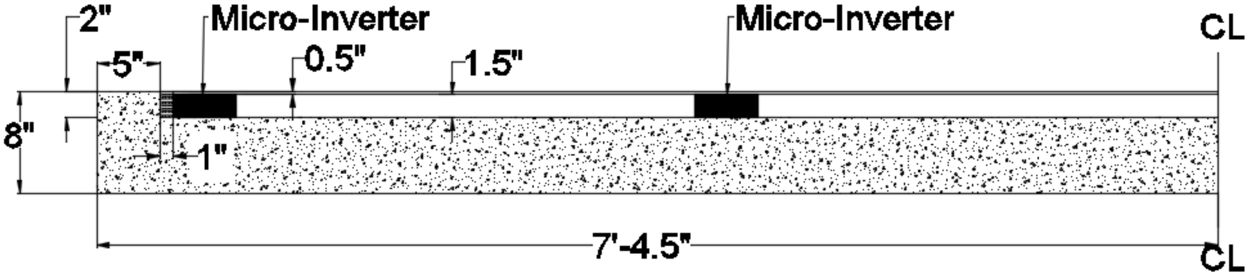

Figure 3-7: Cross Section of Solar Deck Slab

The solar panels are set down below the perimeter concrete slab. The perimeter slab edge is a total of 8" high and thickness of 5". The total depth of the slab was determined through design slab calculations using a clear deck width of 15ft, strip length of 12in, pedestrian live load of 90psf, and a slab dead load of 87.5psf.

The interior depth of the concrete is 6" leaving a 2" depression in the center of the slab to house the solar panels. The X21-345 series solar panels are 1.8" in height and largely consist of the micro-inverters dimensioning as seen in Figure 3-7. Above the 6" concrete slab will be 1.5" of material types with varying modulus's of elasticity. These tested materials will be in direct contact with the concrete slab below and the solar panels above to directly transfer load cases. Above the testing material lies the solar panels and tempered glass. The tempered glass is 12mm (.47") thick and protects the 300μm thick solar cells below. All edges where concrete contacts solar panels will be 1" thick expansion joint material as seen in Figures 3-6 and 3-7.

3.1 AASHTO-LRFD Load Specifications:

The Guide Specifications address the design and construction of typical pedestrian bridges which are designed for, and intended to carry, primarily pedestrians, bicyclists, equestrian riders and light maintenance vehicles, but not designed and intended to carry typical highway traffic.

The Guide Specifications provide additional guidance on the design and construction of pedestrian bridges in supplement to that available in the AASHTO LRFD Bridge Design Specifications (AASHTO LRFD). Only issues requiring additional or different treatment due to the nature of pedestrian bridges and their loadings are addressed. All loading parameters are addressed below in individual sub-sections and are then compiled into one table at the end of section 3.1.7 and used for all modeling load cases throughout this report.

3.1.1 Pedestrian Loading:

As per AASHTO LRFD pedestrian loading guidelines, the bridge is designed for a uniform pedestrian loading of 90psf. This loading will be patterned to produce the maximum load effects, while consideration of dynamic load allowance is not required with this loading. For the main support members, (trusses) the deck area is the non-zero influence surface for all components of the design. A 90psf without impact is the pedestrian live load for this case. Secondary members such as the deck, stringers and floor beams are designed using a pedestrian load of 90psf without impact according to AASHTO LRFD.

3.1.2 Snow Loading:

AASHTO states that snow loads should be considered when a bridge is located in an area of potentially heavy snowfall. Traditionally snowfall occurs at high elevations in mountainous areas where seasonal accumulation occurs, such as the Continental U.S. Northeast region. In other areas of the country, snow loads are as large as 700 lb. /ft^2 and therefore must be checked if it controls in cases of bridge deck loading.

AASHTO specifications do not require consideration of snow loads except under special conditions (AASHTO 3.3.2). The effects of snow are assumed to be offset by an accompanying decrease in vehicle live load as is with pedestrian load. As stated above, this assumption is valid for most structures, but is not realistic in areas where snowfall is significant like the Northeast. When prolonged winter closure of a bridge makes snow removal impossible, the magnitude of snow loads may exceed those from vehicle live loads and pedestrians. The applicability and magnitude of snow loads are left to designer judgment (Ritter 1990).

Snow loads vary from year to year and depend on the depth and density of snow pack. The depth used for design is based on historical records and the maximum recorded depth of the State of Massachusetts. Density is based on the degree of compaction in Table 3-1.

Table 3-1: Probable Snow Fall Density (Ritter 1990)

CONDITION OF SNOW PACK	PROBABLE DENSITY (LB./FT^3)
FRESHLY FALLEN	6
ACCUMULATED	19
COMPACTED	31
RAIN ON SNOW	31

The lightest accumulation is produced by fresh snow falling at cold temperatures. Density increases when the snow pack is subjected to freeze-thaw cycles or rain, a common occurrence in Massachusetts (Ritter 1990). Probable densities for snow pack conditions for the design will be a worst case scenario, classified as rain and snow with a density of 31lb/ft^3 when snow has sat over a long period of time, and 19lb/ft^3 for accumulated snow after storms.

Estimated snow loads from historical records display an average high seasonal snowfall of 14.9 inches and a record snow depth, snow that’s on the ground at any one time, of 53 inches (National Weather Service). This produces a rain and snow load of 38.5lb/ft^2 and a worst case scenario accumulated snow load of 84lb/ft^2. AASHTO recommends that snow loading not be accounted for in design loading except in cases of the country where snow accumulation is high. State weather records have been concluded AASHTO’s assumption to be true for the state of Massachusetts. Even during the record setting winter season of 2014 -2015, snow loads did not exceed the 90psf pedestrian loading of the proposed bridge and do not control.

3.1.3 Vehicle Loading:

As per AASHTO LRFD, the vehicle loadings specified are equivalent to the H-trucks shown in article 3.6.1.6. Although stated in this thesis that the bridge would possess permanent physical methods for preventing vehicle assess, AASHTO LRFD states that in such cases where this is not the case, the bridge shall be designed for a maintenance vehicle load equivalent to the H-truck shown in Table 3-2 and displayed in Figure 3-8 for the strength I load combination unless otherwise specified by the owner.

Table 3-2: AASHTO LRFD Pedestrian Design Vehicle (AASHTO LRFD 2009)

Clear Deck Width (feet)	Design Vehicle
7-10	H5
≥ 10	H10

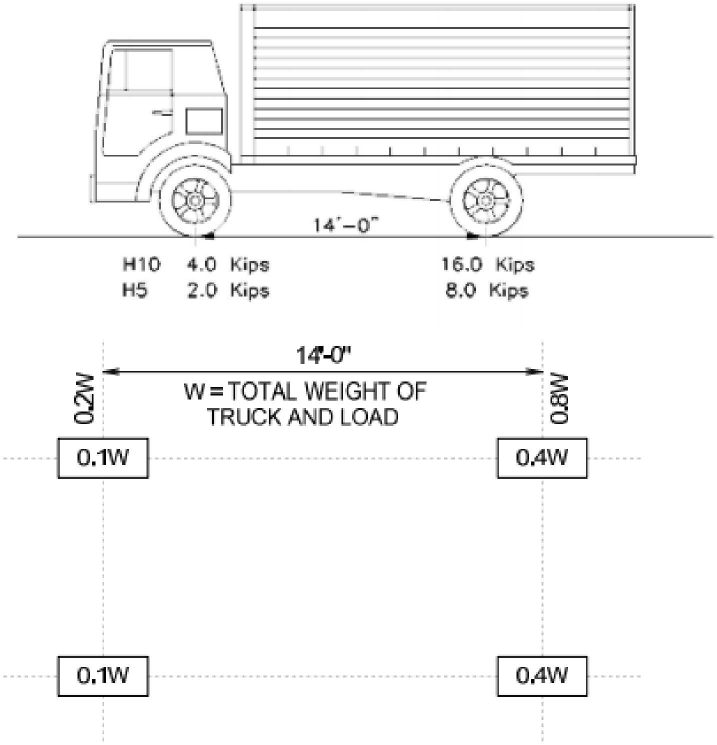

Figure 3-8: Design Vehicle Load Configuration (AASHTO LRFD 2009)

The clear deck width is over 10 feet so the design vehicle will be an H10 truck per AASHTO LRFD design with a front axle loading of 4kips and a rear axle loading of 16kips. A single truck shall be placed to produce the maximum load effects and shall not be placed in combination with the pedestrian load. The dynamic load allowance is not considered for this loading. However with restricted entry points at both entrances of the bridge, AASHTO states that vehicle loadings can be specified by the owner in special cases.

3.1.4 Special Vehicle Loading:

There will in no situation ever be an H10 classified truck crossing the proposed bridge. Therefore an appropriate vehicle was chosen for design purposes per the engineer's discretion. A GEM eL shown in Figure 3-9 is the maximum vehicle load that will cross the proposed bridge. Fully loaded the vehicle weight is 2300lb. Based on vehicle layout and orientation of load carrying capabilities, the vehicle's load configuration has a front and rear axle loading of 1.15kips as seen in Figure 3-10.

Dry Weight	1,285 lb
GVW	2,300 lb
Payload Capacity	1,015 lb
Width	55"
Length	144"
Height	70"
Cubic Feet of Cab	47 ft³
Wheelbase	114"
Turning Radius	17 ft
Ground Clearance	8"
Tires	12-inch
Range* Up to 30 miles. Range on all Polaris® electric vehicles will vary depending on temperature, grade, payload and driving style.	
Top Speed	25 mph

Figure 3-9: Proposed Special Case Vehicle Loading (Polaris Industries 2014)

Figure 3-10: Special Case Vehicle Load Configuration (Polaris Industries 2014)

The vehicle loading parameters shown in Figure 3-9 will be used for all AASHTO LRFD vehicle loading cases throughout the remainder of this thesis. Any additional vehicle classes that the owner deems necessary to include can and will be analyzed in later dates and reports.

3.1.5 Equestrian Loading:

AASHTO LRFD has specified a unique case for all pedestrian bridge designs intending to carry occasional equestrian loadings. A single point load analysis of 1kip/16in^2 will be included in the loading parameters for all tests conducted in this thesis. The equestrian load is a live load intended to ensure adequate punching shear capacity for pedestrian bridge decking.

3.1.6 Wind Loading:

The proposed bridge shall be designed for wind loads as specified in the AASHTO Signs, Articles 3.8 and 3.9 unless otherwise directed by the owner. A vertical uplift line load of 0.020ksf as specified in AASHTO LRFD Article 3.8.2 shall be applied. This line load is determined as the force caused by a pressure of 0.020ksf over the full deck width and is applied at the windward quarter point of the deck width.

3.1.7 Load Cases:

Table 3-3: Load Cases (AASHTO LRFD 2009)

	AASHTO		Proposed	
Pedestrian Live Load	90psf		90psf	
Vehicle Live Load	front axle	rear axle	front axle	rear axle
7ft-10ft	2kip	8kip	1.15kip	1.15kip
>10ft	4kip	16kip	1.15kip	1.15kip
Equestrian Live Load	1kip/16in^2		1kip/16in^2	
wind load	0.020ksf		0.020ksf	

3.2 Pedestrian Bridge Deck Design Considerations

There are a number of design considerations that are unique to every bridge design. While many considerations are similar for many bridges, they usually rely on the specific geometry of the bridge and thus must be considered carefully. Presented below are cases thought to be hazardous to the design of a deck slab, and are deemed necessary to check for safety.

3.2.1 Thermal Expansion:

Every material has thermal expansion properties. Thermal expansion is an increase in linear dimensions of a solid in response of change in surrounding temperature through heat transfer. Thermal expansion differs between materials, and can also differ between the same materials depending on the conditions it is exposed to. The loose chemical composition of a material on a molecular scale, high temperatures, and fast cooling rate increase the thermal expansion of glass.

The proposed bridge decking will consist of a concrete shell housing the solar modules and protective cover glass. Because the decking slabs house a large single pane of glass, thermal expansion may be a potential problem and is addressed below. As stated above high temperatures and rapid cooling rates are two main causes of thermal expansion in glass and these conditions will occur in the outdoors of the Northeastern United States. Equation 10 is used to determine the thermal expansion of the tempered glass of the design. It must be checked that the thermal expansion of the glass does not come into contact with the surround concrete due to rapid temperature change from sun down to sun up, and during the peak of the summer months when the heat of the solar modules is at their highest.

$$\Delta L = Lo\lambda\Delta T \tag{10}$$

Where Lo is the linear dimension in question, λ is the thermal expansion coefficient of the tempered glass, and ΔT is the change in temperature. The design glass is 1560mm by 4185mm and a worst case scenario of 100°C in temperature change is used. Note this change in temperature has never been recorded in any weather patterns in the Northeast Region of the United States; however, it’s used to ensure that any potential case is checked. The thermal expansion coefficient of tempered techno glass is 9 @ 20°C (K^{-1}) or (10^{-6} °C). Equation 10 determined the thermal expansion for tempered techno glass to be 1.4mm (0.055in) and 3.77mm

(0.148in) in the short and long dimensions respectively. There will be a one inch expansion joint material between the glass and concrete on all sides of the design allowing for a combined expansion capability of one inch. Therefore it is concluded that thermal expansion of the glass, under even the most sever temperature conditions, will not create unwanted stresses within the glass, or warping of the glass potentially causing fracture.

3.2.2 Concrete Cracking:

The precast concrete slab must be checked for potential long term cracking caused by structural loading. The reinforced concrete slab was checked for cracking both along the top face and bottom face. These two faces are where cracking is most likely to occur first. A calculated cracking moment of 2kip*ft was found while a maximum applied moment due to structural loading was 2.6kip*ft and -1.81kip*ft. Therefore since the applied positive moment of 2.6kip*ft is greater than the cracking moment, cracking will occur over time along the bottom face of the slab, while cracking will not occur along the top face of the slab because the cracking moment is greater than the negative moment of -1.81kip*ft applied.

3.2.3 Punching Shear:

AASHTO LRFD uses an equestrian loading parameter for pedestrian foot bridges as a way to check for extreme cases of punching shear. Punching shear was checked against a generated shear, due to equestrian loading, of 1.86kips. The shear force needed for punching to occur is 3.64kips. The applied shear force is much lower than the punching shear limit and therefore there is no need for shear reinforcement. This result is mostly due to the increased thickness of the concrete slab of the decking, severely increasing the force needed to induce shear failure.

3.2.4 Overturning:

Wind loads acting on the substructure generate lateral and longitudinal forces that produce the same effects associated with centrifugal and longitudinal forces. They are most significant for continuous or multiple-span structures supported by high piers or bents. Because the proposed design is low to the ground surface and only consists of two spans, many of the wind loads can be ignored based on this and the AASHTO LRFD pedestrian bridge guide.

AASHTO specifications (AASHTO 3.15.3) require that the wind forces tending to overturn a bridge be computed in some loading combinations. When overturning is considered, the wind loads applied to the superstructure and substructure are assumed to act perpendicular to the longitudinal bridge centerline. In addition, a vertical wind load is applied upward at the windward quarter point of the transverse superstructure width. The vertical wind load is equal to 20psf of deck or 0.02ksf as shown in Table 3-3. The vertical wind load on the full superstructure applied at the windward quarter point is 300 pounds per linear foot (plf). The vertical load on the leeward truss is thus 225plf and 75plf on the windward truss. This loading case would be taken into account for design of the complete bridge superstructure, however this thesis does not contain that work and in conclusion the overturning forces were checked, and will only be used further for deck vibration checks.

3.3 Deck Materials:

The desire to provide a durable and long lasting solar slab is the main concern of this thesis. While concrete bridge decks are susceptible to premature cracking and to corrosion of reinforcing steels, it is assumed that the concrete slabs are precast off site and delivered to the University construction site in final form. Therefore, the main focus of this thesis's material selection is determining what variations of intermediate decking materials can most effectively transfer AASHTO LRFD loadings from the solar cell modulus above through to the concrete slab below without maximizing stresses within the solar cells seen in Figure 3-11. Tables 3-4 through 3-6 display the material properties of a single solar deck slab, minus the intermediate material in question.

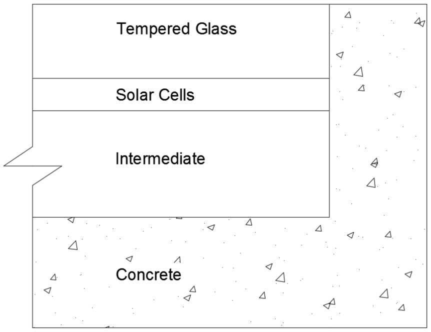

Figure 3-11: Slab Cross Section (not to scale)

Table 3-4: Solar Silicon Properties (Hull 1999)

Material	Silicon
model	isotropic elastic
Young's Modulus	165GPa
Poisson's Ratio	0.22

Table 3-5: Concrete Slab Properties

Material	Normal Weight Concrete
Young's Modulus	24.86 GPa
Poisson's Ratio	0.2
Compressive Strength	4000psi @28day

Table 3-6: Tempered Glass Properties (Tecnoglass 2014)

Material	Tempered Glass (Tecnoglass)
Young's Modulus	70 GPa
Poisson's Ratio	0.22
Compressive Strength	140,000psi
Bending Strength	29,900psi
Tensile Strength	17,000psi

Five different materials will be tested and compared for effective load distribution through the concrete slab. The intermediate material rests below the solar cells and sits atop the concrete slab with a total thickness of 38.5mm (~1.5in). Each of the five materials has varying moduli of elasticity ranging from 0.001Gpa, incredibly soft rubber, to 30Gpa, concrete. If concrete is used as the final material it will conclude that an intermediate material is not needed in the design. Below in Table 3-7 are the five intermediate materials. Note that each material’s modulus of elasticity is separated by roughly an order of magnitude of 10. This ensures a broad but complete analysis is conducted between possible material types.

Table 3-7: Intermediate Material Properties (Cambridge University Materials Data Book 2003)

Material	Modulus of Elasticity (Gpa)	Poisson's Ratio (υ)	Density (kg/m^3)
Concrete	30	0.18	1900
Hard Rubber	2.96	0.46	1100
Polyethylene	0.41	0.46	950
Silicon Elastomer	0.02	0.47	1500
Soft Rubber	0.001	0.5	950

CHAPTER 4

STRUCTURAL ANALYSIS OF BRIDGE DECK SLAB

In this chapter the geometry of the solar bridge slab will be used in order to demonstrate the effects a material's modulus of elasticity can have on the load transferring performance of a fully loaded walking surface. The geometry is comprised of concrete slabs housing an array of solar modules, as presented in Figures 4-2 and 4-3, with material properties found in Tables 3-4 through 3-7.

The structure's top layer is a plate of fully tempered Tecnoglass (E = 70 GPa, υ = 0.2) consisting of an outer fully compressive layer with an intermediate fully tensile core. The thickness (Tg) of the glass plate is 12mm- roughly ½" seen in Figure 4-1. Beneath the glass is the array of silicon solar cells (E = 165GPa, υ = 0.22) with thickness (Tc) of 0.3mm. An intermediate material of 1.5" is expressed as thickness (Tf). All materials will be modeled as isotropic linear elastic materials.

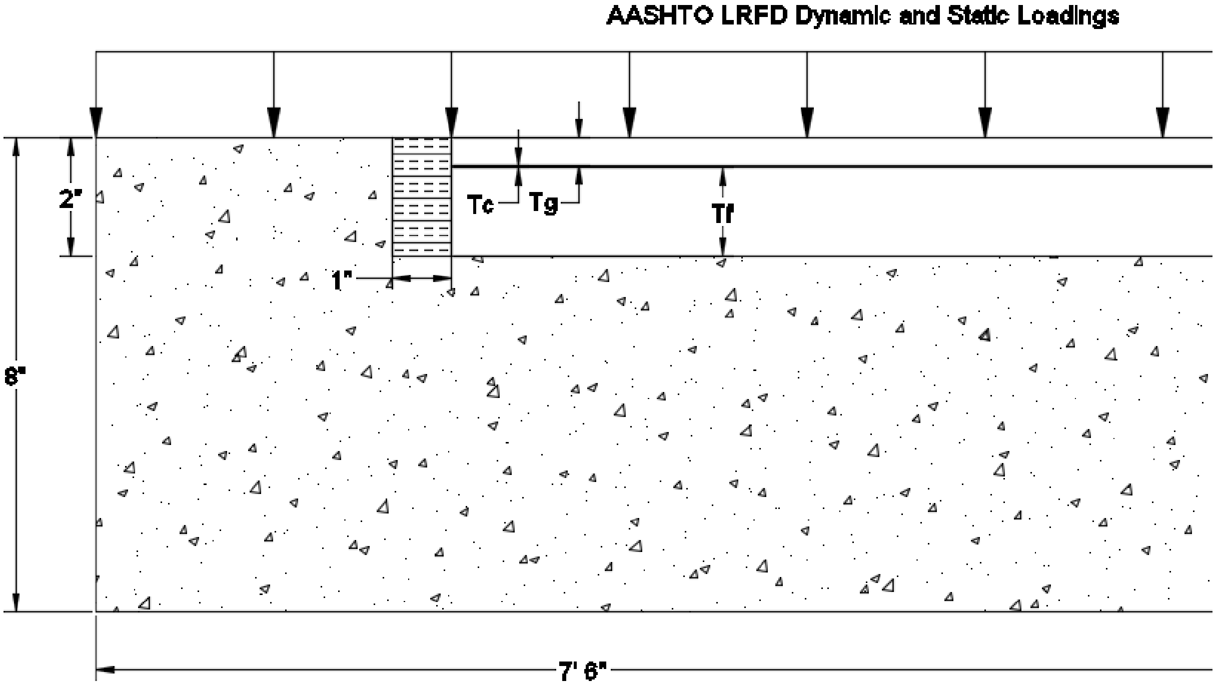

Figure 4-1: Cross Section of Slab Geometry

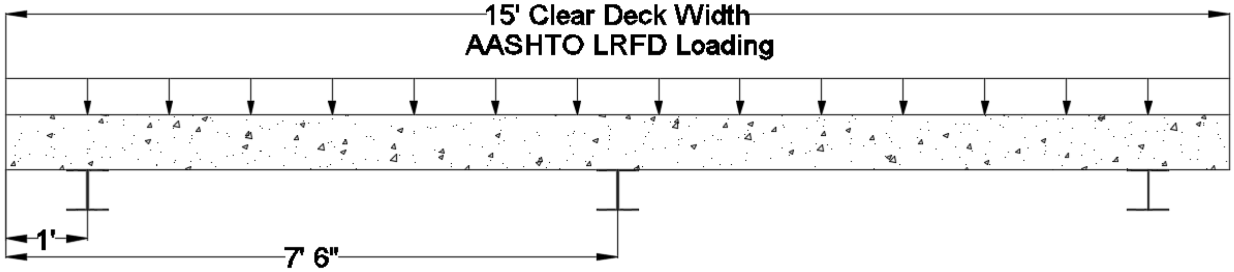

Figure 4-2: Full Deck Cross Section

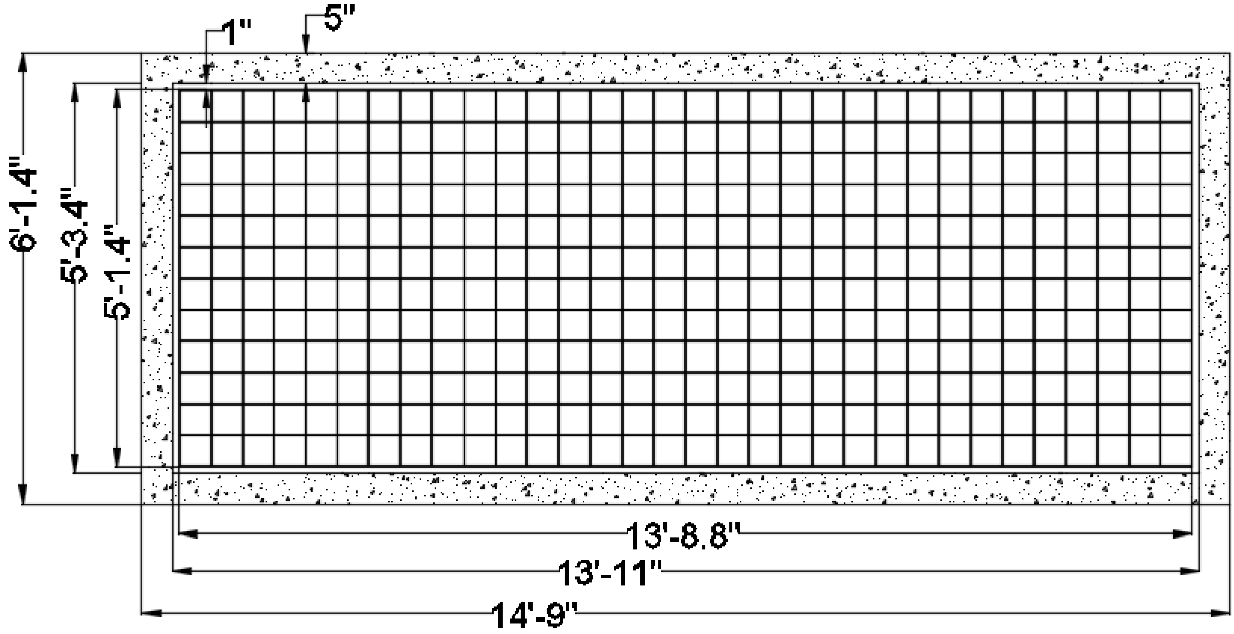

Figure 4-3: Fully Dimensioned Deck Panel

In ANSYS model a single panel seen in Figures 4-3 supported by 3 A36 steel I-beams (E = 200 GPa, υ = 0.26) spaced 1ft on center from the slab edges seen in Figure 4-2. Model the glass plate, monocrystalline silicon solar cells, varying intermediate material, concrete casing, and three supporting I-beams.

Model the 1.5in intermediate material between the solar array and concrete base with materials of varying moduli of elasticity. Range the material's modulus from a typical firm rubber, classically low E, to concrete, and determine if the solar module can simply rest upon the concrete base below or if an intermediate material is truly required. Compare maximum experimental values of all AASHTO LRFD loading parameters in Table 3-3 with maximum tensile and compressive material strengths. Analyze maximum deflections, stresses, and frequencies of the design slab under AASHTO LRFD static and dynamic pedestrian, equestrian and vehicle load parameters to determine the durability of proposed materials of the solar slab.

Use second order three dimensional solid elements in ADINA in order to provide a benchmark solution to which the other method is compared. Take specific note of the solar cell and glass stresses, as well as maximum deflection criteria of varying intermediate materials.

4.1 Deck Slab Finite Element Analysis (FEA)

When predicting stresses in tempered glass structures, there are two main options for stress predictions. The first possibility is to use formulas, tables or design charts. The other method consists of finite element analyses of the structure. The method of formulas has the advantage that it is easy to use, but its use is limited to basic geometries and boundary conditions. In this work, a basic rectangular geometry is studied; however, the boundary conditions are more complex then what design charts and tables can provide. For the case of a single glass deck slab, finite element analyses must be used to analyze stress and deformation patterns throughout the structure.

When making analyses using three dimensional solid elements, analysis results become sufficiently accurate given that the discretization of the model is fine enough. When analyzing the combined structures that are relevant in this work, finite element models become too large and the demand on computational resources too heavy.

4.2 General

In this thesis a single concrete deck slab is modeled in order to analyze the effects of AASHTO LRFD pedestrian bridge loading parameters against the internal solar cells and tempered glass surface material. The model is comprised of a tempered glass plate over tightly packed monocrystalline solar cells. Beneath the cells is an intermediate material separating the cells and concrete housing below. All materials were modeled as isotropic and linear elastic materials.

4.3 Description of Model

The model is comprised of 390 individual solids: tempered glass plate, 384 solar cells, intermediate layer, concrete slab, and steel stringers. The tempered glass is 4314mm x 1654mm with a thickness of 12mm. Please note for this thesis the glass was modeled 1in larger for both the length and width in place of the 1in expansion joints separating the glass and concrete. Each solar cell is 125mm x 125mm and 0.3mm thick. While not specific to any particular solar module, these dimensions are within standard range of a variety of cells on the market today. There is 8mm of separation between each cell and 8mm between each exterior cell and concrete. The intermediate material beneath the cells is 4314mm x 1654mm, identical to the glass, with a thickness of 38.5mm. The outer dimensions of the concrete are 4572mm x 1912mm with a total thickness of 177.8mm. The inner molding is 4314mm x 1654mm and depresses down 50.8mm. This leaves a symmetric concrete edge, around the solar, glass, and intermediate materials, of 129mm.

In Tables 3-4 thru 3-6, the material parameter values are presented. E denotes modulus of elasticity and ν denotes Poisson’s ratio for silicon, concrete, and glass respectively. Standard A36 steel was used for bridge stringer geometries. Table 4-1 presents the varying intermediate material’s moduli of elasticity, Poisson’s ratio, and density.

Table 4-1 Intermediate Material Parameters (Cambridge University Materials Data Book 2003)

Material	**Modulus of Elasticity (Gpa)**	**Poisson's Ratio (υ)**	**Density (kg/m^3)**
Concrete	30	0.18	1900
Hard Rubber	2.96	0.46	1100
Polyethylene	0.41	0.46	950
Silicon Elastomer	0.02	0.47	1500
Soft Rubber	0.001	0.5	950

Meshing is an integral part of the computer-aided engineering simulation process. The mesh influences the accuracy, convergence and speed of the solution. Furthermore, the time it takes to create a mesh model is often a significant portion of the time it takes to get results from a FEM solution. Therefore, the better and more automated the meshing tools, the better the solution. Meshing techniques from ANSYS provide the flexibility to produce meshes that range in complexity from a pure hex mesh to highly detailed hybrid meshes.

The deck slab finite element model’s geometry is comprised of basic rectangular plates of varying thicknesses. Because of their box-like geometry, a desired pure hex mesh was used for the tempered glass, intermediate, and solar cells. This mesh method uses an unstructured meshing approach to generate a quad dominant surface mesh and then fills it with a hex dominant mesh. This approach gives hex elements on the boundary of a chunky part with a hybrid hex, prism, pyramid, or tetrahedral mesh internally.

Due to varying thicknesses, however, the number of elements that comprised each material thickness was different. The available memory and processing time of the entire model was controlled by each material's comprised number of elements per thickness. This is because as the number of elements per thickness increase, the number of elements of the model increases exponentially. Convergence tests were conducted on each geometry to conclude the optimal number of elements to comprise each geometry's thickness without enduring long processing times. While effective, it must be noted that a total model convergence analysis was not able to be conducted. Each of the 384 solar cells was meshed with a single element thickness, along with the steel stringers. Both the tempered glass and intermediate had a three element thickness. Due to the interest in the solar cells, a 1in element sizing was used for standard cells, while a refined element size of 0.2in was used for cells in the direct vicinity of load cases as shown in Figure 4-4 below.

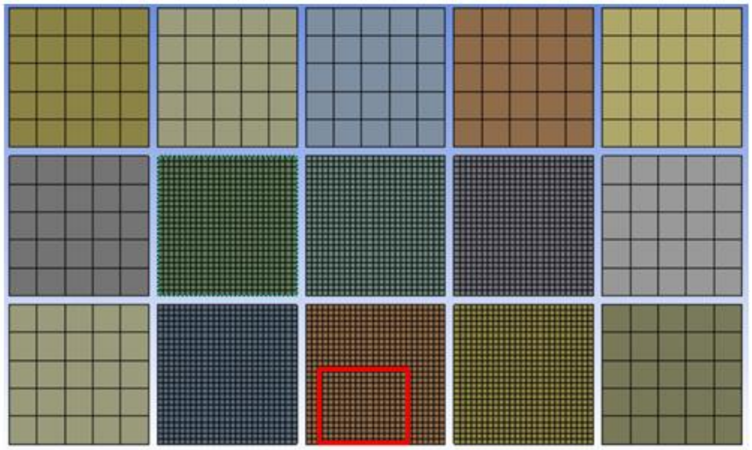

Figure 4-4: mesh refinement of local solar cells (red defines boundary of load case)

The varying color of the cells in Figure 4-4 are for visual orientation only. ANSYS 15.0 uses a random color generation system to help the user visually differ between identical geometries. For the sake of model discretization all solar cell geometries were meshed with a single element thickness of 0.3mm. The glass meshing was comprised of 2in sized elements, while the intermediate had 2in sized elements as well. The steel stringers were of little importance in the analysis, but needed to be comprised of fine enough meshing to allow for accurate load transfer through the whole system's geometry. Each steel stringer's length and width was divided into a number of sections to create their mesh sizing. The width was split into 6 divisions, and the length was split into 70 divisions.

The Concrete Slab was the only geometry meshed with triangular elements creating a tetrahedral mesh. For volume meshing in the system a tetrahedral mesh generally provides a more automatic solution with the ability to add mesh controls to improve the accuracy in critical regions. On the contrary, a hexahedral mesh, used for cells, glass, and intermediate, generally provides a more accurate solution, but is more difficult to generate. The total finite element model contains 236,906 nodes within 44,067 elements. Each element does not have the same number of nodes where the solar cells contain elements with 9 nodes, but concrete elements contain elements with various numbers of nodes based on their triangular meshing.

4.4 Loading Parameters

All required AASHTO LRFD pedestrian bridge load cases were analyzed under static loading. The pedestrian load case used a distributed load applied perpendicular to the entire tempered glass face. The pedestrian load had a magnitude of 90psf. For vehicle loading a front axle loading of 1.15kips was used with an axle length of 1397mm and individual tire tread areas of 4032.25mm^2. The tread was assumed based on a general assumption made for tire tread being total weight of the design vehicle divided by the pressure in each tire. Five locations were of interest under vehicular and equestrian analysis. Figure 4-5 shows each axle location in question and a number value to define the location. Figure 4-6 shows each hoof location in question with a number value to define the location. A loading of 1kip was applied over 16in^2 to satisfy the loading parameters of all equestrian cases while vehicular loading falls under a special loading case detailed in Section 3.1.4. All load cases were performed using pressure as the static structural load type.

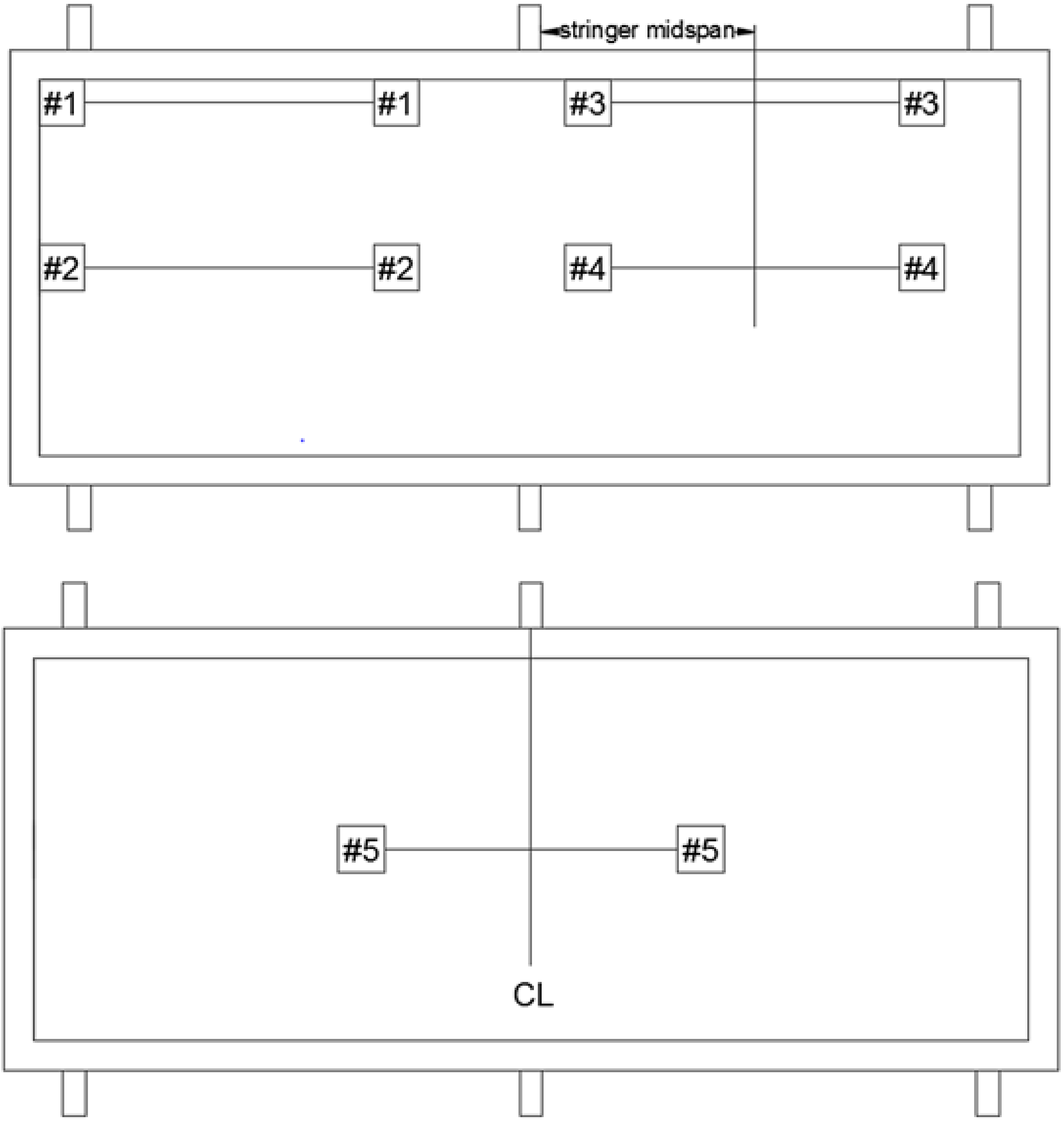

Figure 4-5: Vehicular Loading Locations

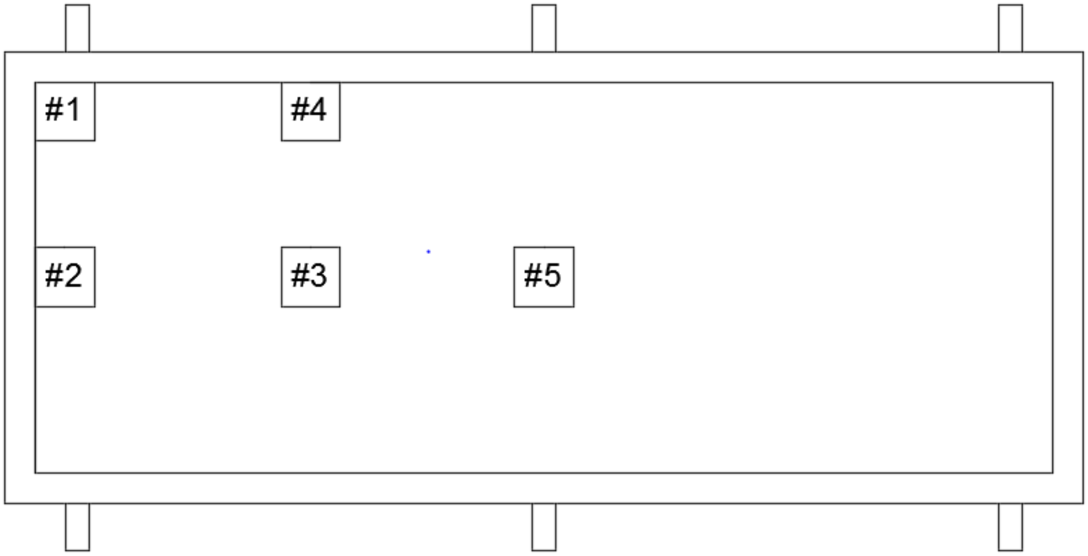

Figure 4-6: Equestrian Loading Locations

CHAPTER 5

FEA STRESS AND DEFLECION RESULTS

In this chapter stresses and deflections are presented and analyzed. Stress and deflection of the solar slab are important because external deformation caused by loading generates internal stress states that lead to plastic failure in some high stressed zones of each material. Plastic failure is the criterion used to determine the breakdown of each individual material. The failure stresses of the tempered glass and underlying solar cells due to bending and tension will be compared with maximum resulting stresses of each material under all static loading types and cases. Similarly the maximum deflection of the tempered glass and solar cells will also be analyzed under static loading. Lastly the first six mode shapes and resulting maximum frequencies will be presented.

5.1 Stress Results of Tempered Glass in FEA

All five loading locations in question were compared across changing moduli of elasticity. While the entire structure as a whole is important, the tempered glass, and solar cells below are of most importance and concern. Therefore the results presented here in will be of only the glass and cells. The concrete and intermediate materials are all well suited to withstand the forces acting upon the structure and ultimate failure lies in either the glass or cells. In Figure 5-1 the maximum recorded stress in the glass under pedestrian loading is shown as the intermediate materials modules of elasticity changes from 0.001 (soft rubber) to 30Gpa (concrete).

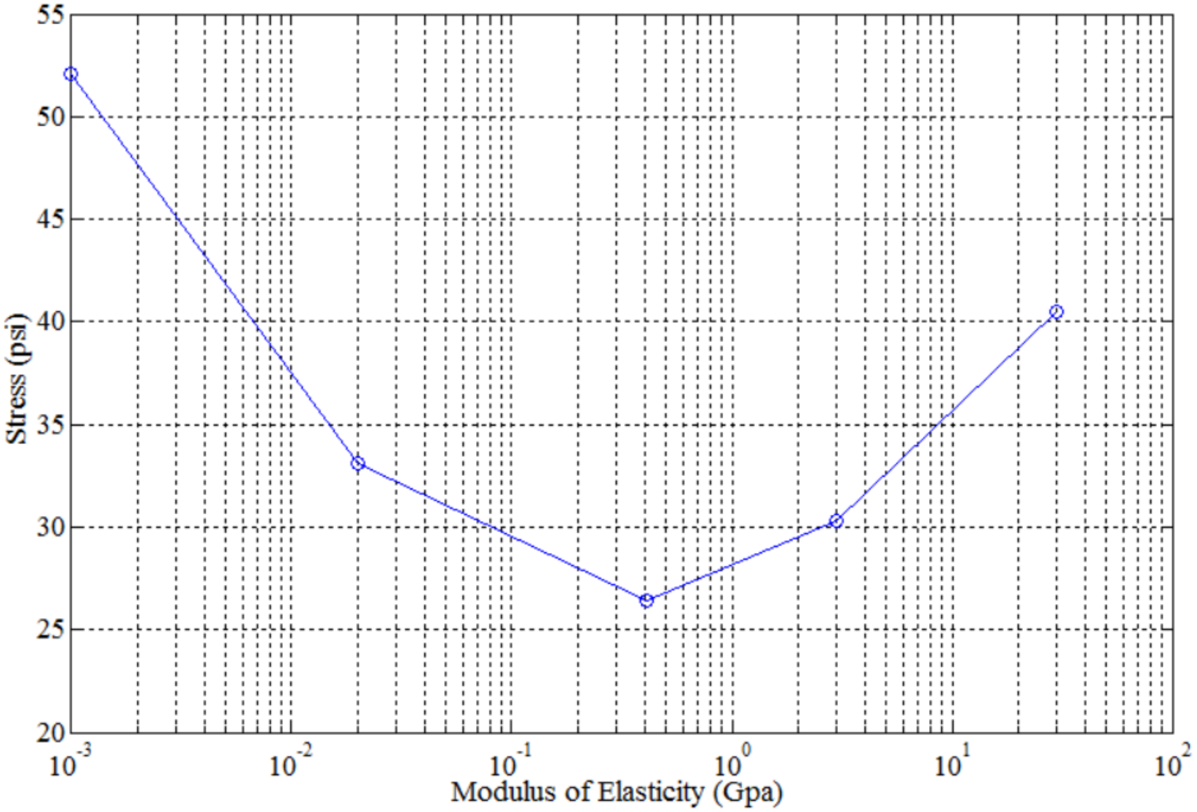

Figure 5-1: Max Stress in Tempered Glass under Pedestrian Loading

Under Pedestrian loading a trend appears as the modules of the intermediate material changes. Max stresses reduce by nearly half at 26.4psi as the modulus of the material approaches 1Gpa. After that point however, the max stress increases at the same rate as it initially declined, and returns to within roughly 15% of the original max stress of 52.1psi at 40.5psi when concrete properties are substituted as the intermediate material.

While the pedestrian load analysis suggests that an intermediate material with elasticity of roughly 1Gpa be used for lowest stress concentrations within the glass, under far heavier loadings, such as the equestrian and vehicle, there is a different pattern. Figures 5-2 and 5-3 show the max stresses within the tempered glass under equestrian loading and vehicular loading respectively. Both figures include all five scenario loading locations thought to induce the worst case stresses.

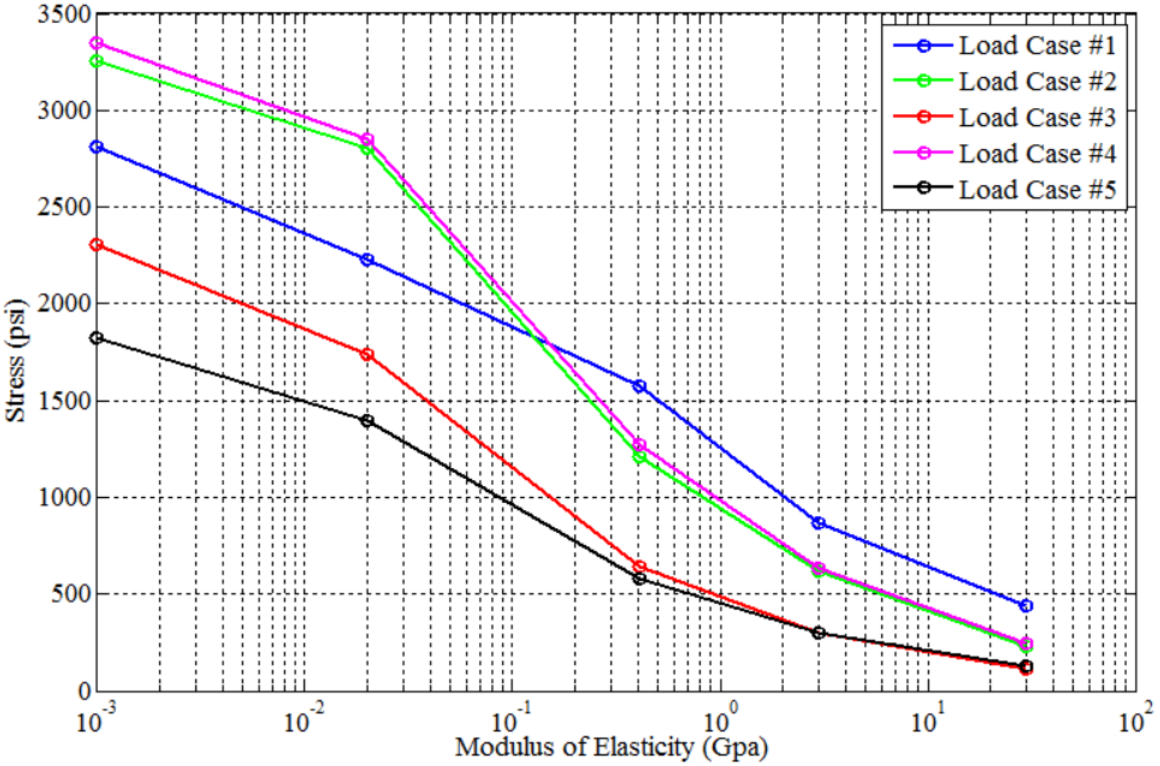

Figure 5-2: Max Stress in Glass under Equestrian Loading Cases

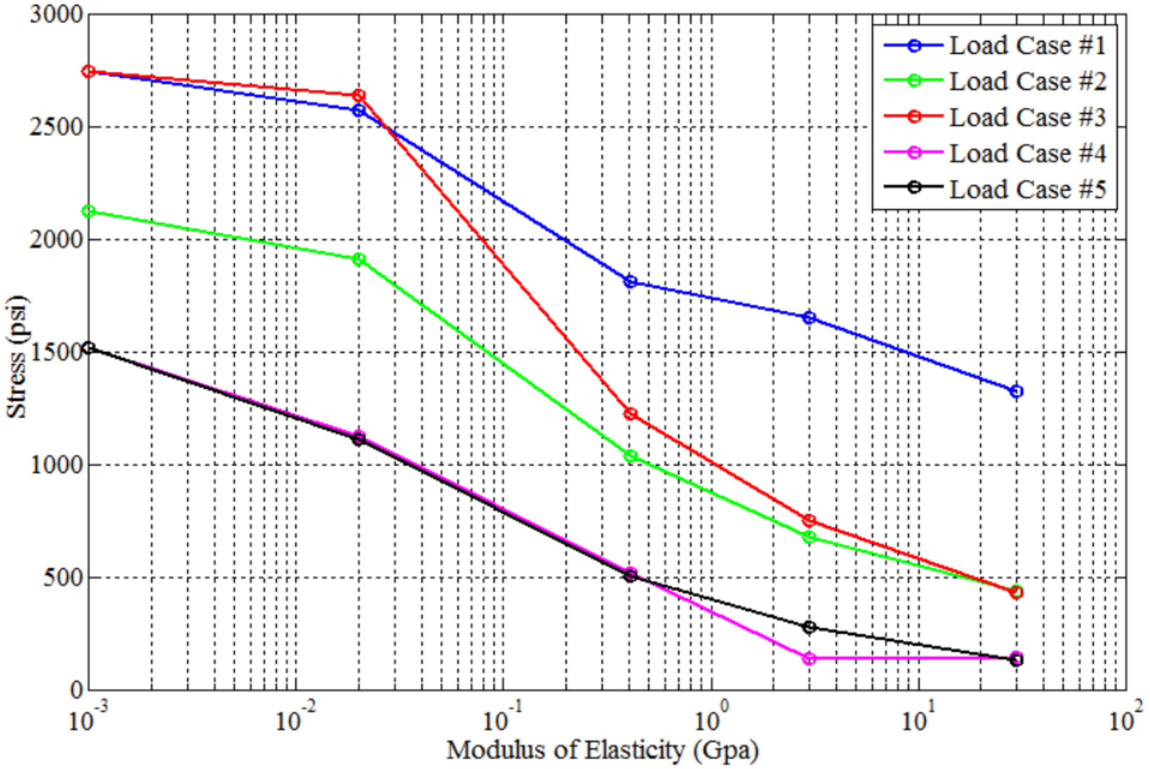

Figure 5-3: Max Stress in Glass under Vehicular Loading Cases

Under all vehicular and equestrian loading cases it is clear that as the modulus of elasticity of the intermediate material increase the stress within the tempered glass reduces considerably. The most dramatic cases being equestrian loadings at locations 2-5 where max stresses reduced by 93%, 95%, 92.5%, and 93.1% respectively. The overall maximum stresses induced by AASHTO LRFD pedestrian bridge loading parameters in the glass are shown in Table 5-1.

Table 5-1: Maximum Induced Stress in Tempered Glass

AASTO LRFD Loadings

Material	Load Type	Modulus of Elasticity (Gpa)	Poisson's Ratio (υ)	Max Stress (psi)
Soft Rubber	Pedestrian	0.001	0.5	52.1
Soft Rubber	Vehicular	0.001	0.5	2743
Soft Rubber	Equestrian	0.001	0.5	3352

From the results in Table 5-1 it is clear that the intermediate material should not be made of the analyzed soft rubber with a modulus of elasticity of 0.001Gpa. Each of the load cases produced maximum stresses within the glass with soft rubber as the intermediate material. Although even the largest resulting stresses are very low compared with the max allowable stress of the glass. The lowest resulting stresses in the glass result from a modulus of elasticity equal to that of concrete of 30Gpa, concluding that the glass can simply rest upon the underlying concrete slab. Furthermore the FEA has suggested that the glass thickness should be reduced from the original 12mm thickness. With a thinner glass stress patterns would remain relatively constant in the static analysis, but under transient dynamic load analysis special care would need to take place to ensure fracturing of the glass does not occur.

Table 5-2: Maximum Stress in Glass using Concrete Intermediate

Concrete Intermediate Material		
Load Case	**Applied Load Location**	**Max Stress (psi)**
Pedestrian	Distributed	40.5
Equestrian	#1	441.9
	#2	227
	#3	112
	#4	244.7
	#5	125.4
Vehicular	#1	1323
	#2	440
	#3	433
	#4	145
	#5	127
	Max Stress =	1323psi

Table 5-2 shows the total maximum stresses within the tempered glass generated by the corresponding load cases. The maximum resulting stresses occur in the glass under vehicular load case #1 with a concrete intermediate. The resulting stress is 1323psi and the max stress location is shown in Figure 5-4.

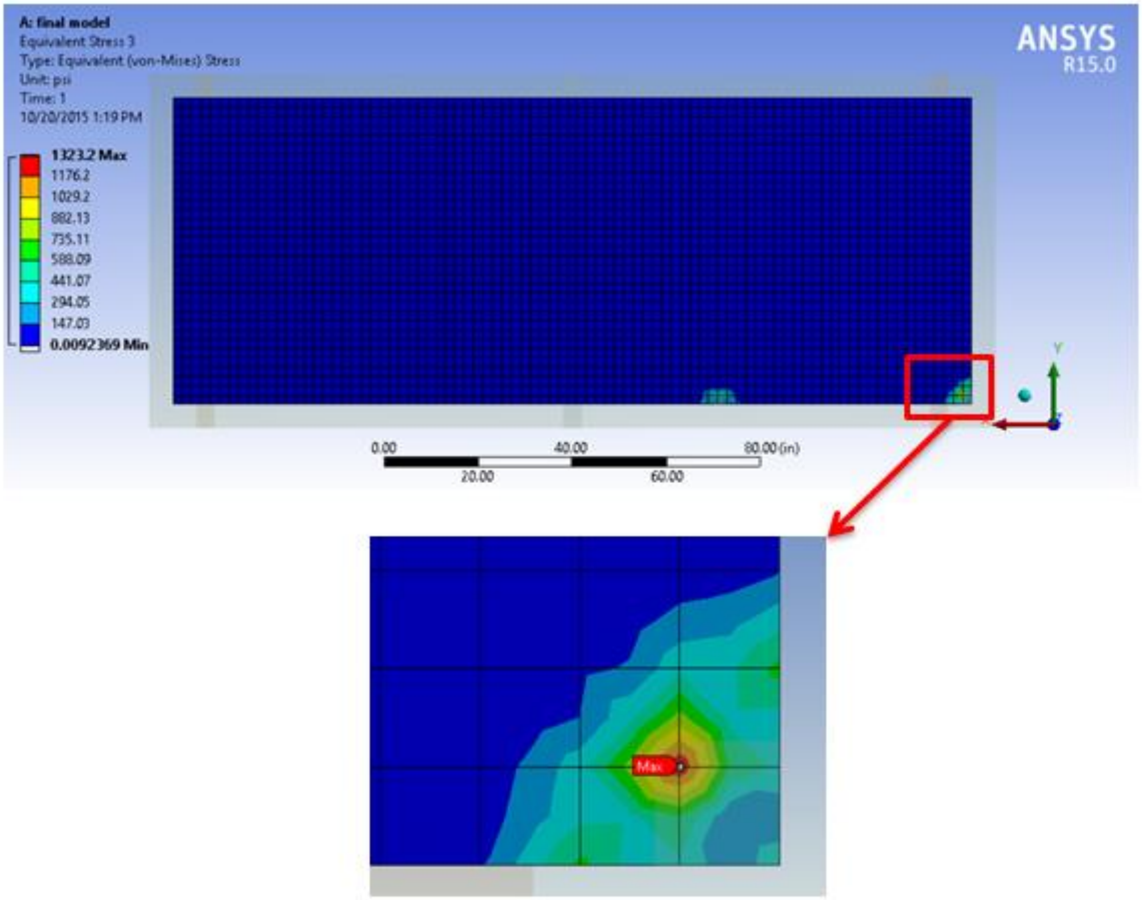

Figure 5-4: FEA Glass Maximum Stress Location

Due to the vehicle load case at location #1 a maximum stress occurs at the corner of the tempered glass. The loaded tread area was positioned so that all area was atop the glass. During this analysis there was no tread in contact with the concrete slab.

5.2 Glass Fracture Analysis

Techno glass states it produces a tempered glass with a tensile strength between 1,000 and 1,200Kg/cm^2 (14,250-17,000psi), and a breakage module between 350 and 550Kg/cm^2 (5,000-7800psi) in bending. The maximum stress induced from all AASHTO LRFD pedestrian load cases is 1323psi according to the results of the FEA. Therefore it is concluded that the 4314mm x 1654mm 12mm thick, tempered techno glass will not fracture under AASHTO LRFD loading parameters for pedestrian bridges, with a modified vehicular loading specific to the case of the pedestrian bridge at the university of Massachusetts Amherst. The slab is designed to be used in the elastic region, where the stress is sufficiently below the local yield stress. This prevents any local permanent deformation of the system and unwanted redistribution of critical stresses within the glass or other materials of the slab.

5.3 Deflection Analysis of Tempered Glass in FEA

While stress determines the failure location of a system, the importance of deflection in a system is a case to case affair. While static analysis has been a large focus for this thesis, the slabs will undergo repeated foot traffic and therefore the slab can be treated as a dynamic system. In cases of dynamic systems, too much deflection can lead to waring of the slab over time known as fatigue. The critical deflection of the glass determines what kind of cyclic stresses the glass undergoes for fatigue considerations. Therefore the analysis of the maximum deflection of each system material is of high importance. Figure 5-5 shows a sketch of the material layering of the proposed solar deck slab.

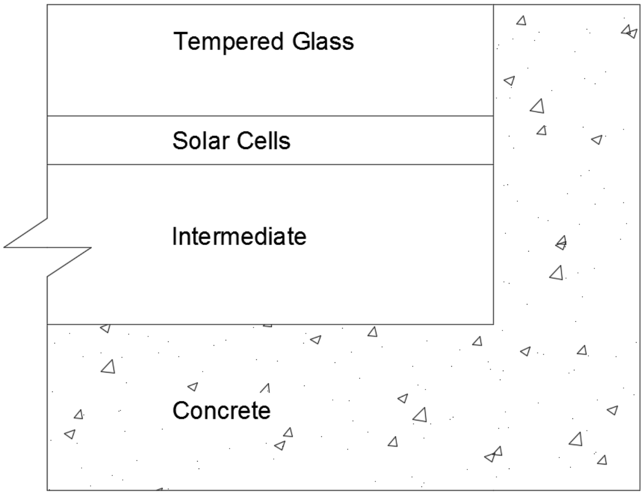

Figure 5-5: Slab Cross Section (not to scale)

The solar cells and glass maximum deflections are of extreme interest in this thesis. Large amounts of deflection can cause fracturing in each material's individual geometry internally before total failure of the slabs concrete shell. Figures 5-6 and 5-7 show the max deflection within the tempered glass under equestrian loading and vehicular loading respectively. All observed deflections for all load types and cases are very small and are allowable for the intended use of the slab.

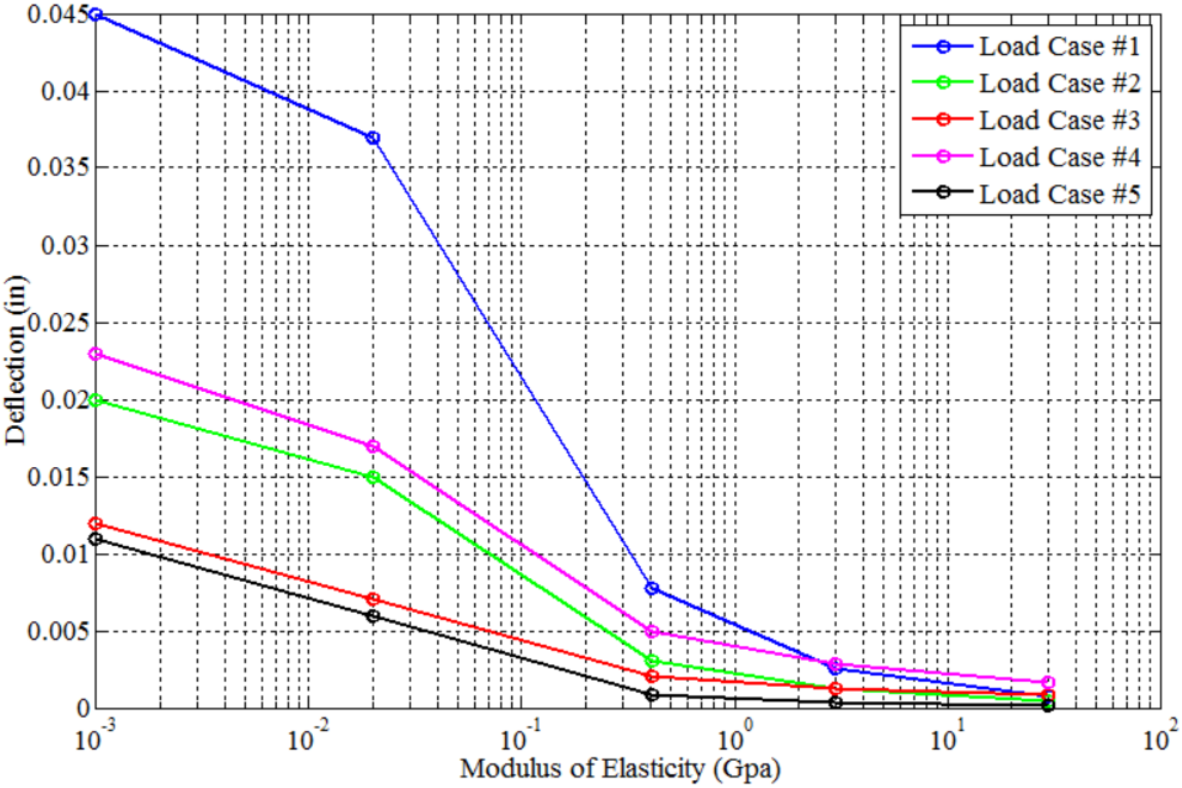

Figure 5-6: Max Deflection of Tempered Glass under Equestrian Loading

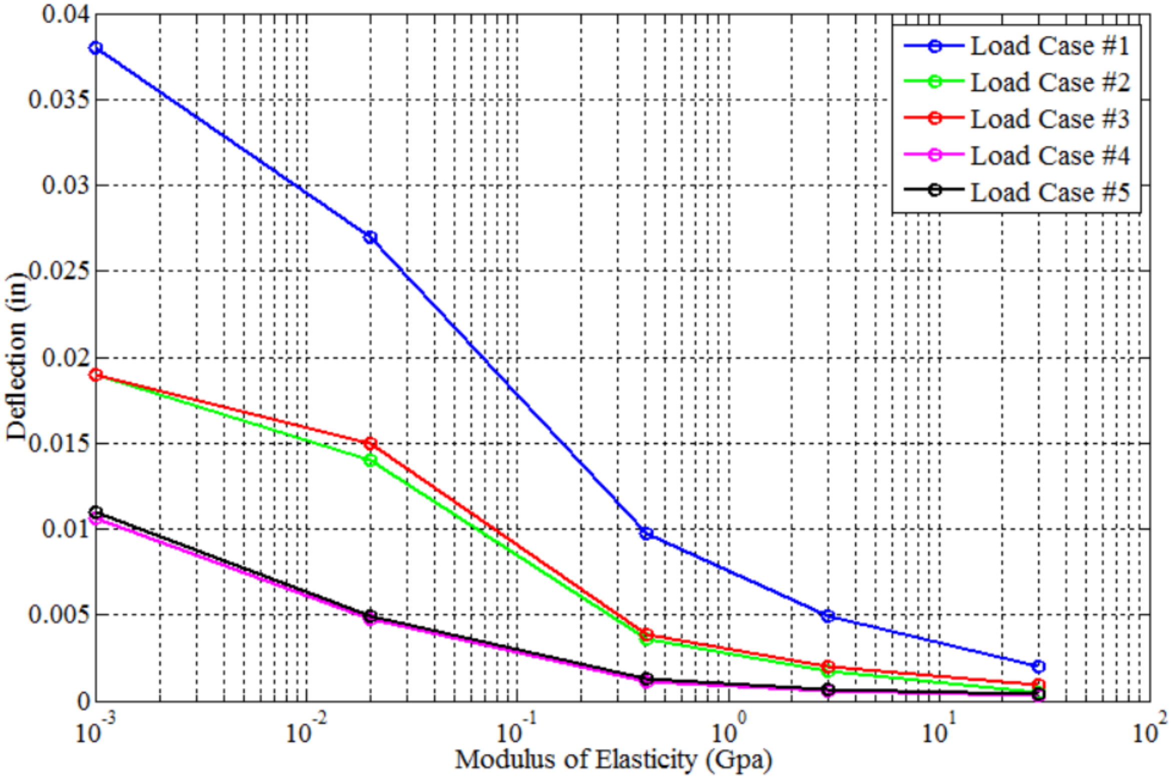

Figure 5-7: Max Deflection of Tempered Glass under Vehicular Loading

Under all vehicular and equestrian loading cases it is clear that as the modulus of elasticity of the intermediate materials increase, the maximum occurring deflection within the tempered glass reduces considerably. The most dramatic case is equestrian loading at location #1 where the max deflection was reduced by 98% from 0.045in to 0.0008in. Similarly, the overall maximum deflection for vehicular loading was reduced by nearly 95% from 0.038in to 0.002in when the materials modulus of elasticity increases to 30Gpa. Each maximum deflection occurred when a load was placed directly atop the corner of the glass slab, in both #1 load case locations when the modulus of elasticity for both cases was 0.001 (soft rubber). Deflection as well as stress analyses have both concluded with identical trends that as the modulus of elasticity increase to that of concrete, the overall stresses and deflections within the glass are at their lowest.

Further analyses were conducted to conclude whether the glass, while under loading, bends to create maximum deflections or if the interior layering system as a whole deflects downward and resulting deflections are caused by the entire downward movement of the glass. Figure 5-8 shows deflections of the tempered glass across several locations of its geometry.

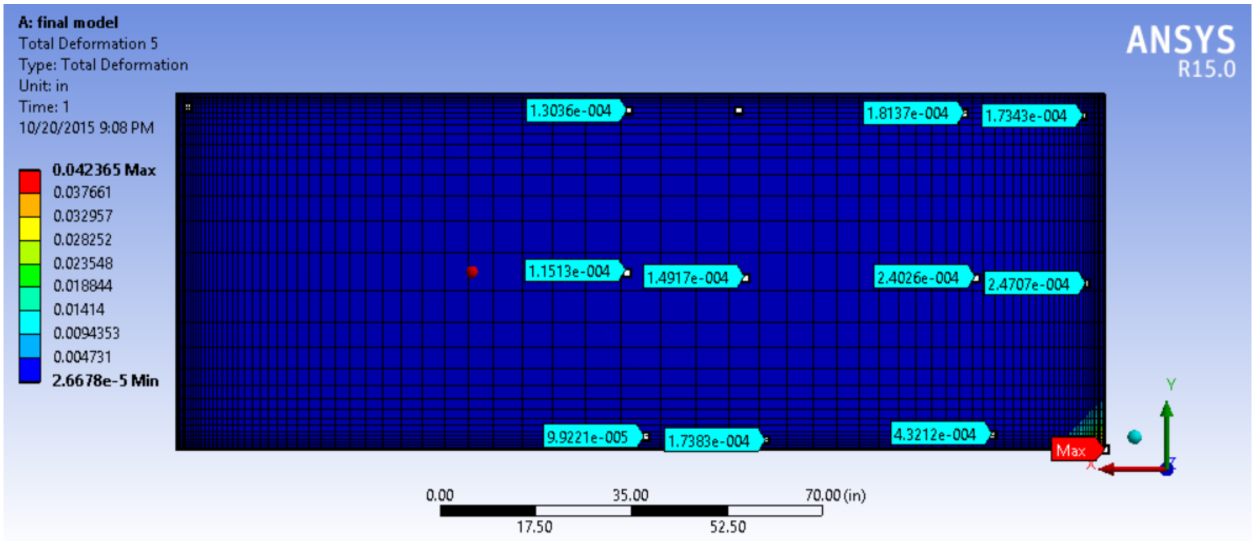

Figure 5-8: Flexural Bending Deflection

Table 5-3: Probe Deflections

Deflection (in)
0.042
2.40E-04
1.73E-04
1.81E-04
2.40E-04
4.32E-04
1.74E-04
1.49E-04
9.90E-05
1.15E-04
1.30E-04

Table 5-3 shows the several probe values shown in Figure 5-8. The resulting values of Table 5-3 conclude that the maximum deflection of the tempered glass occurs at the bottom right corner where the equestrian load was applied. Furthermore, the probe values show that the resulting deflection does not result from a total depression in the glass, but rather bending induced by the applied loading. The bending is a result of the cantilever effect of the glass out over the steel stringer supporting the entire slab. Figure 5-9 shows an exaggerated slab deflection criterion under equestrian loading #3.

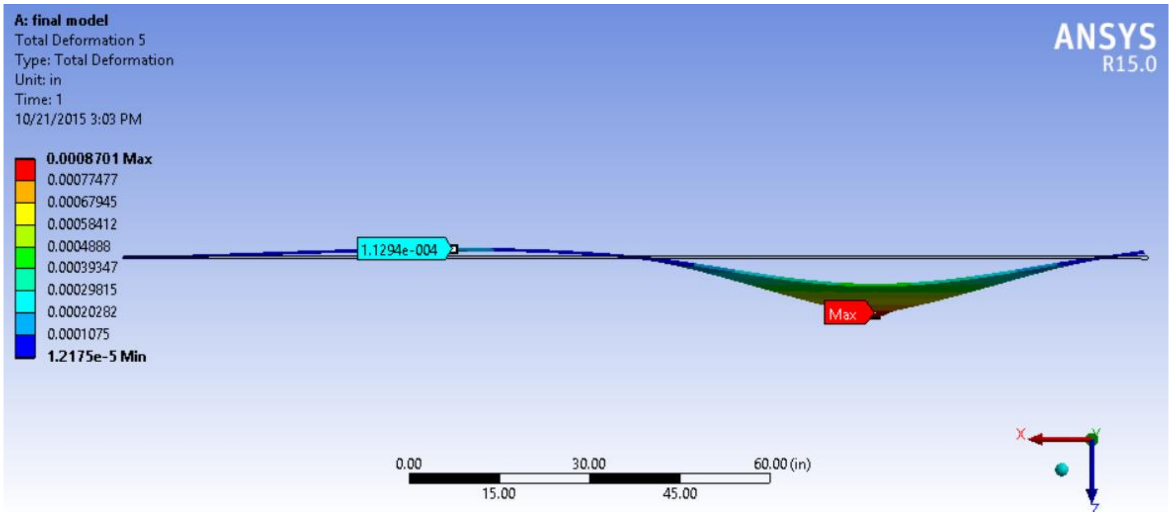

Figure 5-9: Tempered Glass Deflection under Equestrian load case #3 (1.1E+004 scale)

Note the deflection and bending of the slab under the loading. There is not a uniform downward deflection of the glass, but rather a bending of the glass over the supporting steel stringers below. The maximum deflection of equestrian load case #3 occurs at the mid-span of the center and right stringers of 0.00087in in the positive Z direction, while at the opposing stringer mid-span another notable deflection of 1.13E-004in occurs. While not influential, the direction of the deflection in the negative Z direction is notable. This along with all other loading scenarios has shown a bending of the glass rather than a downward displacement.

Deflection analysis of the tempered glass with varying intermediate materials in Figures 5-6 and 5-7 have further confirmed that the intermediate material should be removed from the slab, allowing the cells and glass to rest solely on the concrete slab below. Minimum deflections occurred when the modulus of elasticity of the intermediate material was 30Gpa, that of concrete.

Table 5-4: Maximum Deflection of glass using Concrete Intermediate

Concrete Intermediate Material		
Load Case	**Applied Load Location**	**Max Deflection (in)**
Pedestrian	Distributed	0.00083
Equestrian	#1	0.0008
	#2	0.00043
	#3	0.00087
	#4	0.0017
	#5	0.00011
Vehicular	#1	0.002
	#2	0.00046
	#3	0.00092
	#4	0.0003
	#5	0.00039
	Max Deflection =	0.002in

Table 5-4 shows the maximum deflection of the tempered glass generated by the corresponding load cases with a concrete as the intermediate material. The maximum resulting deflection occurred in the glass under vehicular load case #1. The resulting deflection is 0.002in and the max deflection location is shown in Figure 5-10.

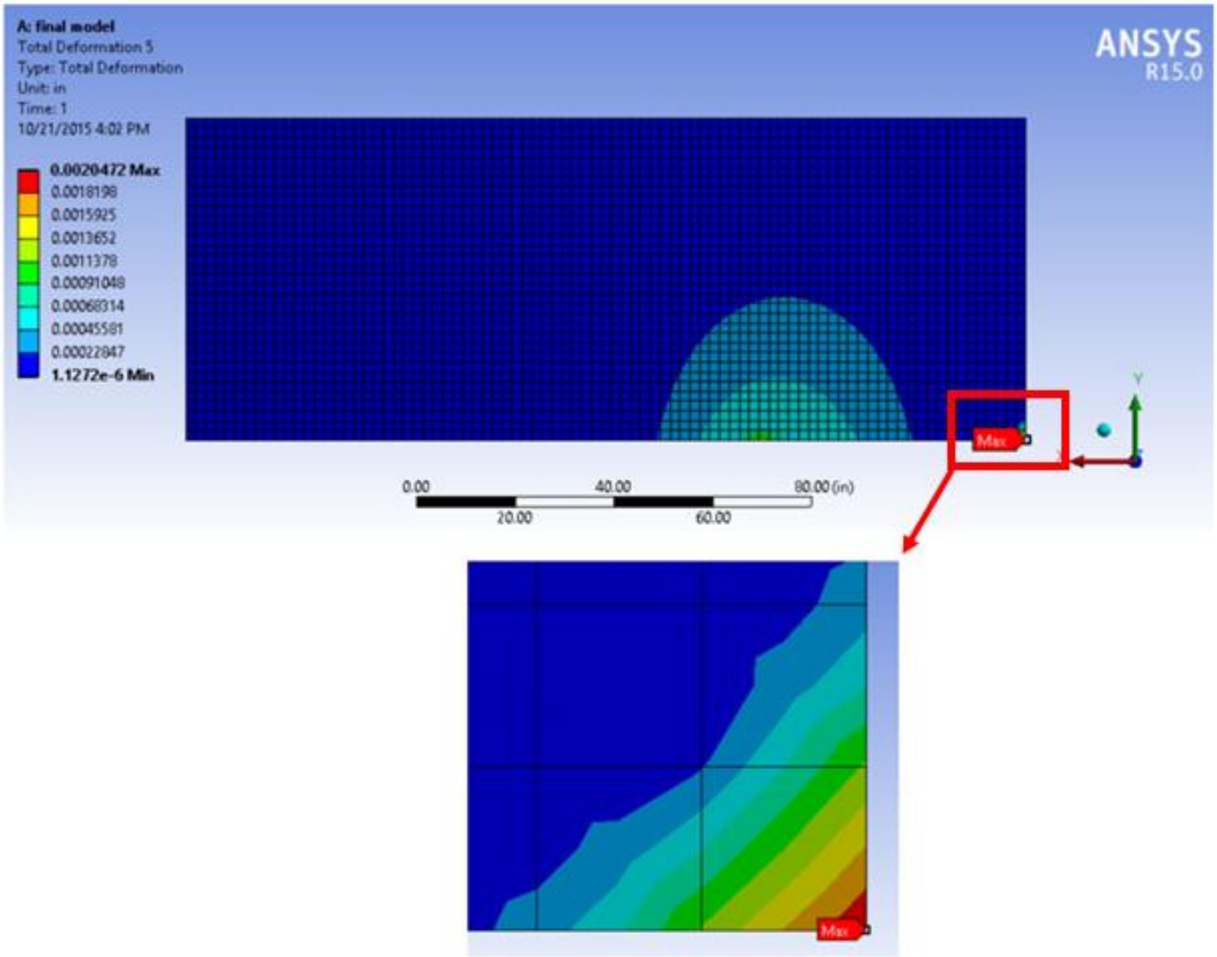

Figure 5-10: Glass Maximum Deflection Location

Let it be known that vehicle load case #1 gave the largest resulting stress within the glass as well as the largest deflection. It is concluded that the resulting deflection was due to plate bending, causing the large concentrated stresses within the glass.

5.4 Stress Results of Solar Cells in FEA

All five loading locations for both load types were compared across changing moduli of elasticity of the intermediate. While the entire structure as a whole is important, the tempered glass, and solar cells below are of most importance and concern. Ultimate failure of the system, as a whole, lies in either the glass or cells. Sections 5.1 through 5.3 have investigated the capabilities of the glass, and now that same investigation is presented here in of the solar cells. In Figure 5-11 the maximum recorded stress in the solar cells under pedestrian loading is shown as the intermediate materials modules of elasticity changes from 0.001Gpa (soft rubber) to 30Gpa (concrete).

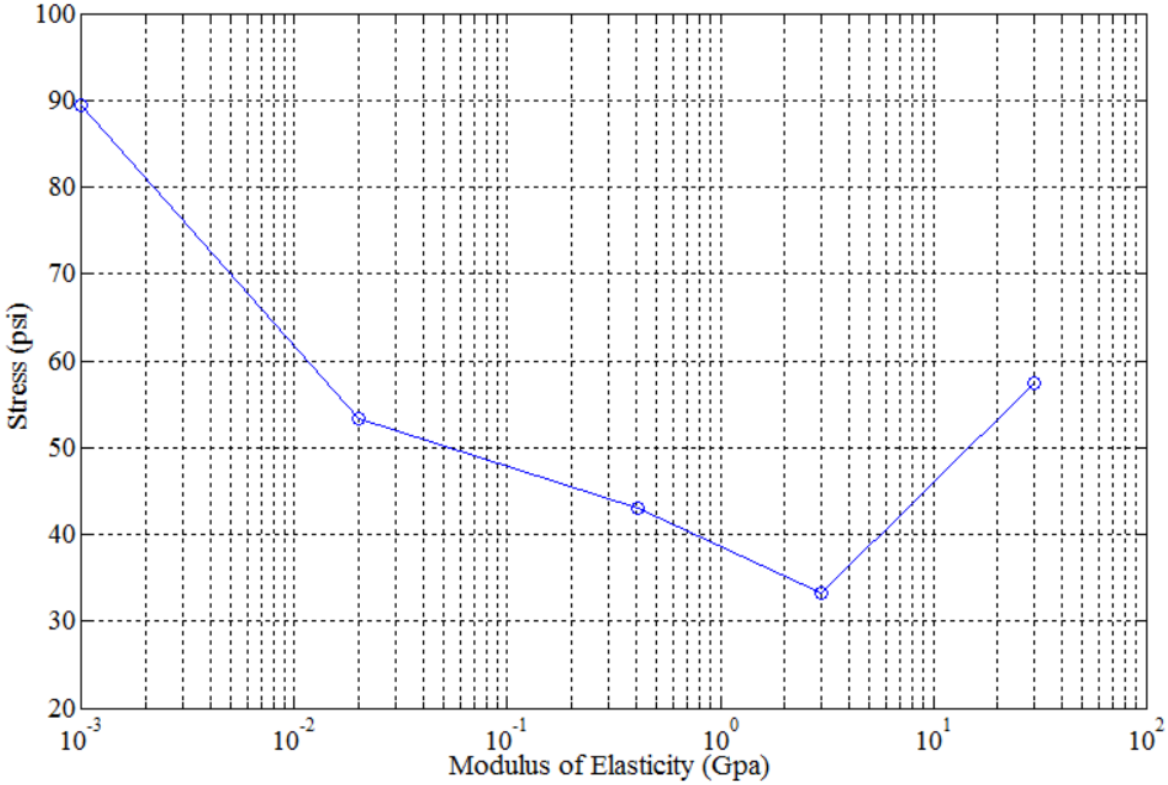

Figure 5-11: Solar Cell Max Stress under Pedestrian Loading

Figure 5-11 follows the same pattern in maximum stress as the moduli of elasticity increase in the intermediate material under pedestrian loading for the tempered glass. While the pattern remains the same, the overall stress within the cells is larger. Under pedestrian loading, the solar cells beneath the tempered glass experience max stresses that are double what the glass experiences. With weaker tensile and bending material properties and higher stresses, the solar cells will be the controlling failure location within the system. While any failure of a system in general is never wanted, the solar cells are the most crucial component to this entire thesis. They are what convert solar irradiance into electricity and their lifetime protection is the main engineering objective.

While the pedestrian load analysis for both the tempered glass and solar cells suggests that an intermediate material with elasticity of roughly 1Gpa be used for lowest stress concentrations within the glass, under equestrian and vehicle loadings, there is a different pattern, and due to the controlling nature of the load types, the use of a material with 1Gpa will be ignored. Figures 5-12 and 5-13 show the max stresses within the solar cells under equestrian loading and vehicular loading respectively. Both figures include all five scenario loading locations thought to induce the worst case stresses as shown in Figures 4-5 and 4-6.

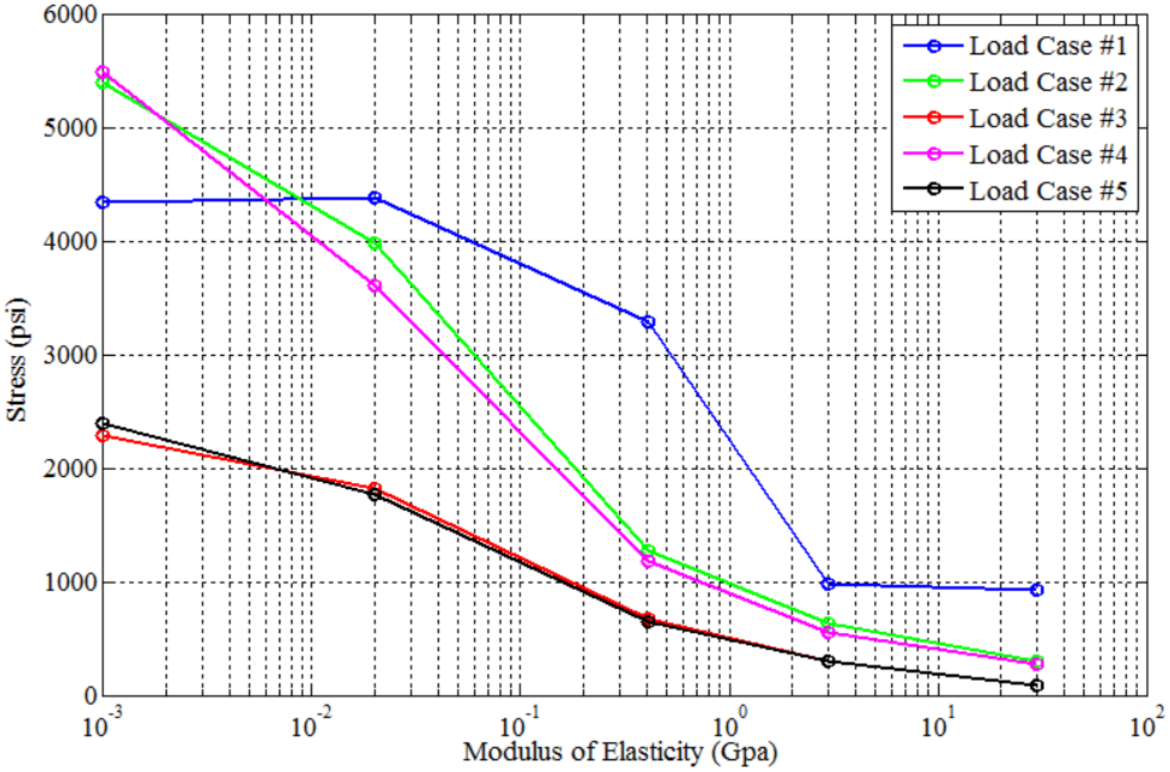

Figure 5-12: Max Stress in Cells under Equestrian Loading Cases

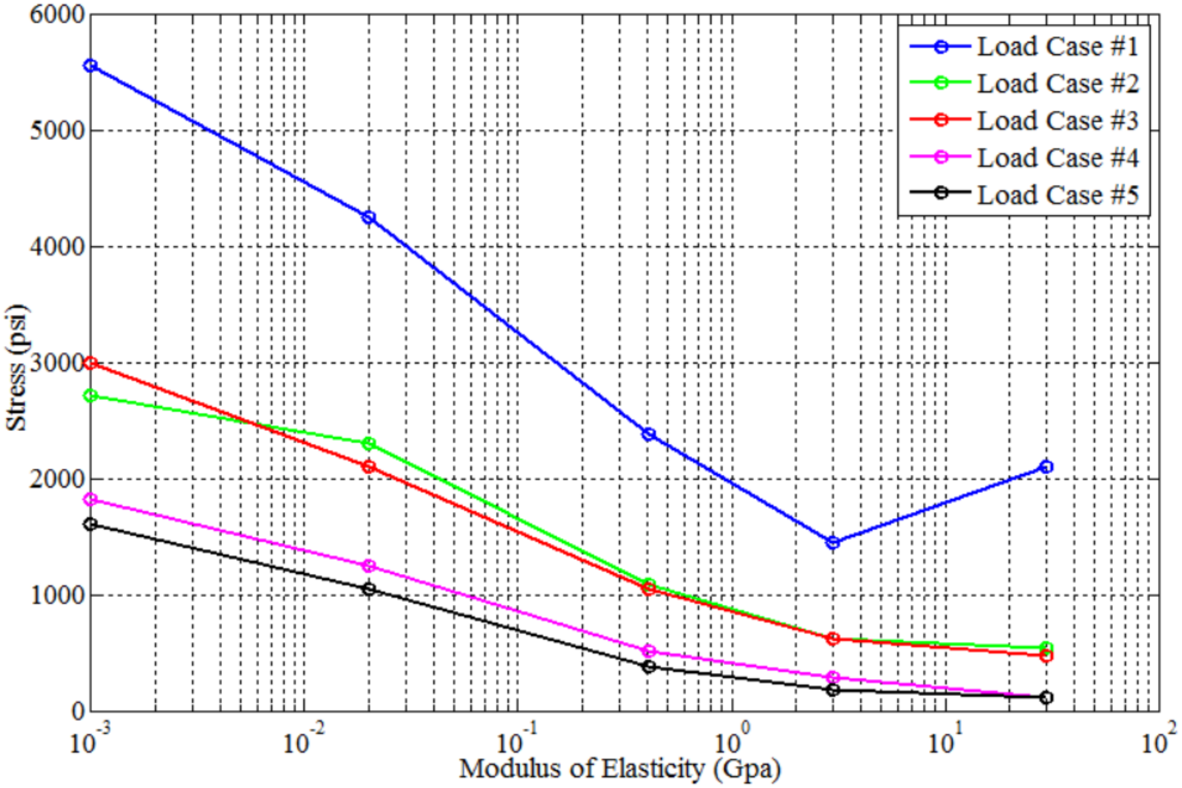

Figure 5-13: Max Stress in Cells under Vehicular Loading Cases

Under all vehicular and equestrian loading cases it is clear that as the modulus of elasticity of the intermediate material increase the stress within the solar cells reduces considerably just as the glass does. In fact, all materials of the system trend in this way. This is due to the contact criteria of the finite element model. All geometry’s contact surfaces are bonded and act as one system under loading. The results from Figures 5-12 and 5-13 corresponded to that. The max stresses in the cells under all load cases reduced between 60% and 95%. The overall maximum stresses induced by AASHTO LRFD pedestrian bridge loading parameters in the cells occur when the modulus of elasticity of the intermediate is significantly low. The conclusion that the intermediate material can be removed from the system is confirmed by both the tempered glass and solar cell stress analyses. All analysis of the solar cells here in will be with an intermediate material equal to that of concrete, (E = 30Gpa). It should be discussed however that these results were produced with a FEM that created a concrete slab with perfect surfaces. In the real world the precast concrete slab may contain imperfections along its surface where it contacts the underlying solar cells. Without the presence of an intermediate it is highly likely that fracture of individual solar cells will occur due to raised and uneven imperfections on the concrete.

Table 5-5: Maximum Stress in Cells using Concrete Intermediate

Concrete Intermediate Material		
Load Case	**Applied Load Location**	**Max Stress (psi)**
Pedestrian	Distributed	57.4
Equestrian	#1	922.3
	#2	305.4
	#3	86.2
	#4	271
	#5	91.4
Vehicular	#1	2099
	#2	545
	#3	473.5
	#4	108.3
	#5	108
	Max Stress =	2099psi

Table 5-5 shows the total maximum stresses within the solar cells generated by the corresponding load cases. The maximum resulting stresses occur in the cells under vehicular load case #1 with a concrete intermediate. The resulting stress is 2099psi and the max stress location is shown in Figure 5-14.

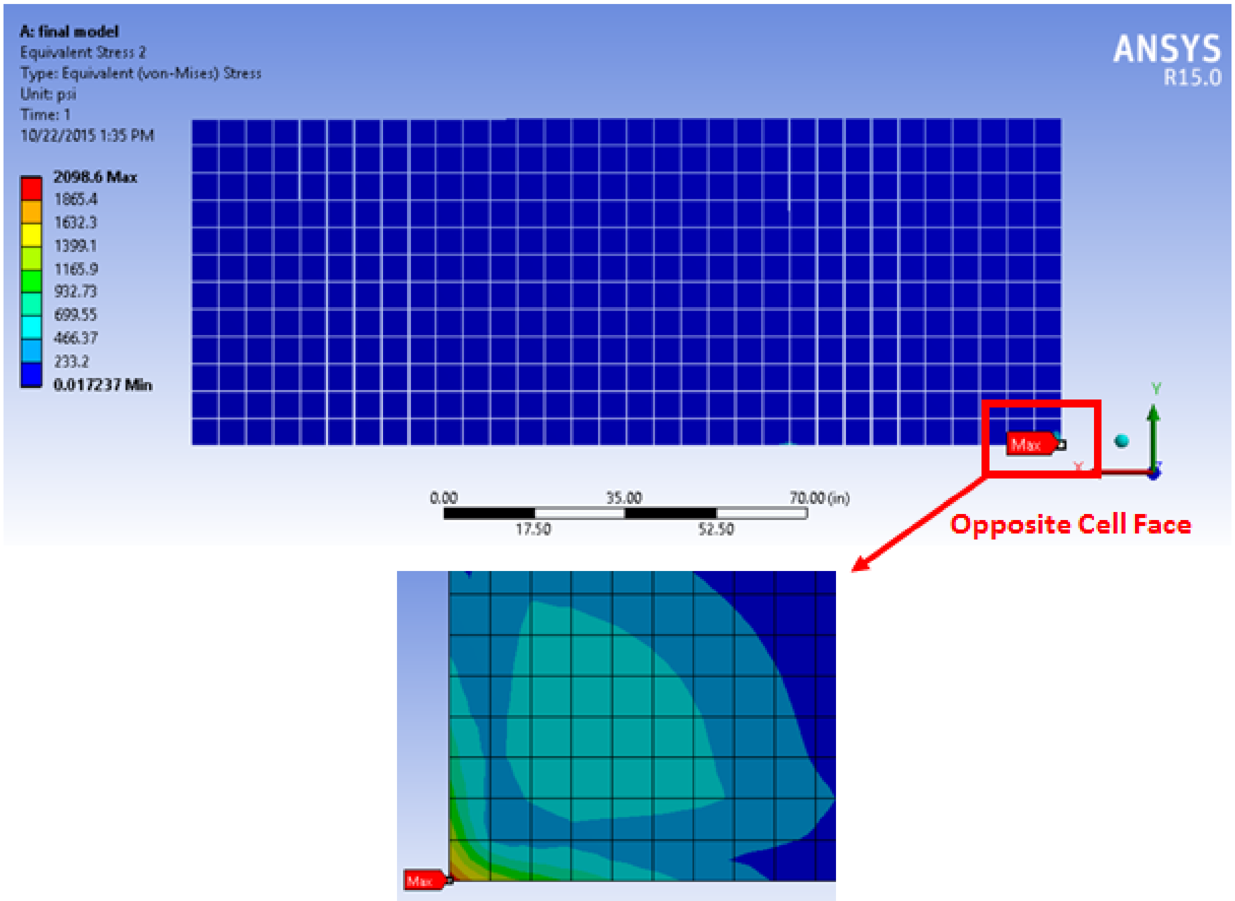

Figure 5-14: FEA Cell Maximum Stress Location

Due to the vehicle load case #1 a maximum stress occurs at the corner of the solar cells. The loaded tread area was positioned so that all area was atop the tempered glass. There is an offset of 8mm in both the X and Y directions before the cells begin, meaning that the loading is not oriented perfectly with the corner edge of the first solar cell. Only a single cell experienced large stresses from the load case. This small dispersion of stress among the cells is due to the high modulus of elasticity of the intermediate below.

5.5 Solar Cell Fracture Analysis

Martin Sander conducted an investigation of cracking patterns in encapsulated solar cells after mechanical loading to determine the ultimate strength of solar cells in solar modules. It was concluded that the mono-crystalline cells have average failure strengths of 96.4Mpa (~14,000psi) with a standard deviation of 6,700psi in bending. The standard deviation is noted as being quite large (Sander 2012). This error band is most likely due to the effect of micro-defects in the silicon wafers during the manufacturing stage. Because of these defects, some samples are weaker than others. All samples can be observed in Figure 5-15 with values presented in Table 5-6.

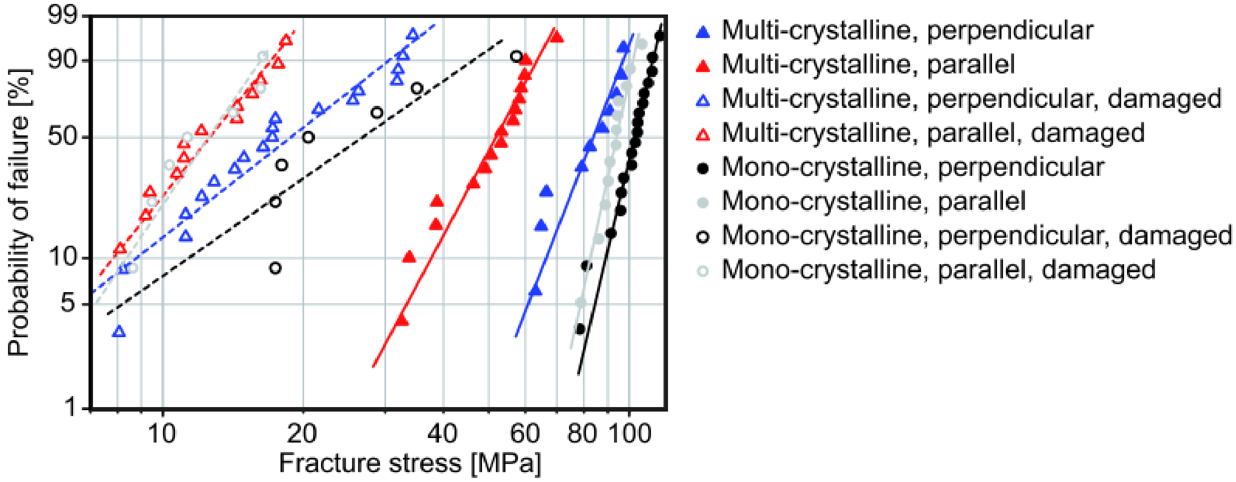

Figure 5-15: Weibull plot of crack occurrences in test specimens with mono and multi crystalline cells

Table 5-6: Investigated Weibull distribution values according to Figure 5-15, (values of 95% confidence intervals in brackets)

	σ_θ MPa	m -
Multi-crystalline, parallel	55.2 (50.1...60.4)	5.9 (3.8...8.4)
Multi-crystalline, perpendicular	87.6 (79.7...95.5)	8.1 (4.6...13.1)
Multi-crystalline, parallel, damaged	13.8 (11.8...16.0)	4.0 (2.5...5.8)
Multi-crystalline, perpendicular, damaged	21.8 (17.7...26.5)	2.5 (1.7...3.4)
Mono-crystalline, parallel	96.4 (92.2...100.6)	14.7 (9.1...21.3)
Mono-crystalline, perpendicular	105.7 (101.6...109.7)	13.3 (8.8...18.7)
Mono-crystalline, parallel, damaged	13.6 (11.1...16.4)	4.7 (2.4...7.9)
Mono-crystalline, perpendicular, damaged	30.3 (21.5...41.7)	2.3 (1.4...3.5)

The maximum stress induced from all AASHTO LRFD pedestrian load cases in the cells is 2099psi according to the results of this thesis' finite element model. It is concluded that all 125mm x 125mm x 0.3mm solar cells will not fracture under AASHTO LRFD loading parameters for pedestrian bridges, with a modified vehicular loading specific to the case of the pedestrian bridge at the University of Massachusetts Amherst.

In addition to the effect of flaws, there are other issues that should be considered before a design value of strength can be determined. Temperature dependence, fatigue and loading rate, sample size, sample orientation in relation to crystal plane orientation, and orientation of conductor strips in relation to bend direction all must be more closely analyzed for every sample of silicon solar cells used (Sander 2013). The failure strengths used in comparison above were conducted in a lab under ideal conditions, and because of the brittle nature of silicon all of the parameters stated above can reduce the safe value of design strength from the theoretical value, as discussed by Sander. Sander has shown that cell orientation and composition changes the fracture stresses of a cell by almost half in comparison with multi and mono crystalline cells in parallel. It is therefore not prudent to use a design value based simply on theoretical results.

5.6 Deflection Analysis of Solar Cells in FEA

Solar cells are made out of silicon, like glass. Therefore they are like glass, and quite hard. Unlike glass, solar cells are crystalline, rather than amorphous. This means that they are more brittle and also have an orientation, whereas glass is non-directional. They'll tend to break “along the grain” so if the orientation of the cells grain are in the same bending direction of the slab, they'll be less likely to break. Figures 5-16 and 5-17 show the max deflection of the solar cells under all equestrian and vehicular load cases respectively.

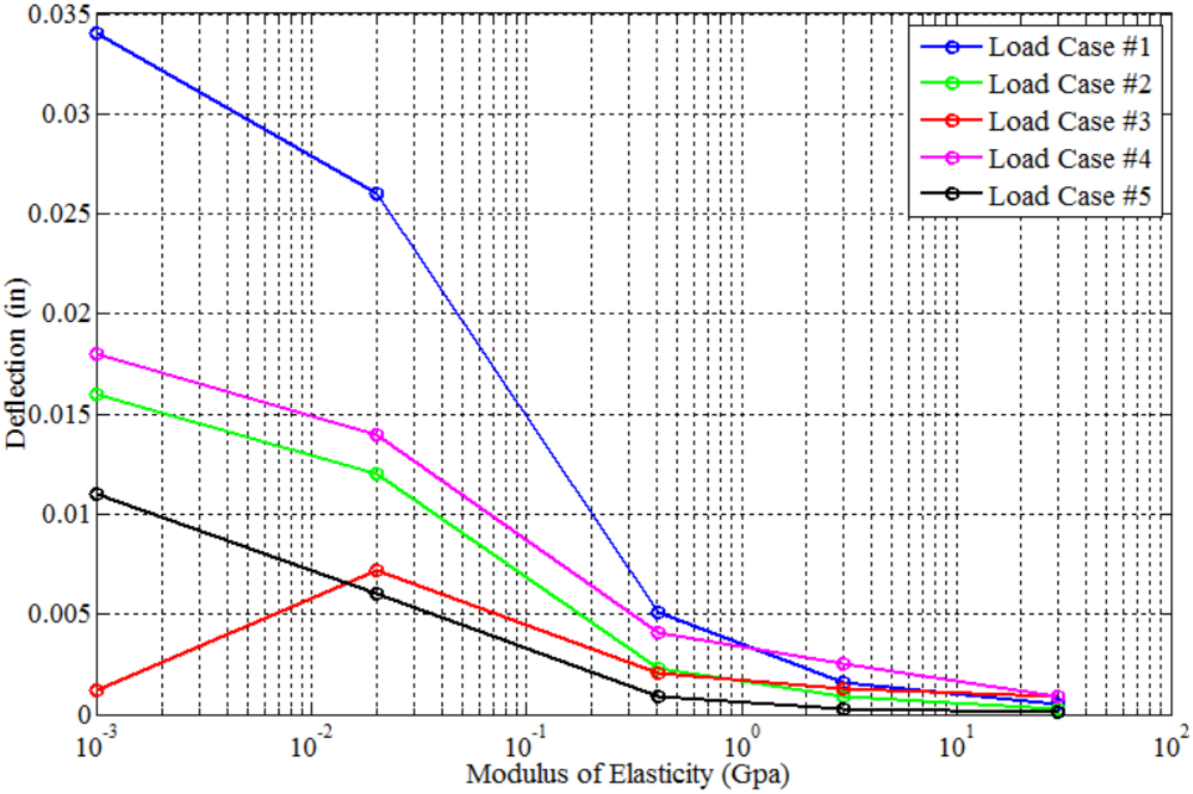

Figure 5-16: Max Deflection of Solar Cells under Equestrian Loading

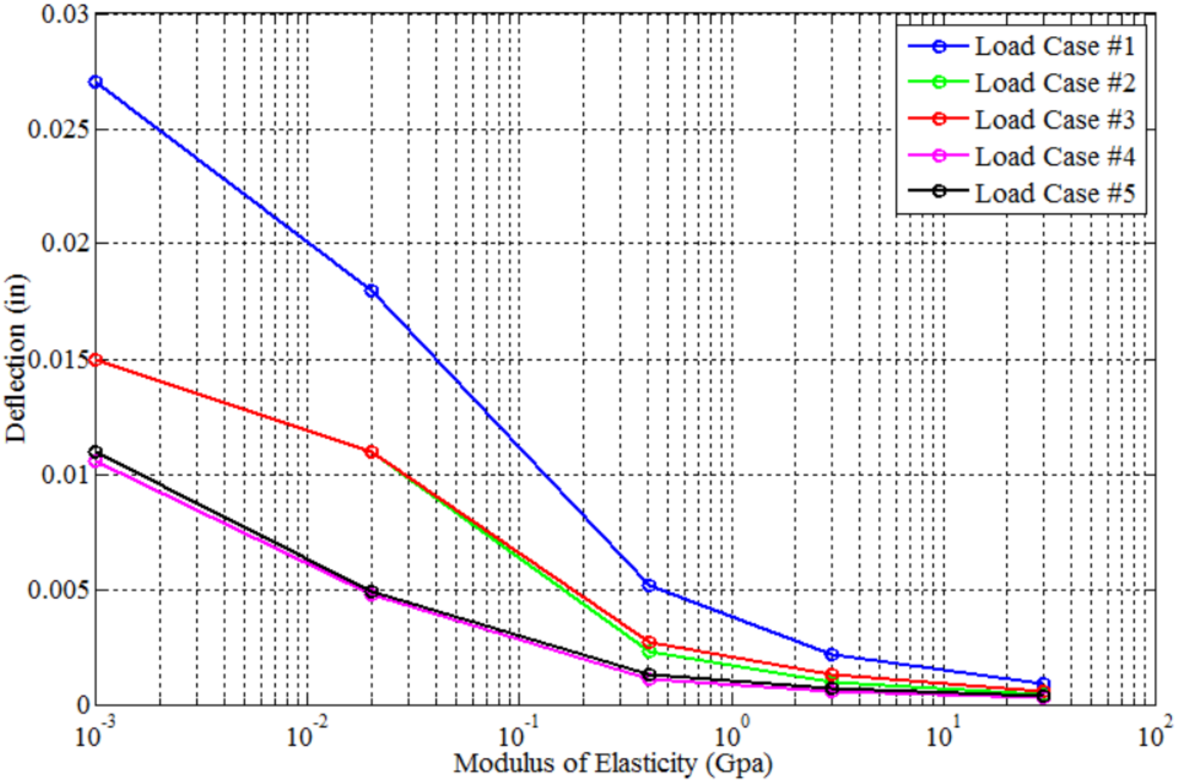

Figure 5-17: Max Deflection of Solar Cells under Vehicular Loading

Under all vehicular and equestrian loading cases as the modulus of elasticity of the intermediate materials increase, the maximum occurring deflection of the solar cells reduce considerably. The most dramatic case is equestrian loading at location #1 where the max deflection was reduced by 98.5% from 0.034in to 0.00047in. Similarly, the overall maximum deflection for vehicular loading was reduced by nearly 96.5% from 0.027in to 0.00088in when the materials modulus of elasticity increases to 30Gpa. Each maximum deflection occurred when a load was placed directly atop the corner of the glass slab, in both #1 load case locations when the modulus of elasticity for both cases was 0.001 (soft rubber). Deflection as well as stress analyses have both concluded with identical trends that as the modulus of elasticity increase to that of concrete, the overall stresses and deflections within the solar cells are at their lowest.

Table 5-7: Maximum Deflection of Cells using Concrete Intermediate

Concrete Intermediate Material		
Load Case	**Applied Load Location**	**Max Deflection (in)**
Pedestrian	Distributed	0.00083
Equestrian	#1	0.00047
	#2	0.00027
	#3	0.00087
	#4	0.0015
	#5	0.00011
Vehicular	#1	0.00088
	#2	0.00044
	#3	0.00056
	#4	0.00029
	#5	0.00038
	Max Deflection =	0.0015in

Table 5-7 shows the maximum deflection of the solar cells generated by the corresponding load cases with a concrete as the intermediate material. The maximum resulting deflection occurred in the cells under equestrian load case #4. The resulting deflection is 0.0015in and the max deflection location is shown in Figure 5-18.

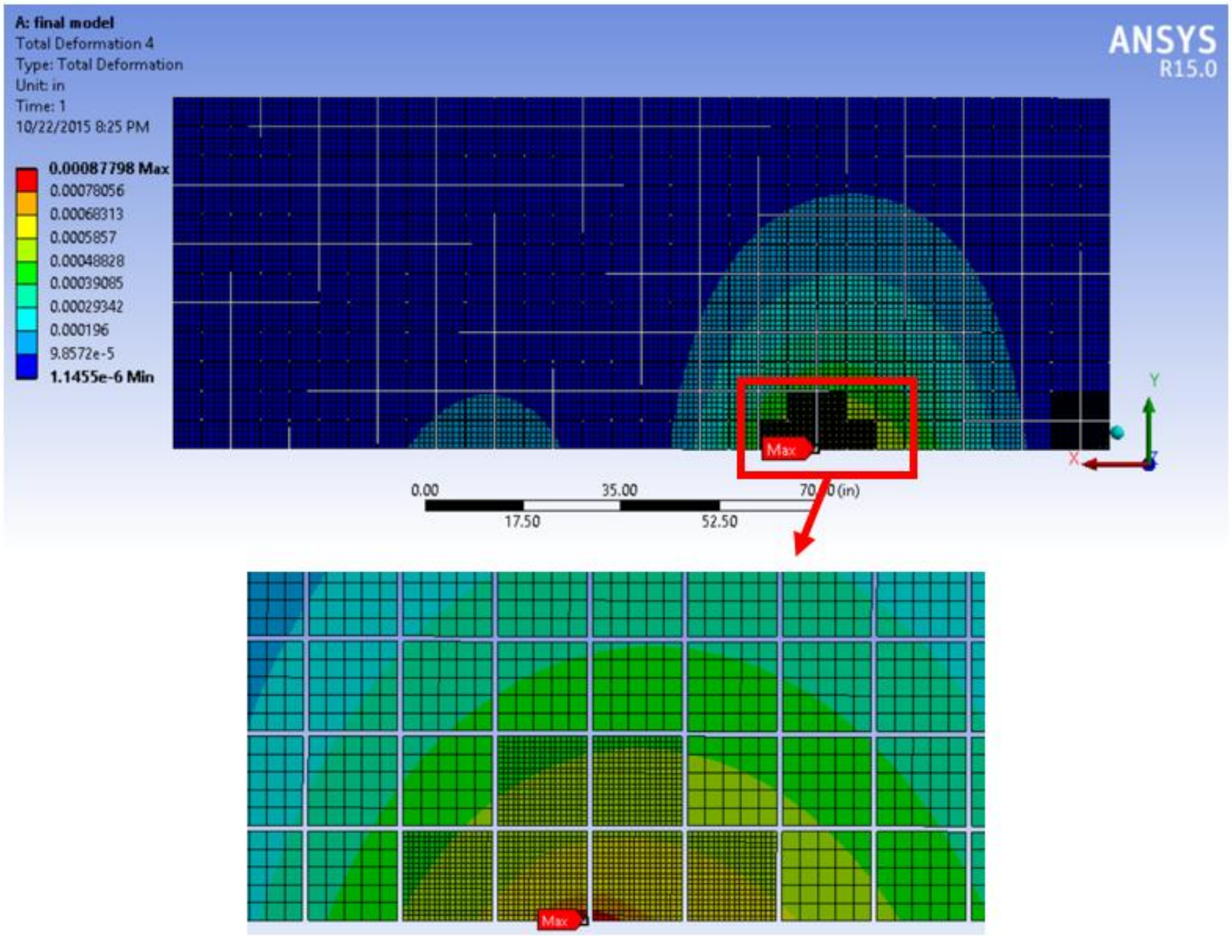

Figure 5-18: Cell Maximum Deflection Location

Equestrian load case #4 gave the largest resulting deflection of the solar cells. The tempered glass and the solar cells experienced maximum deflections under two different load cases. Equestrian load case #4 produced maximum deflection of the cells because the loading was along the edge of the cell configuration and also the load was applied at mid-span of two of the steel stringers. This cantilever effect produced the maximum deflection within the solar cells.

5.7 Finite Element Results of Natural Frequencies and Mode Shapes

A finite element analysis was performed to predict the undamped natural frequencies and mode shapes of an individual slab while constrained by three stringers below. The model was built in ANSYS 15.0 and all geometry and material properties were imported from the static structural model used previously. Table 5-8 shows the calculated natural frequencies for each mode for both a silicon elastomer and concrete intermediate. Figure 5-19 shows a snapshot of the mode shape animations.

Table 5-8: Calculated Natural Frequencies from FEA

Silicon Elastomer intermediate		Concrete intermediate	
Mode Shape	Frequency (Hz)	Mode Shape	Frequency (Hz)
1	121	1	152.9
2	127.4	2	163.6
3	153.7	3	191.1
4	159.4	4	201.8
5	243.9	5	339.7
6	248.2	6	346.9

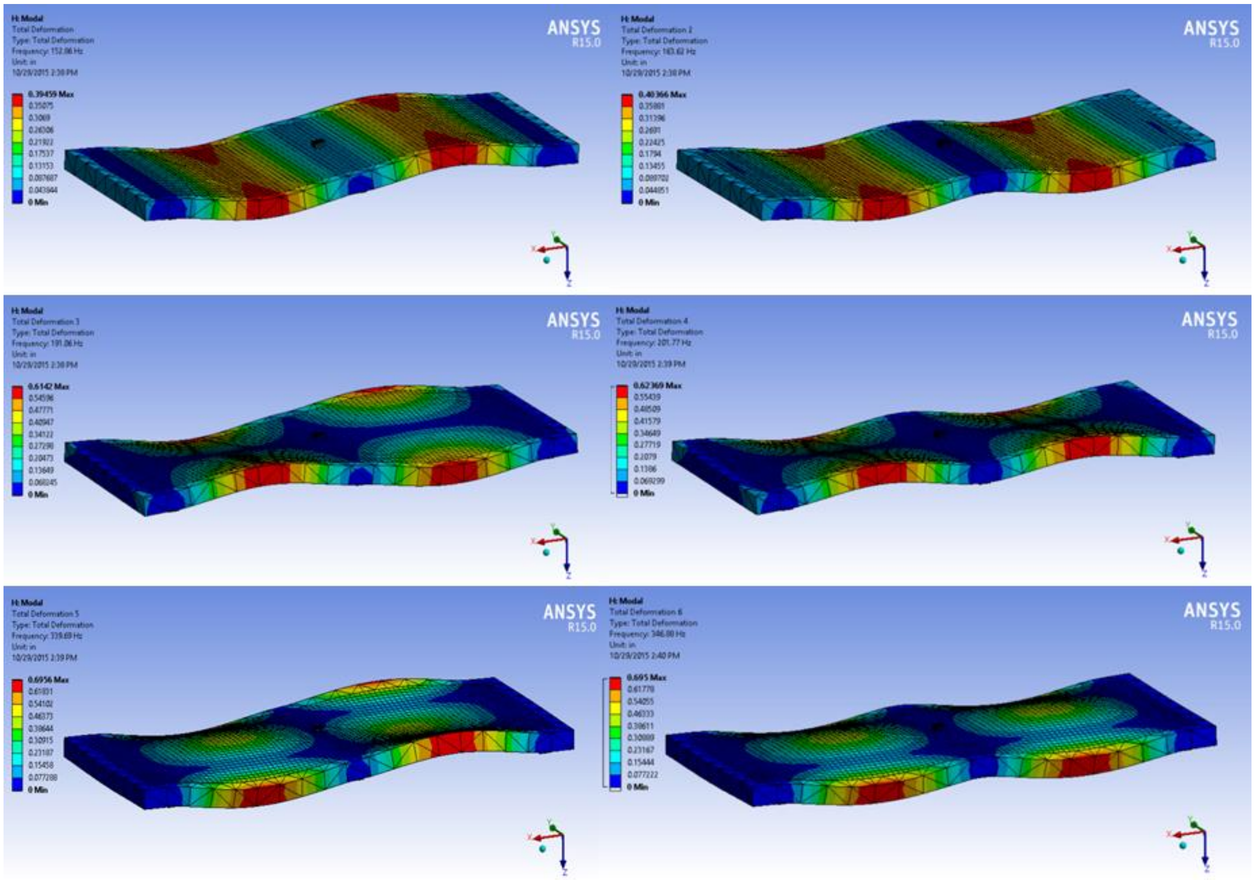

Figure 5-19: FEA Mode Shapes (1st to 6th Modes from Upper Left to Lower Right)

The mode shapes appear reasonable for a typical slab geometry. The values of the frequencies for each mode shape are very high and show that the system is very stiff. This is because of the thickness of the slab and the overall mass of the slab. The mode shapes represent the dynamic properties of a single deck slab under vibrational excitation. This excitation is important in study because varying forms of vibration will be induced on the slabs by pedestrian, vehicular, and equestrian loadings. It is imperative that a slab's natural frequency not match the frequency of expected loadings. If a slab's natural frequency matches one of the loading's frequencies, the slab may continue to resonate and experience structural damage.

5.8 Model Error Analysis

Results have concluded that the highest stresses occur in the solar cells and tempered glass for both equestrian and vehicular load cases, when loadings are located in the corner of the slab. While these results do not raise concern for alarm, the sharp change in stress values does. Values recorded in tables 5-2 and 5-5 maintain similar values as the loading locations move among the surface of the slab. In both cases however, the highest recorded stresses for equestrian and vehicular loading case #1 produce severely high amounts of stress in the very corner of the solar cells shown in Figure 5-20.

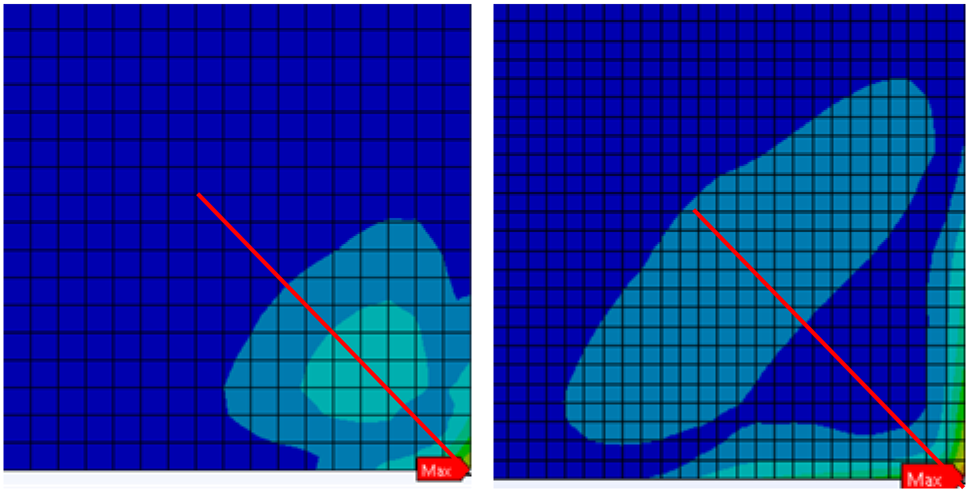

Figure 5-20: Stress "hot spots" in Solar Cells

The finite element model may be generating a final stress for both cases in which the max stress actually increases exponentially as it reaches the corners of both materials. The figures below show the stress values through each cell as the values approach the corner of the solar cell in the cases above.

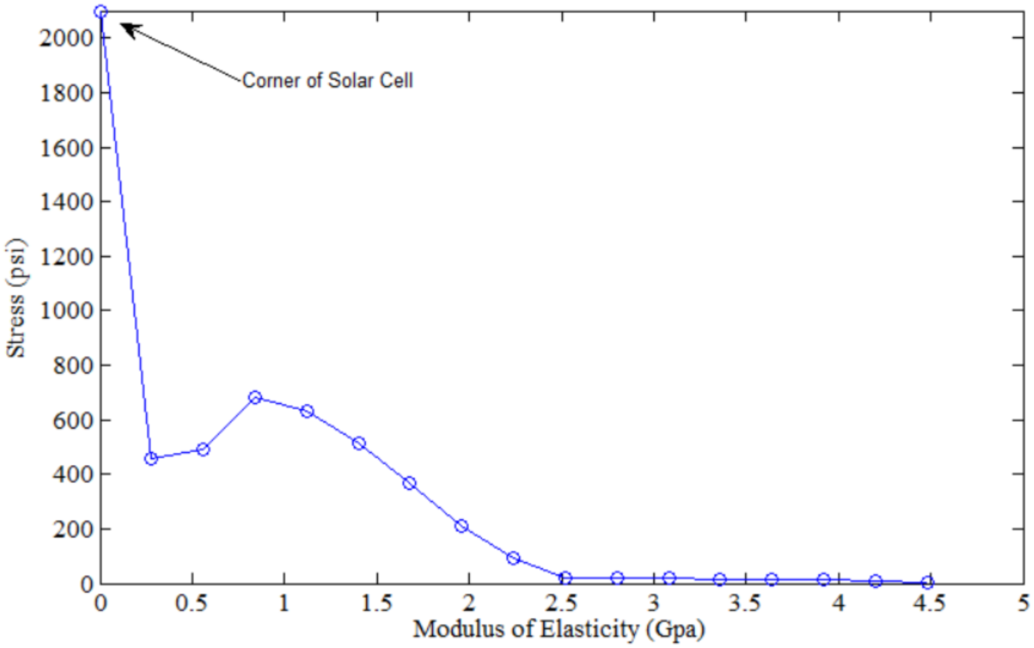

Figure 5-21: Stress in Solar cell along red line (left cell Fig 5-20)

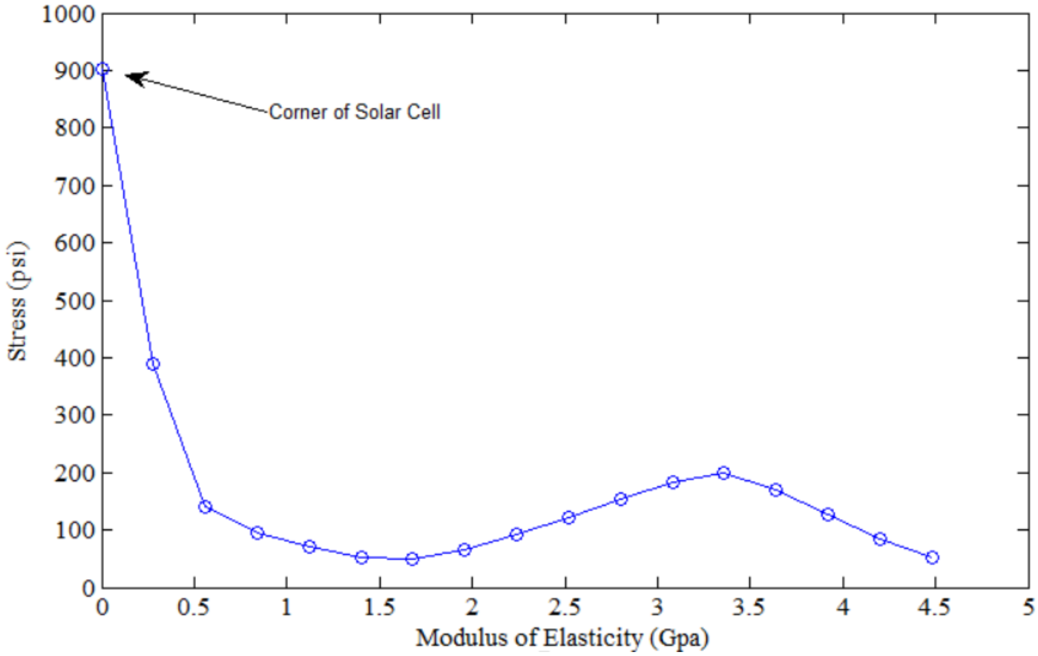

Figure 5-22: Stress in Solar cell along red line (right cell Fig 5-20)

It is clear that a more in depth analysis of the solar cells under load case location #1 should be conducted in the future. It is believed in this thesis that the max stress is not realistic compared with the rest of the stress field results. It is thought that an average of the values could be considered to determine a more reasonable max stress, but no evidence is presented to support this thought.

CHAPTER 6

CONCLUSION AND FUTURE WORK

This thesis deals with the development of a bridge deck surface that is both strong enough to withstand AASHTO LRFD pedestrian bridge load cases and able to generate a beneficial amount of power from incident irradiance using embedded solar technology.

It was concluded that the embedded solar cells produce 161.5kWh/day on average over the course of 25 years. This number includes cell decay and the benefits of zero maintenance and replacement costs for faulty equipment. The deck can produce an amount of energy equivalent to 7.5 Massachusetts houses or 50 campus walkway lamps, showing it can produce more energy than it takes to light its own surface. The total reduction in power generation due to bridge deck integration is 62% compared with an equal size solar module under ideal solar conditions in Massachusetts. Although a large decline in power generation due to integration, the economic feasibility of the solar deck was concluded to be very plausible. With the Massachusetts state tax credit for solar projects, the breakeven point of a solar deck slab was just under 8 years with Solarworld plus mono silver 285w cells. The return of investment was 215.7% over its lifetime of 25 years.

A finite element model of a single bridge deck slab was generated and analyzed using ANSYS Workbench 15.0 to determine maximum stress and deformation patterns under AASHTO LRFD load cases. The developed finite element model was implemented and it demonstrated that the performance of the proposed deck slab would be capable of withstanding forces due to bending in both the thin glass structure and solar cells. In one hand the computational performance concluded that the intermediate material should not be made of a material with a modulus of elasticity of 0.001Gpa. While in the other hand, the lowest resulting stresses in the tempered glass and solar cells resulted from a modulus of elasticity equal to 30Gpa, showing that the glass and internal embedded solar cells can simply rest upon the underlying concrete slab without the need of an intermediate material, however, it is recommended that a thin material of similar properties to that of concrete be inserted between the cells and concrete slab to offset potential high stress points caused by imperfections of the concrete during the precast stage. Because the max stresses were found in the solar cells at very concentrated “hot spots”, an investigation of the stresses with different design parameters, and meshing could be performed with finite element analysis.

In 2009 SolaRoad kick started the beginning of the solar based walking surface era with a 70 meter long prototype. After a solar analysis of the suburban pathway just outside Amsterdam center, it was estimated that the solar path would generate 70kWh/m^2/year, and that the entire system would have a breakeven point of 15 years. In late 2015 the pilot had successfully been running for one year. Estimates turned out to be much lower than actual power production. Over the course of one year in operation the 70m x 1.6m SolaRoad generated 9800kWh of energy, or 88kWh/m^2/year, a 25% increase of what was first estimated. This thesis concluded that its solar integrated bridge deck can generate a maximum of 58,765kWh of energy per year, or 168kWh/m^2/year with 21% efficient solar cells, which are the most efficient cells commercially available today. While thinking economically, using cheaper 17% efficient cells, the deck generate 47,800kWh of energy per year (137kWh/ m^2/year) with a payback period of 8 years. The difference in energy output is thought to be linked to two reasons. One being that the cells used in the SolaRoad are unknown and thought to be much lower in efficiency, roughly 12%. Second, the solar irradiance received by Amsterdam each year is about 15% less than what Massachusetts receives annually. Lastly the breakeven point is roughly half the predicted time of the SolaRoad. This is because the analysis was conducted for the entire SolaRoad system while this thesis only analyzed the solar system and not the entire concrete deck. With the increased cell efficiency comes more generated energy from the system and higher profits resulting in a reduced breakeven point.

For future work, a complete overhaul of the design should be conducted. The original design was concluded to be over engineered and should be redesigned without an intermediate material. With this fact, the slab should be nearly half the thickness of the original and the concrete encasement should be reconsidered for both material choice and design. Furthermore the tempered glass was found to withstand AASHTO LRFD pedestrian load cases, with only half the initial recommended thickness of 12mm. With a reduced design, in depth transient dynamic loading analyses are recommended. The development of an interlocking system for the deck slabs must be considered next. Incomplete and undermined slab sections will lead to water entry causing irregular slab settlement along with movement of individual slabs. Also precast slabs classically have problems with condensation forming on the interior of the slab wall due to inadequate protection against air flow where temperatures vary from the exterior wall of the slab. The slabs will be subjected to all weather conditions while the interior walls of the slab will conduct heat produced by the solar module. Therefore careful condensation and airflow monitoring needs to be addressed and heavily considered in the future slab design.

Lastly, a design that incorporates an added layer of EVA film to both sides of the solar cells should be analyzed as this important material for solar power generation also adds structural advantages to the solar cells. It could also be interesting to consider types of fastening systems to secure the solar cells and glass to the concrete deck, such as bolt connections or clamps around the exterior of the slab creating interesting concentrated stress fields. One could consider other types of connections and create an overview of different types of connections and resulting stress associated. Especially adhesive connections are of interest, because the larger contact area between the connection and the glass leads to a redistribution of the stress concentrations that glass may be subjected to. The use of glued connections also leads to greater transparency of the structure.

APPENDIX

STRUCTURAL DESIGN DOCUMENTS

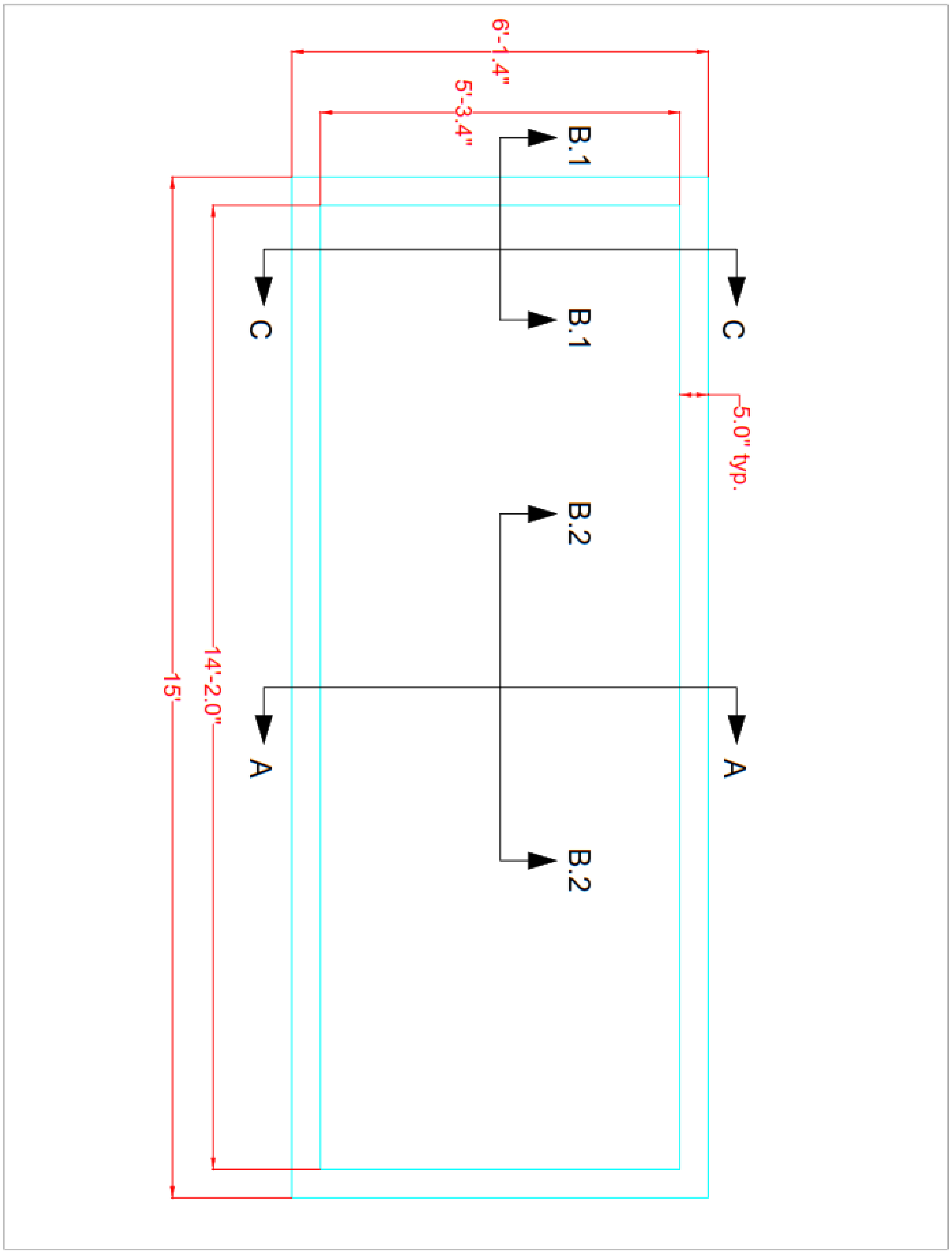

B.2 - B.2
Cross Section Detailing

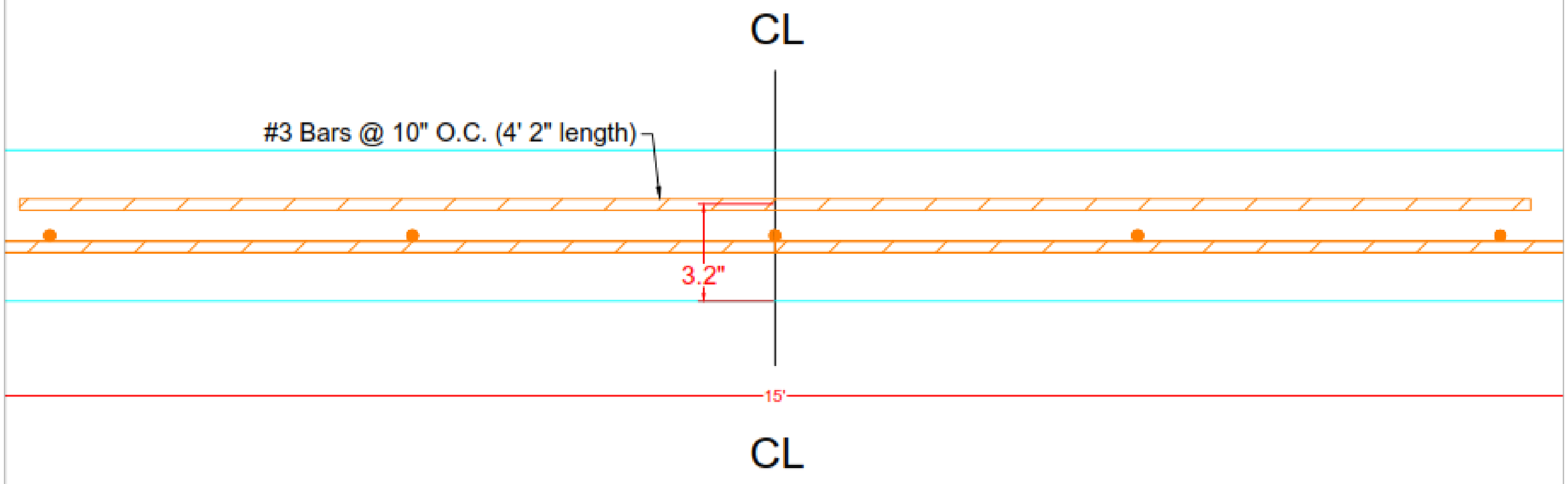

B.1 - B.1
Cross Section Detailing

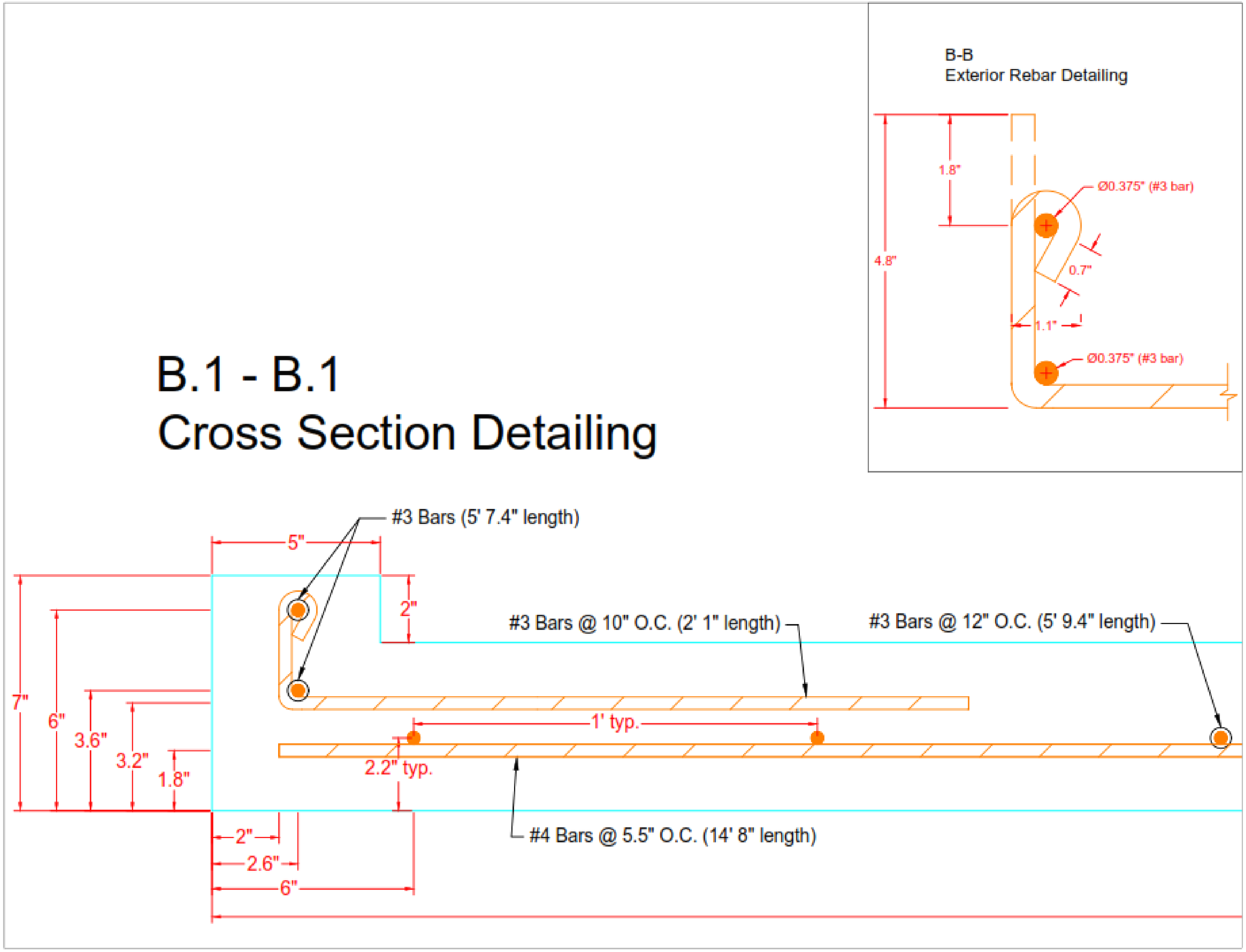

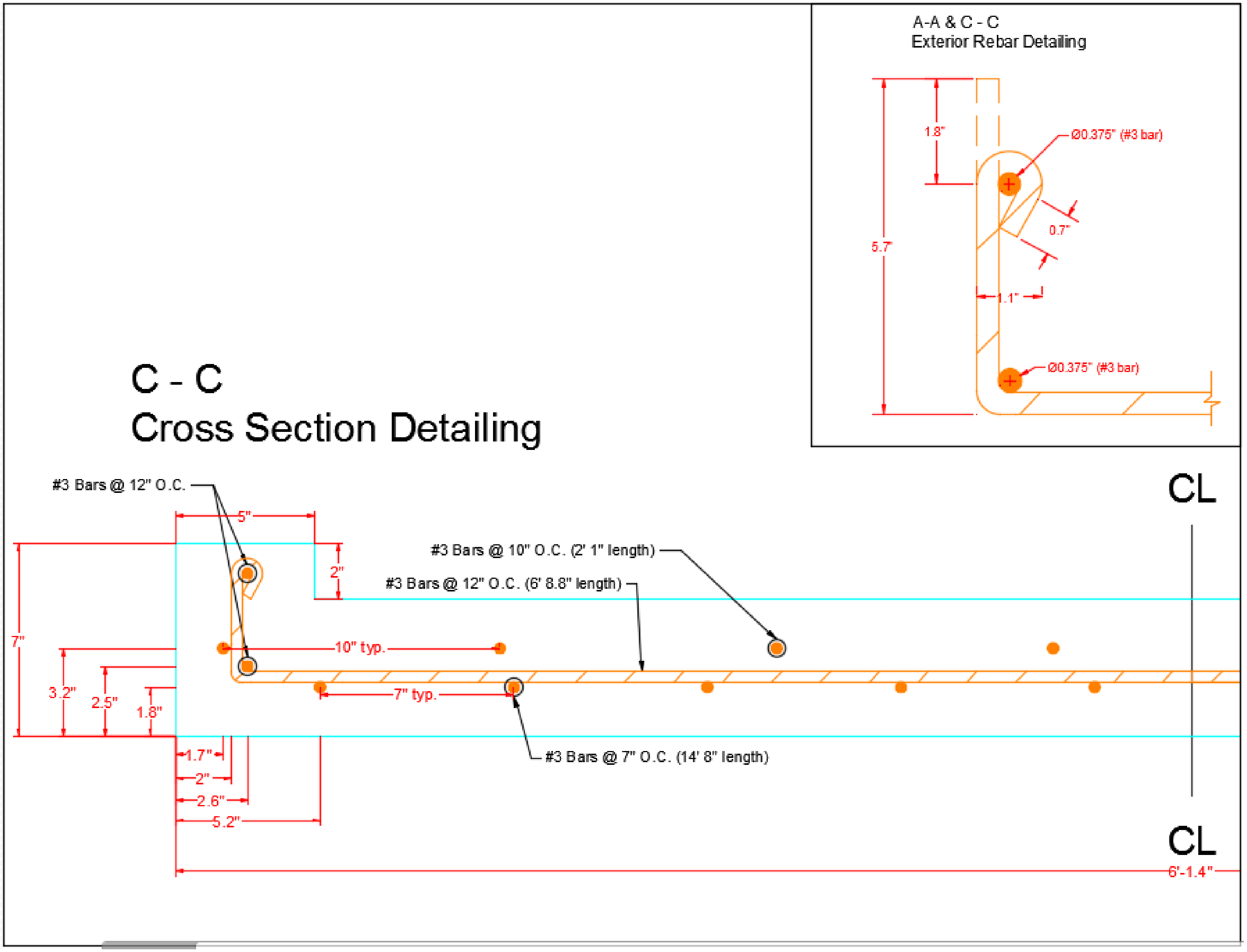
C - C
Cross Section Detailing
#3 Bars @ 12" O.C.
#3 Bars @ 10" O.C. (2' 1" length)
#3 Bars @ 12" O.C. (6' 8.8" length)
#3 Bars @ 7" O.C. (14' 8" length)
5"
2"
7"
3.2"
2.5"
1.8"
10" typ.
7" typ.
1.7"
2"
2.6"
5.2"
6'-1.4"
CL
CL
A-A & C - C
Exterior Rebar Detailing
1.8"
5.7"
Ø0.375" (#3 bar)
0.7"
1.1"
Ø0.375" (#3 bar)

REFERENCES

BASF Polyurethanes GmbH. (2011). ThermoPlastic Polyurethane Elastomers (TPU) - Material Properties.

Bos, F. P., & Zuidema, J. (n.d.). STRENGTH AND FRACTURE BEHAVIOUR OF, 2–7.

Cambridge University Engineering Dept. (2003). Materials Data Book.

Cano, J., Tamizhmani, G., Madakannan, A., & Macia, N. (2011). Photovoltaic Modules: Effect of Tilt Angle on Soiling.

Federal Highway Administration. (n.d.). Walkways, Sidewalks, and Public Spaces 13.1.

Feldmann, M. (2008). Human induced Vibrations of Steel Structures Design of Footbridges Background Document.

Fröling, M. (2011). Strength Design Methods for Laminated Glass.

Gaur, A., & Tiwari, G. N. (2013). Performance of Photovoltaic Modules of Different Solar Cells. *Journal of Solar Energy*, *2013*, 1–13. http://doi.org/10.1155/2013/734581

Gehrilicher. (2015). Defining Photovoltaic. Retrieved from http://www.gehrlicher.com/us/service/faq/what-does-photovoltaics-mean/

Karnopp, D. C., Margolis, D. L., & Rosenberg, R. C. (2012). APPENDIX : TYPICAL MATERIAL PROPERTY VALUES USEFUL IN MODELING MECHANICAL , ACOUSTIC , *5th*.

Kaule, F., Wang, W., & Schoenfelder, S. (2013). Modeling and testing the mechanical strength of solar cells. *Solar Energy Materials and Solar Cells*, *120*, 441–447. http://doi.org/10.1016/j.solmat.2013.06.048

Lee, D. M., & Raichle, B. W. (n.d.). A SIDE-BY-SIDE COMPARISON OF MICRO AND CENTRAL INVERTERS IN SHADED AND UNSHADED CONDITIONS.

LRFD GUIDE SPECIFICATIONS FOR THE DESIGN OF PEDESTRIAN BRIDGES FINAL DRAFT LRFD GUIDE SPECIFICATIONS FOR THE DESIGN OF PEDESTRIAN BRIDGES. (n.d.).

Neugebauer, J. (n.d.). To Increase the Residual Bearing Capacity of Glass with a Local Reinforcement.

Occupational Safety and Health Administration. (n.d.). Static coefficients of friction for walking/working surfaces. Retrieved November 17, 2014, from https://www.osha.gov/pls/oshaweb/owadisp.show_document?p_id=24511&p_table=INTERPRETATIONS

Officials, A. A. of S. H. and T. (2012). Aashto Lrfd, 1661.

Pascual, C., Castro, J. De, Schueler, A., Vassilopoulos, A. P., & Keller, T. (2013). TOTAL LIGHT TRANSMITTANCE OF GLASS FIBER-REINFORCED POLYMER LAMINATES FOR MULTIFUNCTIONAL LOAD-BEARING STRUCTURES, 73–78.

Peter Parts Electronics. (n.d.). Lesson on Solar Panels.

Pingel, S., Zemen, Y., Frank, O., Geipel, T., & Berghold, J. (n.d.). MECHANICAL STABILITY OF SOLAR CELLS WITHIN SOLAR PANELS.

Popovich, V. A., Riemslag, A. C., Janssen, M., Bennett, I. J., & Richardson, I. M. (2013). Characterization of Multicrystalline Silicon Solar Wafers Fracture Strength and Influencing Factors. *International Journal of Material Science*, *3*(1). Retrieved from www.ij-ms.org

Reno, M. J., Hansen, C. W., & Stein, J. S. (2012). Global Horizontal Irradiance Clear Sky Models : Implementation and Analysis, (March).

Ritter, & Michael A. (1990). Timber Bridges: Design, Construction, Inspection, and Maintenance Š Chapter 6: Loads and Forces on Timber Bridges.

Sacher, A. (1996). Coefficient of Friction An Overview of : Floor Surfaces , Polishes and Maintenance Interaction, 1–6.

Sampath, S., & Ramachandra, G. S. (2008). Effects of glass fibers on light transmittance and color of fiber-reinforced composite. *Dental Materials : Official Publication of the Academy of Dental Materials*, *24*(1), 34–8. http://doi.org/10.1016/j.dental.2006.12.010

Sander, M., Dietrich, S., Pander, M., Ebert, M., & Bagdahn, J. (2013). Systematic investigation of cracks in encapsulated solar cells after mechanical loading. *Solar Energy Materials and Solar Cells*, *111*, 82–89. http://doi.org/10.1016/j.solmat.2012.12.031

Schnieder, F., & Womer, J. D. (n.d.). Inelastic Material Behavior of Soda-Lime-Silica Glass.

Steinzig, M. (2000). Bend Tests of Silicon Ladders to Determine Ultimate Strength.

SunPower. (n.d.-a). SunPower X21-345 Product Guide.

SunPower. (n.d.-b). *SunPower: Safety and installation instructions*.

Techno Glass. (n.d.). Techno Glass Product Guide.

U.S. Department of Transportation - Federal Highway Administration. (n.d.). Chapter 4 - Sidewalk Design Guidelines and Existing Practices - Sidewalks - Publications - Bicycle & Pedestrian Program - Environment - FHWA. Retrieved November 19, 2014, from http://www.fhwa.dot.gov/environment/bicycle_pedestrian/publications/sidewalks/chap4a.cfm

University of Massachusetts Amherst. (2014). Campus Metering.

University of Massachusetts Lowell. (n.d.). Natural frequencies for Common Systems.

Wilby, K. (2012). Modal Characterization of a Thin Flat Plate in the Free-Free Condition with Non-Contact Particle Velocity Measurements by, (December).

Yixian, L., & Tay, A. a. O. (2011). Finite element thermal stress analysis of a solar photovoltaic module. *2011 37th IEEE Photovoltaic Specialists Conference*, 003179–003184. http://doi.org/10.1109/PVSC.2011.6186616